UNIVERSITY OF
BIRMINGHAM

New Materials for Strontium Removal from Nuclear Waste Streams

by

Savvaki Neoklis Savva

Supervisor: Dr Joseph A. Hriljac

A thesis submitted to The University of Birmingham for

the degree of Doctor of Philosophy

The School of Chemistry

College of Engineering and Physical Sciences

University of Birmingham

September 2015

Abstract

The primary aim of this project is to investigate potential new materials for application in ion exchange processes to remove ^{90}Sr from nuclear waste streams. This work can be broadly split in to two sections, work on attempts to synthesise new materials and work to investigate ion exchange properties of two recently prepared materials AV-7, a synthetic analogue of tin-kostylvite and AV-3, a synthetic analogue of petarasite.

Synthesis on new materials was focused on metal silicate materials, in particular titanium, zirconium and tin silicates containing exchangeable group I and II cations. These synthesis attempts initially were focus on targeted mineral phases such as noonkanbahite, $BaKNaTi_2(Si_4O_{12})O_2$, followed by a series of brief surveys examining the effects of various changes to precursor gels such as concentration of bases such as NaOH, metal to silicon ratios and the presence of mineralizing agents such as sodium fluoride. The synthesis of two synthetic mineral phases potentially interesting for ion exchange is also reported here, titanite and fresnoite.

Ion exchange studies focused mainly on AV-7 and AV-3 but also included well known ion exchange materials for comparison such as clinoptilolite and Nb-doped crystalline silicotitanate and brief investigations in to the ion exchange of fresnoite and titanite. Ion exchange was followed using X-Ray fluorescence, ion chromatography and radioactive ^{85}Sr exchanges measured using scintillation counters.

Acknowledgements

I would firstly like to thank my supervisor Dr Joe Hriljac for all his support throughout this PhD project and all its difficulties. Thanks also to those at the NNL who helped with this work in particular my NNL supervisor Dr. Zoe Maher for some valuable guidance but also to Dr. Scott Owns for useful discussions. Financial sponsorship from the School of Chemistry, University of Birmingham and the NNL is also gratefully acknowledged.

A special thanks to past and present members of the Hriljac group, Tom Carey for help with my crystallography problems and George and Geoff for the time we spent in Boston. A special thanks to Evin who has been an incredible help throughout my time here.

I would also like to thank all those from the 5th floor of chemistry who helped in innumerable ways over the course of my work, from useful discussions over cups of tea to blowing of steam bouldering. A great thanks also to Dr Jackie Deans whose technical support has been a great help to me and everyone on floor five.

Finally I'd like to thank Katrina whose love, patience and support have helped with the hardest part of this work, the writing of it.

Contents

List of Figures

List of Tables

List of abbreviations

(P) XRD - (Powder) X-ray diffraction

BSE - Backscattered electrons

CST - Crystalline silicotitante

DTA - Differential thermal analysis

EARP - Enhanced actinide removal plant

EDS - Energy dispersive X-ray spectroscopy

GDF - Geological disposal facility

HDPE - High density polyethylene

HIP - Hot isotactic pressing

HLW - High level waste

HRPD - High resolution powder diffraction

ICDD - International centre for diffraction data

ICP- Inductively coupled plasma

ILW - Intermediate level waste

MS - Mass spectrometry

NNL - National nuclear laboratory

OES - Optical emission spectroscopy

PDF - Powder diffraction file

PTFE - Polytetrafluroethylene

RAL - Rutherford Appelton laboratory

SEM - Scanning electron microscopy

SIXEP - Sellafield ion exchange effluent plant

TEOS - Tetraethylorthosilicate

TGA - Thermal gravimetric analysis

TIP - Titanium isopropoxide

WDS- Wavelength dispersive X-ray spectroscopy

XRF - X-ray fluorescence

Chapter 1: Introduction

1.1 Background

With a growing number of nuclear power stations the storage and treatment of UK legacy waste is a growing concern. Radioactive waste is categorized according to the total radioactivity, heat generated and half-life as low level waste (LLW), intermediate level waste (ILW) and high level waste (HLW). According to the 2013 radioactive waste inventory produced by the Nuclear Decommissioning Authority (NDA) and UK Department of Energy and Climate Change (DECC)[1] there are 4.5 million cubic meters of waste in the UK. LLW is primarily composed of building materials and comprises the largest portion of this waste, approximately 94% by volume but less than 0.01% of the total radioactivity. The composition of ILWs can vary greatly but also contains building materials along with sludges, ion exchange resins and flocs. HLW is initially produced as a nitric acid solution containing fission products from the reprocessing of fuels. The long term storage goal of ILW and HLW is storage at a Geological Disposal Facility (GDF). However, in addition to solid wastes there is a large volume of contaminated water used for cooling and washing of contaminated materials; this presents a problem due to the difficulty in storing large volumes of radioactive material. It is this high-level waste which contains much of the strontium-90 ($t_{½}$=28.79 years) and caesium-137 ($t_{½}$=30.17 years) with which this thesis is primarily concerned; these are major contaminates in liquid effluent and are responsible for the bulk of heat generated in these wastes. Selective removal of strontium-90 and caesium-137 into a solid medium would result in a significantly more compact waste form which is of particular importance considering the space available at a GDF is a concern. Strontium-90 is of particular concern due to mimicking calcium in biological systems and is readily incorporated in-to bone tissue where it will follow the decay pathway; a beta emission of 546 KeV to yttrium-90 and subsequently to zirconium-90 via a 2.28 MeV beta emission[2]. Caesium-137 can also be incorporated into biological systems where it will replace potassium and follows a decay pathway of beta decay to barium-137 followed by an X-ray emission of 662 keV.

In order to remove these radionuclides highly selective and robust ion exchangers are required as the waste solutions not only contain a wide range of cations which could potentially compete with the ion exchange targets, but also form a highly aggressive environment. In addition due to the high mobility of ^{90}Sr and ^{137}Cs a low leach rate is a vitally important property of an ion exchanger or a material it is transformed into as once stored any incidents such as flooding should not spill radioactive waste over a large area.

The ability for soils and natural minerals to absorb cations has been known and studied for a number of years[3], however poor pH and chemical stability of these materials led to the development of organic ion exchange resins such as polystyrenedivinylbenzene[4] which replaced many of the inorganic ion exchangers in use.

There are some processes in the nuclear industry, however, that have specific requirements for ion exchangers which these organic resins did not meet, most importantly good selectivity whilst maintaining resistance to ionizing radiation and high temperature. This lead to a number of inorganic ion exchange materials developed with use for the nuclear industry in mind[5,6]. Organic resins are common in other ion exchange applications, such as the petrochemicals industry but are not as commonly found in the nuclear industry[7] where they act as filters for particulates such as cobalt and nickel and ion exchangers for ionic contaminants such as caesium and strontium.

Inorganic ion exchangers have been primarily used to treat waste solutions from decontamination operations and leaks in place of using evaporation type treatment, but despite a wide range of materials being tested few materials have demonstrated consistently good separation performance[8–10].

1.2 Ion exchange

Ion exchange is a process whereby ions within a mobile phase are exchanged with loosely bound ions electrostatically bound to an insoluble stationary phase eg:

$$S - H + Na^{+} \leftrightarrow S - Na + H^{+} \qquad (1.1)$$

where S is a stationary phase such as organic resin or inorganic material.

The ion exchange process is heavily dependent on both kinetic and thermodynamic factors. In order for an ion exchange to be thermodynamically favourable it would be expected the ion to be removed from the mobile phase when compared to the ion in the stationary phase should:

- have a higher valence
- have a smaller solvated volume
- have a greater ability to polarize
- should precipitate less with any other reagents to form complexes

Kinetics of ion exchange are dependent upon the rate of particular transport pathways involved. A simplified form of the overall process is described as:

1. movement of ions from bulk solution to film or boundary layer surrounding ion exchanger solid
2. transport through film/boundary layer to solid surface
3. transport through pores of solid to exchange site
4. exchange of ions
5. transport of exchanged ion outward through pores of solid
6. transport of exchanged ion outward through film/boundary layer
7. movement of exchanged ion into bulk solid

Typically the rate is controlled by steps 2 or 3 and these steps can be heavily affected by cation/pore size and charge distribution throughout the material.

When examining the performance of an ion exchange material there are 3 commonly used metrics:

- Cation exchange capacity – this represents the highest possible exchange often based upon standardized measurement tests such as extraction with ammonium acetate, often given in units of milliequivalents per gram.

- Batch distribution coefficient – The batch distribution coefficient (K_d) is an equilibrium constant, used to measure of the uptake of an ion exchanger relative to the ratio of exchanger to solution, it is given as:

$$K_d = \frac{V(C_0 - C_1)}{mC_1} \tag{1.2}$$

where:

V is the total volume of solution;

C_0 is the initial concentration of the ion of interest;

C_1 is the final concentration of the ion of interest;

m is the mass of ion exchange material used;

Whilst this metric may seem to be well suited to comparing different sets of ion exchange experiments, in practice they can vary significantly between experiments due to a number of factors affecting ion exchange and so it best to only use as a comparison within the same experimental conditions.

- Selectivity coefficient – an equilibrium constant used to determine how selective an ion exchanger is for the desired cation when other competing cations are present:

$$k_{Cs/Na} = \frac{[Cs]_{solid\ phase}[Na]_{liquid\ phase}}{[Cs]_{liquid\ phase}[Na]_{solid\ phase}} \tag{1.3}$$

1.3 Inorganic ion exchangers

1.3-1 Natural inorganic ion exchangers

Clay materials such as kaolinite, bentonite and illite have been studied as ion exchangers extensively[11,12], these materials are phyllosilicates, structures formed by parallel sheets of silica tetrahedra, with two dimensional or layered structures comprised of Si /Al tetrahedra and Mg/Al octahedra, with cations such as Na^+, K^+, Ca^{2+} or Mg^{2+} to charge balance. Ion exchange sites are typically located on the surface, resulting in little to no ion sieve effect decreasing selectivity, however with good uptake and relatively low cost, the low selectivity can be of little importance. The mechanical properties of these materials, however, have reduced their use in an industrial setting as they are not suited to use in a flow through column-type exchanger due to poor fluid flow limiting their use to batch type reactors.

Mica type materials, such as biotite and muscovite have also been investigated for their ion exchange properties[13]. Micas are also phyllosilicates but have three dimensional structures composed of two silica tetrahedral layers corner sharing with an MO_6 octahedral layer in between and two hydroxyl groups shared between three neighbouring octahedra. Common metals forming the octahedra are Fe^{2+} and Mg^{2+}, but can be replaced by trivalent cation such as Fe^{3+} or Al^{3+}, Fe^{3+} can also replace Si^{4+} in a tetrahedron, generating negative charge on the framework [14]. The charge of the framework is balanced by the interlayer cations or anions which are exchangeable and result in the structure being expandable.

Zeolites are microporous (0.2-2 nm pore size) crystalline hydrated aluminosilicates defined by the general formula:

$$M_{2/n}OAl_2O_3.xSiO_2 \cdot yH_2O \tag{1.4}$$

where *M* is a non-framework cation.

The structure is built up of primarily Si and Al, but also can include Ga, Ge, Zn and Be, which are tetrahedrally coordinated to four oxygen atoms and linked to other tetrahedra forming secondary building units (SBU), such as single and double rings and cages such as the β-cage which can be thought of as a truncated octahedron. The structural features of zeolites in turn form rigid 3-dimensional frameworks of pores and channels. AlO_4 units are responsible for negative charge on the framework, counterbalanced by extra-framework cations or protons located in the pores or channels of the structure. The negative charge is located on an oxygen anion connected to the aluminium forming a Brønsted acid site if the site is a proton rather than a cation in the pore. The Si/Al ratio is a crucial feature of zeolites especially in terms of ion exchange, as this controls the overall framework charge and thus acidity and number of extra-framework cations. A lower Si/ratio and thus more negative framework would have a greater number of cations, but for the purpose of ion-exchange these cations may be too strongly bound for optimal exchange; counter to this too high a Si/Al ratio may lead to too few sites for ion exchange. The framework charge can also be modified by doping other atoms, such as Ga, into the framework to modify the charge[15]. According to Löwenstein’s rule zeolites cannot contain Al-O-Al bonds within the framework; this prevents centres of negative charge being close to each other. The flexibility of the of zeolite type pore structure provides zeolites with their ability to selectively adsorb molecules based on size and shape. Whilst ion exchange properties are often very good, dissolution of Si in basic and Al in acidic conditions results in a narrow pH range for optimal performance[16].

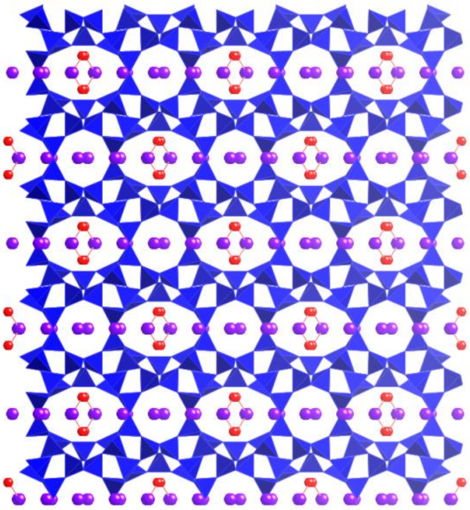

Figure 1. 1 - The structure of clinoptilolite, viewed along the c axis. Blue tetrahedra show SiO_4 and AlO_4 units. Purple spheres indicate cations and red the oxygen of water molecules.

Zeolites have been widely used as inorganic ion exchangers due to low cost and high availability, particularly at the Sellafield Site Ion Exchange Effluent Plant (SIXEP)[17,18], where clinoptilolite, Figure 1.1, a natural mineral with the heulandite framework is used for this purpose as illustrated in a simplified diagram of the SIXEP process in Figure 1.2.

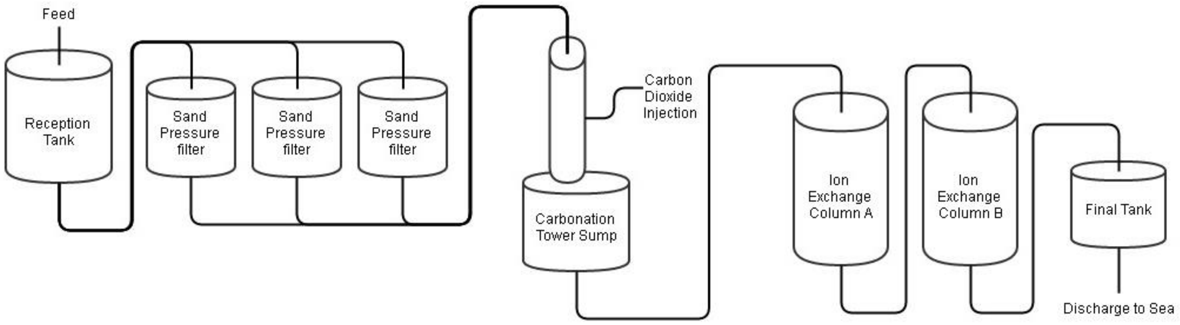

Figure 1. 2 - Schematic diagram of SIXEP process

However there are limitations to both the use of a natural zeolite. Zeolites tend to be most useful only within limited pH ranges, as not only can a high presence of protons affect ion exchange rates but extreme concentrations result in the dissolution of aluminium and silicon. Thus it is necessary at SIXEP to first neutralize the effluent stream. With regards to using a natural mineral, the composition can differ greatly depending on the site at which the mineral was acquired. The ion exchange properties of zeolites are highly dependent upon the Si/Al ratio and Al distribution throughout the structure as this affects the charge of the framework and the local cation environment. Thus reliance upon an inconsistent natural mineral is not ideal as the exact ion exchange properties cannot be fully known prior to testing and thus new synthetic materials for ion exchange have been a common area of research.

Elsewhere on the Sellafield site, the Enhanced Actinide Removal Plant (EARP) is responsible for the removal of beta emitting actinides. In contrast to the ion exchange processes of SIXEP, EARP uses the addition of sodium hydroxide to cause the flocculation of actinides by binding to them and forming insoluble metal hydroxides which sink and are easily separated from the effluent stream.

1.3-2 Synthetic ion exchangers

Unlike zeolites metallosilicates such as zirconosilicates, titanosilicates and stannosilicates do not follow Löwenstein's Rule, which in conjunction with the metals usually forming octahedra as opposed to tetrahedra in the zeolites, allows for a much wider range of crystal structures. The pore size of these materials is usually on the lower side of the range of zeolites, with pore sizes usually in the range of 3-7 Å compared to zeolites which can vary from 3-20Å depending on the structure. Similarly to zeolites the ratio of Si/M is also of great importance with respect to ion exchange for the same reason of controlling the framework charge and number of cations. Metallosilicate frameworks can also be modified with the addition of other framework cations, in particular Nb^{V} has been used to modify the framework charge of CST as discussed later in this section.

One of the most widely studied ion exchangers is crystalline α-zirconium phosphate ($Zr(HPO_4)_2 \cdot nH_2O$) [5,19–21]. Zirconium phosphate has a layered structure with interlayer distances of 7.6A to 5.3A between nearest P-OH groups. Van der Waals forces between water molecules of the structure and P-OH groups are responsible for the interlayer binding. The protons are exchangeable from the structure, most selectively for Cs with a high capacity 6.63 meq/g [22].

Hexacyanoferrate, the pigment Prussian Blue, has been marketed as a medicine for heavy metal sequestration for some time, however it has also been shown to be incredibly selective for caesium when prepared in a granular form as the commercially available CsTreat® which uses potassium cobalt hexacyanoferrate. The Fe^{II} or Fe^{III} forms can be prepared via precipitation with a metal salt solution, such as cobalt, to form the granular HCF particle with extremely good Cs selectivity which also has the mechanical properties desired by engineers to form columns. The high selectivity is due to cavities within HCF structure being very close match to size of caesium ion, allowing for an ion sieve effect to selectively ion exchange [23].

A series of papers by Dyer *et al.*[24–28] focused on the exchange of MCM-41 (Mobil Composition of Matter No. 41), a mesoporous silica material doped with heteroatoms Al, B and Zn. Unlike the previous materials which have been microporous with pore/channel diameters less than 2nm, MCM-41 is mesoporous with pores in the range of 2-50nm. Dyer used the incorporation of heteroatoms and different C-chain length to create a range of different pore sizes from 17.2 Å to 37.3 Å for a primary pore and to create a secondary pore of approximately 55 Å. Dyer used 0.05 g of solid in batch exchanges with a solid/solution ratio of 200 ml/g and nitrate salts of Li, K, Rb, Cs, NH_4, Mg, Ca, Sr, Ba, and Al to obtain a total normality of 0.15. Isotherms of these exchanges indicated that for all MCM-41 ion exchangers examined Cs^+, Rb^+,Na^+ and K^+ were preferentially ion exchanged over Sr^{2+} and other divalent cations; in fact this trend of monovalent cation selectivity over divalent cations is evident in the entire series of papers.

Sodium titanate ($Na_4Ti_4O_{20}\cdot nH_2O$), commonly as monosodium titanate and sodium nonatitanate are poorly crystalline or amorphous layered materials which have been demonstrated to have good ion exchange properties for strontium particularly under basic condutions[29]. It can be prepared by using titanium dioxide powder in concentrated sodium hydroxide solution under reflux to obtain a poorly crystalline material. The exact crystal structure has yet to be reported in the literature but sodium titanates are generally built from edge-sharing TiO_6 octahedra chains joined together through corner sharing to form layers with cations between them. Commercially available as SrTreat®, these materials have been implemented at some nuclear sites across the world [30,31], however, they have demonstrated a breakdown in performance in the presence of calcium, which is preferentially exchanged over strontium, drastically decreasing the use of sodium titanates in high salt waste streams. Poor exchange performance is also observed in low pH waste streams, thus calcium removal and neutralization of the waste stream is necessary in order to utilize these materials for strontium sequestration.

Potassium titanosilicate ($K_3H(TiO_4)(SiO_4)\cdot 4H_2O$), an analogue of the mineral pharmacosiderite, has been shown to have promise for strontium and caesium removal from waste streams under basic and neutral conditions[32,33] . Doping of Ge into the framework for Si was shown to increase the uptake of both Cs^+ and Sr^{2+} [34,35] although not by altering the framework charge but by altering the pore size of the material. A related material sodium titanosilicate ($Na_2Ti_2O_3(SiO_4)\cdot 2H_2O$) is constructed of clusters of four corner-sharing TiO_6

octahedra linked by SiO_4 tetrahedra along two cell axes to form eight-ring pores of alternating octahedra and tetrahedra joined together by corner sharing of the TiO_6 octahedra[36]. The sodium atoms are located both in the pores and in the framework between silicate groups, and some sodium atoms in the pores are replaced by protons due to limited pore volume changing the overall formula to $Na_{1.64}H_{0.36}Ti_2O_3(SiO_4)\cdot 2H_2O$. The tunnel-like pores are reported to be of optimal size for selective removal of caesium ions and the material has been shown to take up caesium over a broad pH range[32,37].

A microporous titanosilicate ETS-10 ($(Na,K)_2Si_5TiO_{13}\cdot nH_2O$) is another well-known ion exchange material with a three-dimensional structure composed of octahedral TiO_6 units linked by bridging oxygen atoms to SiO_4 tetrahedra. The pore structure contains wide channels approximately 8 Å in diameter[38]. Adsorption of heavy metals on to ETS-10 has been well studied over recent years[39–43] including work by Pavel *et al.* on strontium and caesium uptake[44]. Pavel used 0.1 g of ETS-10 in 25ml solutions of Sr^{2+} and Cs^{+} chlorides from 4-9 $meq_M^{n+}\ l^{-1}$ for a contact ratio of 4000 mg/l. These solutions were kept at neutral pH and the exchange allowed to proceed for 24 hours. Pavel concluded that ETS-10 shows a slight preference for Cs^{+} uptake compared to Sr^{2+}. Upon heating of the ion-exchanged ETS-10 it shown via SEM/EDX and XRD that whilst Cs remains homogenously distributed throughout the ETS-10 phase, Sr forms a separate fresnoite-like $Sr_2TiSi_2O_8$ phase. Again this work highlights the different ion exchange behaviour of strontium in comparison to caesium.

Umbite, $K_2ZrSi_3O_9\cdot H_2O$, is another well studied ion exchanger[45–48], which shares a similar pore structure to that of kostylvite (AV-7) one of the main foci of this work. Kostylvite both contain two separate channels, one six-ring of two pairs of corner-sharing tetrahedra joined by corner-sharing octahedra, and a larger eight-ring of alternating corner-sharing octahedra and tetrahedra. Particularly interesting work by Fewox and Clearfield[49] used time-resolved X-ray diffraction to probe the ion exchange process of a concentrated ion exchange solution of Cs^+, 3.3 mM caesium in-situ into protonated umbite, $H_{1.22}K_{0.84}ZrSi_3O_9\cdot 2H_2O$. The conclusions drawn from this work indicated that Cs^+ exchange under these conditions is a two-step process; first the Cs^+ exchange into one site followed by migration into a second more preferable site, which results in a structural change from monoclinic $P2_1/c$ to orthorhombic $P2_12_12_1$. In-situ experiments such as this one, perhaps in conjunction with computer modelling, could potentially prove useful to further investigate the ion exchange mechanisms in these materials and contrast the behaviour of monovalent cations with divalent cations to improve the design of ion exchange materials.

Crystalline silicotitanate (CST, Figure 1.3) has been another heavily studied material, reports demonstrating its selectivity for Cs and Sr and highly crystalline synthesis lead to a great deal of interest in this and other metal-silicates [50,36]. Dyer *et al.* used radiotracers to study the ion exchange properties of CST and a range of other titanosilicates[51]; ETS 10, ETS 4, AM 4 and $Na_2Ti_2SiO_7\cdot 2H_2O$ (Na-CST) were investigated with solutions of ^{60}Co, ^{134}Cs and ^{137}Cs at both pH 7.1 and 5.9. Na-CST showed a significantly higher uptake of isotopes under all conditions. A general trend was observed where the performance of each of the titanosilicates improved with the slightly acidic solutions compared to the neutral solutions of isotopes.

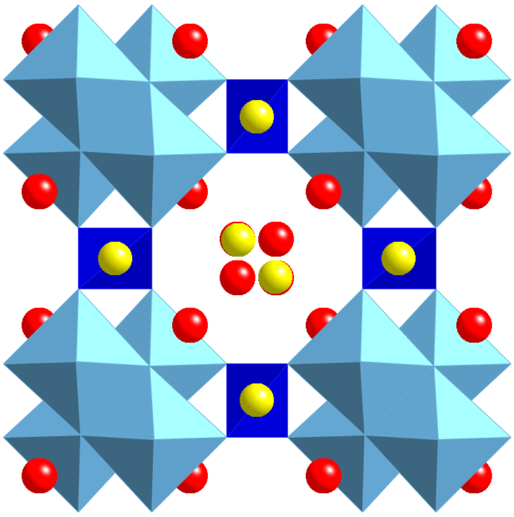

Figure 1. 3 - Crystalline silicotitanate, CST where dark blue tetrahedra are SiO_4 units, cyan octahedra TiO_6 units, yellow spheres Na^+ cations and red spheres water molecules

It has previously been shown that substitution of Ti for Nb leads to an increase in the ion exchange capability[52]. Chitra *et al.* studied Nb-CST ion exchange for ^{90}Sr and ^{137}Cs [53,54] using simulated waste effluents to test the ion exchange ability in a realistic environment. The substitution of Nb for Ti resulted in a significant improvement in the ion exchange capacity for ^{137}Cs. In addition to the doping of niobium into titanosilicates, germanium has also been doped into these materials simultaneously with niobium and shown to retain good, although not necessarily enhanced, exchange properties[35.] The uptake of ^{89}Sr and ^{137}Cs has further been shown to be inhibited by the presence of $NaNO_3$, $CaCl_2$, NaOH and $HNO_{3;}$ in the case of $CaCl_2$ the ion exchange capability is significantly decreased[33]. Whilst CST shows a very high affinity for caesium when the concentrations of competing ions are low, this affinity drops off rapidly as the concentration of these increases past 0.5 mol^{-1} dm^3, which limits the usefulness of this material unless either the material is modified to increase selectivity, or the waste stream is treated to remove calcium and sodium which is not practical. The addition of either NaOH or HNO_3 to alter the pH also results in a decrease in selectivity, however the drop off is not as rapid as with the inclusion of competing sodium or calcium. It is clear that CST, whilst a good exchanger for caesium in pH neutral systems with low concentrations of competitive cations, is not as useful in highly basic/acidic or high sodium/calcium systems.

Strontium uptake was shown to be affected more by the presence of other cations. The presence of sodium ions in a pH neutral solution results in a decrease in strontium uptake and calcium ions result in an even more dramatic decrease. Whilst the uptake appears to be hindered by sodium ions at a neutral pH, the basic solution K_d values remain high, this could potentially be due to a change in the exchange mechanism with varying pH and this facet could warrant further investigation[31].

A comparison of the ion exchange properties of clinoptilolite with a number of other ion exchangers, many of which are produced by UOP, has been made by Marinin and Brown [55]; clinoptilolite, zeolite blend IONSIV® IE-96 (UOP) which consists of a mixture of natural chabazite and Linde A-51 zeolites, IONSIV® TIE-96 (UOP) a synthetic zeolite of undisclosed type modified with titanium, synthetic crystalline materials IONSIV® IE-911(UOP) (a commercially available form of Nb-CST with an added zirconium hydroxide binding agent) and sodium titanate were tested along with a number of organic resins and composite materials. In the case of IONSIV® IE-911 and TIE-96 both demonstrate high distribution coefficients (30000 – 60000) but low selectivity when competing calcium cations are introduced, however, due to such a high uptake these materials can still be of use with regards to waste streams with low levels of competing cations. The zeolite materials exhibit a drastic Decrease in strontium uptake noticeable with an increase in calcium concentration, distribution coefficients drop from tens of thousands down to a few hundred; however, the selectivity remains high due to selective sorption occurring rather than ion exchange. The composite and resin materials were noted to have significantly lower distribution coefficients, by 2 orders of magnitude, but superior selectivity and kinetic properties in most cases.

1.4 Potential materials for ion exchange – scope of this work

Whilst there are a number of different material types to study for ion exchange as previously discussed, the work reported in this thesis focussed on metal-silicate materials due to the flexibility of this system in terms of connectivity of polyhedra for structure and the possibility for isostructural substitutions, and the vast number of different structures possible as evident by the number of natural minerals based on silica tetrahedra with metal octahedra.

Natural minerals and the respective synthetic analogues have also been examined for ion exchange properties. As new mineral structures are discovered synthetic equivalents are reported and these materials are often investigated for a variety of possible applications. Of particular interest would be a natural mineral, noonkanbahite[56] , which is related to the shcherbakovite and batisite materials with the formula $BaKNaTi_2Si_4O_{14}$. This structure has yet to be synthesised or the ion exchange properties investigated. An interesting feature is a range of different size cation sites, which could potentially allow for selective uptake of a number of different cations on to the different sites.

The synthesis of zirconosilicates has been widely studied[57–59] and a number of materials have been produced which could be potential ion exchange materials. The great number of these structures gives a wide variety of pore sizes determined by the motif of tetrahedra and octahedra in the pores. It is also worth noting that there are a number of materials isostructural to zirconosilicate minerals with the zirconium switched for a different metal such as tin[60]. The size difference in metal octahedra could potentially allow for slight modifications to the pore size.

$Na_2ZrSi_2O_7{\cdot}H_2O$, Figure 1.4, has been well characterized structurally, but little work has been performed to investigate ion exchange properties. Many metal silicates have shown good resistance to radiation damage and high pH stability, thus they could prove to be an interesting class of materials for investigation[61,62]. Furthermore recent work has shown that potentially desirable waste form phases can be achieved by thermal treatment converting to a new phase[63].

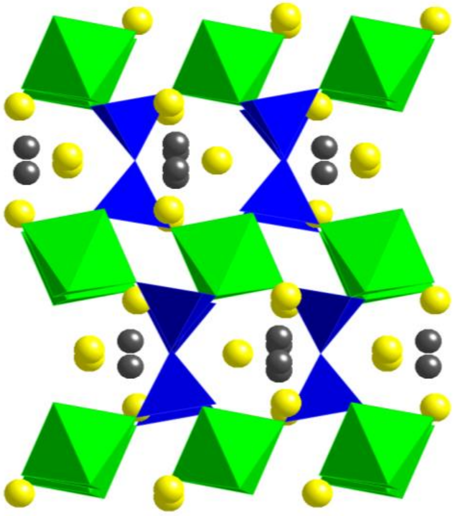

Figure 1. 4 - - $Na_2ZrSi_2O_7{\cdot}H_2O$ viewed along [100]. Na^+ sites are indicated by yellow spheres, and water sites by grey spheres. The pore diameter is approx. 4.7Å

Analogues to the natural minerals umbite, elpidite and petarasite[64,65] offer possible materials which could potentially be useful for ion exchange. These materials have been structurally characterised and have been shown to have channels in the region of 2-6 Å diameter, with both Na^+ and K^+ ions and shared sites which would suggest a possible affinity for Sr^{2+} as the ionic radius is between that of Na^+ and K^+.

Petarasite, Figure 1.5, $Na_5Zr_2Si_6O_{18}(Cl,OH)\cdot 2H_2O$, a synthetic form of which is termed AV-3 has been recently prepared by Lin *et al*[66] . AV-3 is of some interest due to the presence of Cl^- and HO^- which could potentially result in a capability for anion exchange in addition to cation exchange.

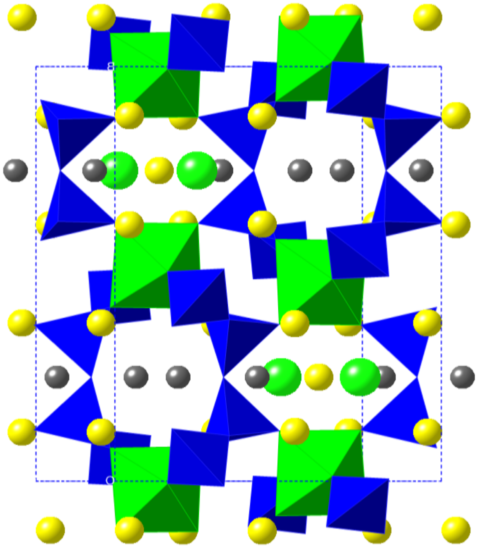

Figure 1. 5 - Petarasite viewed along [001], showing the Cl- sites as green sphere, Na+ sites as yellow spheres and the water molecules are indicated by grey spheres. The diameter of the pore size is approx. 4.6 Å

There has been limited published work on the ion exchange properties of these materials, however, one such paper demonstrated how the ion exchange capability of the material umbite, $K_2ZrSi_3O_9\cdot H_2O$, depended greatly upon the pH of the system [32]. A series of materials based on $K_2ZrSi_3O_9\cdot H_2O$ where framework Zr has been substituted for Ti in various amounts (12. 25, 37, 50 and 75% Ti) were prepared along with protonated forms such as $K_{0.3}H_{1.7}TiSi_3O_9\cdot 2H_2O$ and $K_{0.5}H_{1.5}TiSi_3O_9\cdot 2H_2O$, by Clearfield *et al.*[32] to investigate the selectivity of these ion exchange materials for Li, Na, K, Rb and Cs under a range of pH conditions. The ion exchanges performed in this work took place over 10 days using concentrations of 0.05 M MCl-MOH (M=Li, Na, K, Rb, Cs) at room temperature. Clearfield found that doping Ti into the framework thus reducing the size of the channels resulted in a greater preference for potassium uptake from pH 2-6 whereas the more Zr-rich silicate exhibited a preference for rubidium and caesium cations. This work illustrates the link between pore/channel size and cation specificity and shows it to be an important factor when considering an ion exchange material and how to modify one to improve ion exchange properties. In the case of Cs^+ it was reported that at pH 3.0 the uptake was 0.75 mequiv/g. which increased to a maximum of 2.0 mequiv/g. at pH 12. The uptake of potassium and sodium, however, are favoured over that of caesium over all pH ranges, with potassium being the most favoured. The uptake begins at a pH above 2, and increases to 1.3 mequiv/g. at pH 4 but increases suddenly after pH 6 where the uptake jumps to 4 mequiv/g. The uptake increases further as the solution becomes basic up to a maximum of 5.3 mequiv at pH 9 after which the uptake plateaus.

This research indicates how important the pH of the system is on the ion exchange. It should be noted that in the real world application of these materials in the nuclear industry, the pH of waste steams can vary widely and so good ion exchange properties over a wide range of pH is a very desirable property.

Stannosilicate materials have been less rigorously studied, with little to no work done on the synthesis of these materials. Of particular interest is a material termed AV-7[60] , with the ideal formula $NaKSnSi_3O_9 \cdot H_2O$, Figure 1.6. The first synthesis was reported by Corcoran in 1992 before Rocha *et al.* reported the structure in 2000. Of some interest is the presence of shared

Na^+ and K^+ sites, which as previously mentioned, could indicate an affinity for Sr^{2+} exchange. Furthermore, the structure reportedly has 4 Å channels in one dimension as opposed to fully enclosed cages within the structure, which would be more difficult for cations to access. Ion exchange studies have yet to be carried out on this material, so further investigation is warranted.

Other materials which have been reported, but have not as yet been investigated with ion exchange in mind include a synthetic tin equivalent of the natural mineral Penkivlksite-1*M* (ideal formula $Na_2TiSi_4O_{11}\cdot 2H_2O$), AV-13 ($Na_{2.26}SnSi_3O_9Cl_{0.26}\cdot xH_2O$) and hafnium substituted equivalents [67–69]. The substitution of hafnium into the structure could possibly be an interesting factor to investigate with respect to the effect upon ion exchange properties. Hafnium being significantly larger than tin, could potentially open up the channels of the structure even further, also this material, as in AV-3, exhibits both anions and cations in the channels. This is another interesting factor, and whilst the group mentions forthcoming research on the possible ion exchange of nitrate anions into the structure no other anion exchange is mentioned.

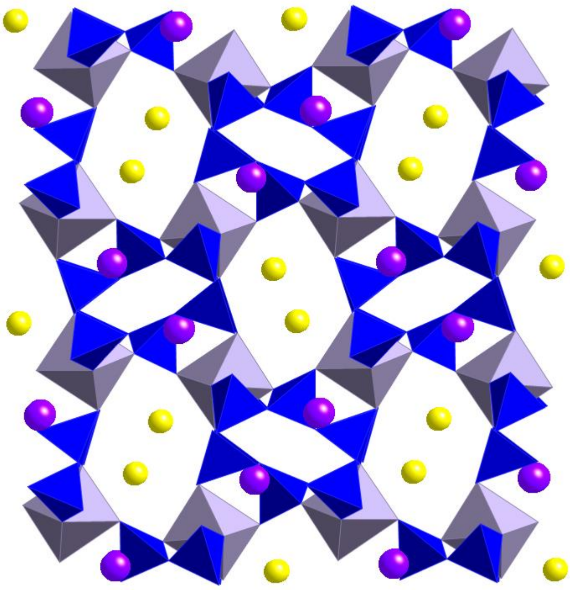

Figure 1. 6 - AV-7 viewed along [100]. K^+ sites are indicated by the purple spheres and the Na^+ and K^+ shared sites indicated by the yellow spheres. The pore diameter is approx. 5.1 Å

Chapter2: Experimental

2.1 Synthesis techniques

2.1-1 Solid state synthesis

The solid state synthetic approach is the most well used method for materials chemistry primarily due to its simplicity; reactants are ground together in a mortar and pestle before sintering at high temperature (often >1000°C). As this relies upon surface contact between reactants regrinding and heating is often necessary to ensure a phase pure product. Direct heating of solids often yields phases which are more condensed than those obtained via hydrothermal routes however, so this route is not often employed when seeking porous materials.

2.1-2 Sol-gel synthesis

The sol-gel method involves the preparation of a sol, a colloidal suspension of metal oxide particles in an alcohol solvent from a precursor, typically a metal alkoxide. The sol is then hydrolysed so as to form a gel which can then be aged to ensure completion of the reaction.

After ageing the gel can be dried to form a porous rigid network, which is then able to be heated at lower temperature compared to solid state reactions.

2.1-3 Hydrothermal synthesis

Hydrothermal and solvothermal synthesis are techniques where by liquids and gels are heated within a sealed chamber to generate pressure in order to crystallize materials from solution. Typically water is the most common solvent used, however alcohols[70] and ionic liquids[71] can also be used if the user is mindful about the pressure generated in the case of ethanol. Pressure is usually generated autogenously, so that the saturated vapour pressure of the solvent and the level of filling determine the pressure at a given temperature.

The phases produced through hydrothermal techniques often differ, particularly in phase density, from those obtained via solid state routes primarily due to the presence of water/solvent but also due to the initial gelling process and the presence of any mineralizers such as F^- ions which can also greatly influence the crystallization process.

Due to starting mixtures often being highly basic or otherwise corrosive, in the typical hydrothermal autoclave a resistant material such as PTFE is often used to contain the reagents, which also has the advantage of good mechanical properties up to 270°C and 150 bar. This vessel in turn typically resides within a steel body with a safety pressure release system in case of higher than expected pressure.

In the course of this work Parr (model 4749, 4744 and 4748) acid digestion vessels with PTFE liners were used.

2.1-4 Microwave synthesis

Microwave heating is distinctive in that it produces even heating throughout a material unlike conventional convection heating ovens which rely on the thermal conductance of a material to heat the centre, which can often result in a large temperature gradient throughout a large object. Furthermore heating can be applied more directly to a material as only a polarizable material will be heated, so no energy is wasted heating air. This can enable very rapid synthesis of some materials, as some zeolites have been shown to be formed by heating for as little time as 10 minutes compared to conventional heating which often takes days.

For this work a CEM MARS6 microwave was used along with EasyPrep acid digestion vessels which comprise a PTFE vessel charged with the reactant gel within a composite sleeve, secured closed with an HDPE screw mechanism. Various crystallization times were investigated over the course of the work ranging from 30 minutes to 8 hours, the temperature for all these reactions was set to 230°C controlled using an immersed temperature probe. Pressure of the vessels could not be directly controlled or measured and so vessels were always filled to the same level (45 ml).

2.2 Characterization techniques

2.2-1 Fundaments of crystallography and diffraction

A crystal is a solid with a regularly repeating arrangement of atoms, the smallest representation of the repeating pattern is termed the unit cell. The unit cell is described by the lengths a, b, and c and angles α, β, and γ, which are referred to as the lattice constants. The relationships between the lattice parameters result in the 7 crystal systems, which when combined with the one of the lattice centrings give a total of 14 Bravais lattice types[72]:

- cubic ($a=b=c$, $\alpha=\beta=\gamma=90°$)
- hexagonal ($a=b<c$, $\alpha=\beta=90°$ $\gamma=120°$)
- orthorhombic ($a\neq b\neq c$, $\alpha=\beta=\gamma=90°$)

- monoclinic($a \neq b \neq c$, $\beta \neq \alpha = \gamma = 90°$)
- rhombohedral ($\alpha \neq \beta \neq \gamma \neq 90°$)
- tetragonal ($a = b \neq c$, $\alpha = \beta = \gamma = 90°$)
- triclinic ($a \neq b \neq c$, $\alpha \neq \beta \neq \gamma$)

Combining the Bravais, lattice types with the 32 crystallographic point groups gives a total of 230 space groups, which all three dimensional unit cells must correspond to. The crystal can be described in terms of planes, described by the inverse of the fractional intercept (*hkl*) with the axis *a*, *b*, and *c*; so a plane bisecting halfway between the *a* axis and not intercepting either *b* or *c* would be the (200) plane.

Subsequent to the discovery of crystalline solids diffracting X-rays by Max von Laue in 1912, William Lawrence and William Henry Bragg developed the first diffractometers based on the observation that when X-rays interact with atoms in a set of parallel planes separated by a distance *d*, the scattered X-rays can interfere constructively or destructively, giving rise to Bragg peaks, according to the incident angle θ as per Braggs law[73] shown in Equation 2.1 and Figure 2.1;

$$n\lambda = 2d_{hkl} \sin \theta \qquad (2.1)$$

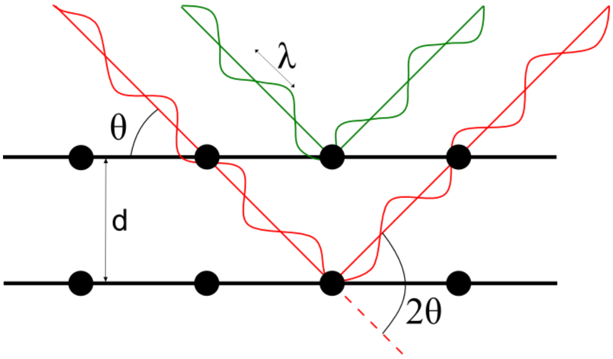

Figure 2. 1 - Diffraction through two rows of atoms[74]

When considering a single crystal it is simplest to examine the diffraction in terms of the reciprocal lattice and Ewald sphere; a sphere of radius 1/λ, where λ is the wavelength of the incident radiation on a crystal is termed the Ewald sphere. This represents the experimental conditions possible as a range of 2θ possibilities. The reciprocal lattice represents the scattering possibilities of the crystal. In the case of a 3D crystal the lattice would take the form of a series of points labelled with Miller indices corresponding to the planes at which diffraction will occur. Combining the Ewald sphere[75] and reciprocal lattice, Figure 2.2, will indicate how diffraction will occur when a point on the reciprocal lattice intersects with the sphere. The diagram below depicts the case of a crystal orientated to cause diffraction on the (–2,4,0) plane, the vector joining the origin to the reciprocal lattice point denoted, $d^*$is the reciprocal lattice spacing which is equal to exactly 1/*d*.

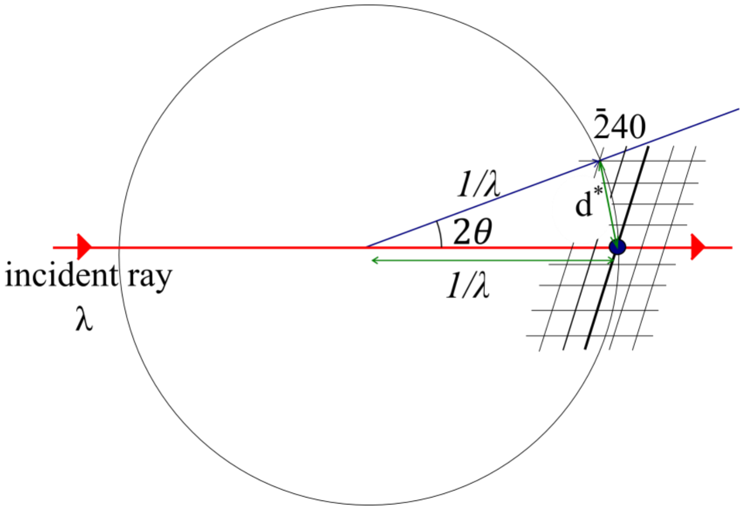

Figure 2. 2 - Reciprocal lattice over an Ewald sphere construction[74]

In the case of powder diffraction, the powder can be considered a collection of randomly distributed crystallites in all possible orientations are represented each of which diffracts independently. This results in cones of diffracted X-rays, termed Debye-Scherrer cones, Figure 2.3, which can be recorded by the detectors of diffractometers.

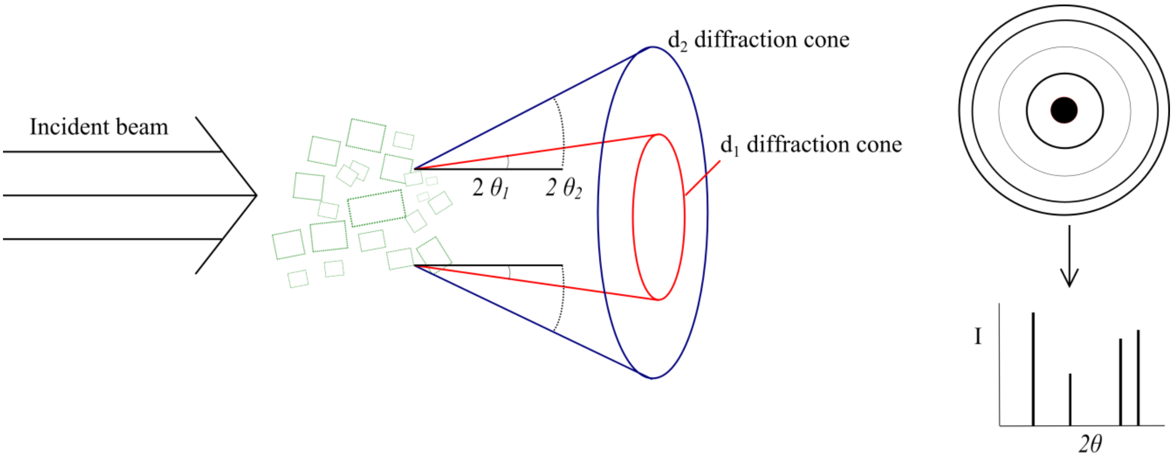

Figure 2. 3 - Debye Scherrer cones[74]

When the wave is diffracted by the plane of a crystal it can be described as a vector with an amplitude and phase with sine and cosine components. The intensity of the reflection from an ideal crystal with an ideal detector can be given by the sum of the scattering factors of the atoms on the plane with this phase component[74,76].

$$F(S) = \sum_{n} f_n e^{2\pi i(hx+ky+lz)} \tag{2.2}$$

where,

- $F(S)$ is the observed intensity (structure factor)
- f_n is the atomic scattering factor of the atoms in the plane of the unit cell

However, it is necessary to include a number of additions to this as the previous equation only considers an ideal crystal.

Multiplicity, j

As powder diffraction depends on the random distribution of crystallites, any set of Bragg planes with the same *d*-spacing will have a number of crystallites orientated for diffraction at 2θ, thus for reflections which have symmetry equivalent reflections (e.g. the (111) NaCl reflection has 7 other equivalent reflections) all of these equivalent reflections will contribute at the given angle.

Polarisation factor, *P*

Polarisation of the diffracted X-ray can change, the degree of which is dependent upon the initial polarisation of the X-ray being in plane or out of plane with the scattering. When the polarisation is perpendicular to the plane of scattering there is no change in intensity over 2θ, when in the plane of scattering, there is a drastic effect on the observed intensity over 2θ with the intensity being 0 at 2θ=90°. Unpolarized X-rays, as used by laboratory diffractometers, being a mixture of the two previous cases have a reduction centred on 2θ=90°. Use of a monochromator can also reduce the loss in intensity as the degree of polarization depends upon the diffraction angle of the monochromator, $2\theta_M$.

Polarization in plane : $P = 1$

Polarization perpendicular to plane: $P = cos^2 2\theta$

Unpolarized X-rays: $P = (1 + cos^2 2\theta)/2$

Unpolarized X-rays with a monochromator: $P = (1 + cos^2 2\theta\, cos^2 2\theta_M)/(1 + cos^2 2\theta_M)$

Lorentz factor, *L*

Whilst Bragg's law implies that diffraction only occurs when the equation is satisfied exactly, in practice λ and *d* will have a degree of spread so that diffraction occurs over a range of angles centred on a mean, 2θ. This can be explained by considering reciprocal space; a point in the lattice remains on the Ewald sphere for a time period during the measurement process, these points are small but possess a size inversely proportional to that of the crystallite. When the detector scans though 2θ, the time the reciprocal lattice space spends in a diffracting position on the Ewald sphere has an angular dependence; higher angle lattice vectors cut the Ewald sphere close to a tangent and thus spend longer in a diffracting position increasing their intensity.

This results in a diffraction peak not being a delta function but being a curve with a height and width with an angular dependence:

$$L = c/(sin\theta\ sin2\theta) \tag{2.3}$$

Where c represents a constant; in the case of diffraction the value of the constant is unimportant as only the relative intensities are of consequence.

Absorption, *A*

As X-rays pass through matter they are absorbed according to an exponential law:

$$I = I_0 e^{-\mu t} \tag{2.4}$$

where I_0 is the incident intensity, I is the reduced intensity after travelling distance t through a material with an absorption coefficient μ. The importance of this effect is dependent upon the geometry of the experiment conducted; in reflection geometry the absorption is unimportant as when all possible path lengths are taken into account the net absorption is constant with θ.

Temperature

The temperature affects the intensities in a more complex fashion as the effect changes from atom to atom in the structure. Modifying the atomic scattering factors to add isotropic displacement is a simple way to include this influence in the structure factor equation:

(2.5)

$$f_T = f\,\exp(-Bsin^2\theta/\lambda^2)$$

where T is temperature and B = $8\pi^2\langle u^2\rangle$, $\langle u^2\rangle$ being the mean square displacement of an atom from its average position. These B factors, also termed Debye-Waller factors , increase with temperature.

The first four of these factors can be used as simple multiplicative corrections with an additional constant representing other influences such the sensitivity of the detector, so that:

$$I_{hkl} = cjPLA\,{F_{hkl}}^2 \qquad (2.6)$$

The temperature factor, however, must be included in the structure factor equation as a modified atomic scattering factor:

$$F(S) = \sum_n f_n N_n \exp\{2\pi\, i\,(hx + ky + lz)\}\exp(-Bsin^2\theta/\lambda) \qquad (2.7)$$

Modern diffractometers generate X-rays beams through an X-ray tube, a sealed vacuum tube containing a metal filament cathode and a water cooled anode. By way of a large potential difference, electrons are accelerated towards a metal target resulting in the excitation of the electrons within the metal leaving vacancies to be filled by higher energy electrons. The relaxation of these electrons results in the emission of an X-ray and heat.

The transitions between electron shells of a target metal produce characteristic X-rays of that transition. For copper when an electron drops from the *L* shell to a *K* shell, the $K_{\alpha1}$ emission has a wavelength of 1.5406 Å.

A continuum of background radiation termed Bremsstrahlung (braking radiation) is also observed due to the rapid deceleration of electrons when they are fired at a metal target and deflected by a charged particle. The decrease in the kinetic energy of the electron necessitates the emission of electromagnetic radiation in order to conserve energy.

Many diffractometers are fitted with monochromators either immediately after the X-ray tube and/or before the detector as seen in Figure 2.4. monochromators ensure a wavelength of as narrow a range as possible, a material where the absorption edge falls between the K_α and K_β of the target material is used, so that it acts as a filter decreasing the intensity but ensuring monochromatic radiation is obtained. In lieu of a metal filter type monochromator, a single crystal, typically of germanium, silicon or quartz, set at a specific angle can be used to collect monochromatic radiation according to Bragg's law[72].

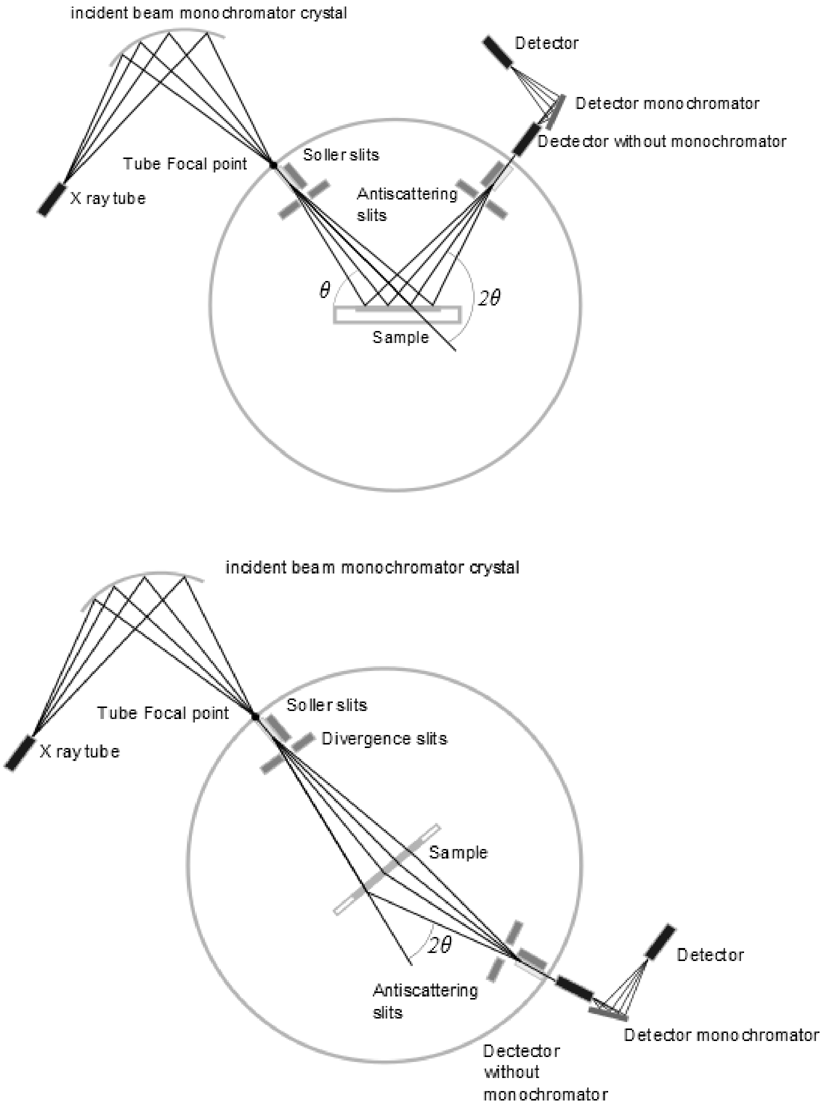

Figure 2. 4 - Reflection (top) and transmission (bottom) geometry for X-ray diffractometers[52]

2.2-2 Neutron diffraction

Whilst neutron-mass scattering is relatively weak in comparison to X-rays, neutron diffraction still proves to be a useful technique. The scattering of neutrons is based upon the nucleus of an atom, as opposed to the electrons in the case of X-rays. This allows for better sensing of lighter atoms, particularly when in the presence of heavier ones. Furthermore neighbouring elements on the periodic table and even different isotopes of the same element often have significantly different scattering cross sections which allows for better differentiation. However due to the weak scattering, large sample sizes are required and the signal-to-noise ratio is typically much weaker than in XRD.

Neutrons are typically generated in one of two ways: from a nuclear reactor or from a pulsed spallation source. Neutrons generated from reactors, termed ‘thermal neutrons’, typically have a wide range of energies and so a moderator material, such as water or graphite is necessary to slow the neutrons down in addition to a crystal monochromator to select the desired wavelength. In the case of a spallation source neutrons are generated by bombarding a metal target (e.g. Pb, Ta or Hg) with energetic particles such as protons accelerated up to 1 GeV.

ISIS at the Rutherford Appleton Laboratory, the facility used in this work, generates neutrons via spallation, using a particle accelerator to fire a pulsed beam of protons at 0.8 GeV at a tantalum target. The pulsed polychromatic nature of the neutron beam lends itself to collecting data via a time of flight (ToF) method rather than varying the energy of the beam or the angle of the detector. As the wavelength of a neutron is related to the energy via equation 2.8;

$$\lambda = \left(\frac{h^2}{2mE}\right)^{\frac{1}{2}} = \frac{9.04}{E^{\frac{1}{2}}} \tag{2.8}$$

where λ is in Å and E is the energy of the neutron in meV and the mass m is taken as $1.675\text{x}10^{-27}$ kg. The wavelength is related to the velocity of neutron and thus the time of flight along a known path. Substituting in values in to equation 2.8 gives;

$$\lambda = \frac{0.003955}{\mathrm{v}} = \frac{0.003955 \cdot T}{L} \tag{2.9}$$

where v is in m(μs)$^{-1}$, T in μs and L in m. This gives a linear relationship between the neutron wavelength and the time of flight.

The High Resolution Powder Diffraction beamline (HRPD), as shown in Figure 2.5, was the instrument used to collect data in this work. HRPD is an example of a ToF beamline: The detectors are fixed at set angles and collect the scattered polychromatic neutrons over a period of time discriminating by time of arrival.

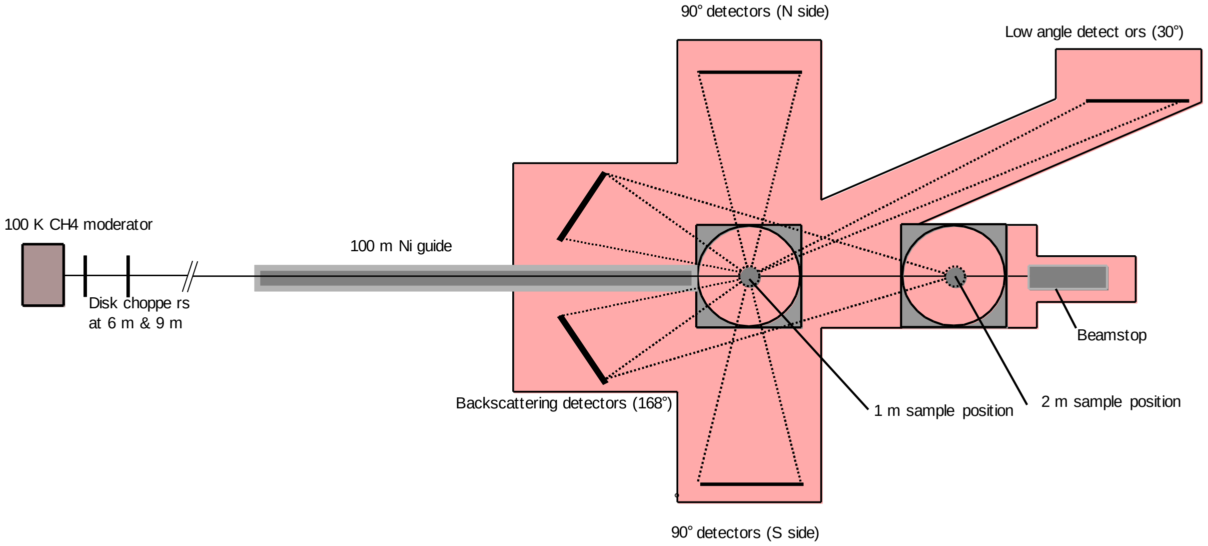

Figure 2. 5 - Schematic diagram of Isis HRPD [6]

2.2-3 Rietveld refinement

The ‘Rietveld method’ is a process to obtain an accurate crystal structure from powder diffraction data using a “whole pattern fitting” method, each element of the powder pattern is broken down into a number of parameters, which can be refined or fixed by the user.

Firstly a crystallographic model is necessary which contains the lattice parameters, space group, atom positions and instrumental parameters such as the wavelength of radiation used. This model is used to generate a calculated pattern, and the parameters are refined to minimise the difference between the observed and calculated pattern via a least-squares method[74,77]:

$$S_y = \sum_{i=1}^{n} w_i (y_i - y_{ci})^2 \qquad (2.10)$$

where S_y is the residual, the quantity minimised by the refinement

w_i the weighting factor,

y_i and y_{ci} the observed and calculated intensities at the i^{th} step.

The calculated intensity is the sum of all Bragg reflections within a range:

$$y_{ci} = s \sum_{K} L_K \left| F_K{}^2 \right| \emptyset_i \,(2\theta_i - 2\theta_K) P_K A - y_{bi} \qquad (2.11)$$

where;

s is the scale factor

A is the absorption factor

$\emptyset$ is the reflection profile function

K represents the Miller indices hkl

L_K is the Lorentz polarization factor

F_K is the structure factor

P_K is the preferred orientation function

y_{bi} is the background intensity

The total profile function can be described as a convolution of instrumental and sample parameters:

- Axial and equatorial divergence;
- Emission profile;
- Sample size and shape broadening;
- Sample strain broadening.

The information contained within the peak shape (profile) is not always of consequence to obtaining a structural model and so three approaches to the modelling of the peak shape are used:

- Empirical peak shapes, where whichever function which best fits the data is used;
- Fundamental parameters, where the instrumental and sample contributions to the profile are known and entered into the refinement;
- Semi-empirical, where the instrumental contributions are modelled empirically and convoluted with sample contributions which can be refined;

In the case of empirical profile modelling, a convolution of Gaussian and Lorentzian functions with a number of refinable parameters, typically a pseudo-Voigt function, is used to describe the profile.

The mathematical agreement between the observed and calculated patterns can be ascertained by a number of functions:

$$R_{wp} = \left\{ \frac{\sum_i w_i [y_i - y_{ci}{}^2]}{\sum_i w_i [y_i]^2} \right\}^{\frac{1}{2}} \tag{2.11}$$

$$R_{exp} = \left\{ \frac{(n - p)}{\sum_{i-1}^{n} w_i y_i{}^2} \right\}^{\frac{1}{2}} \tag{2.12}$$

$$\chi^2 = \left(\frac{R_{wp}}{R_{exp}} \right)^2 \tag{2.13}$$

where R_{wp} is the weighted profile function,

R_{exp} is the expected R-factor

w_i the weighting factor

y_i and y_{ci} the observed and calculated intensities at the i^{th} step

However, these factors are only indicative of how good the fit is in a mathematical sense, it is possible for a local minima to have a good fit but make no chemical sense thus it is important to ensure that any structural model exhibits sensible bond distances and angles.

2.2-4 X-Ray Fluorescence Spectrophotometry

X-ray fluorescence is a technique to measure the elemental composition of a sample. Where XRD involves the processes where X-rays are scattered by electrons, XRF detects processes which occur when X-rays excite electrons. When a core electron is excited by an X-ray a positive hole is left in the shell which can be filled by relaxation of an electron in a higher level shell due to attraction to the nucleus. This relaxation can result in the emission of a photon characteristic of that electronic transition[78] as seen in Figure 2.6. The emission of these X-rays is governed by the following quantum mechanical selection rules[79]:

- $\Delta n \geq 1$
- $\Delta l = \pm 1$
- $\Delta j = \pm 1$

where: n is the principal quantum number, l is the angular quantum number, j is the total momentum $j=l+s$; and s is the spin quantum number.

Based on these selection rules for the K series p→s transitions are allowed giving rise to two lines, the l series lines allow p→s, s→p and d→p transitions.

The photon emitted produces a spectral line which is named according to the original vacancy shell and how many shells above this the higher energy electron dropped down by; so an electron dropping to the K (1s) shell from the L(2s&2p) shell one level above would be termed the Kα line.

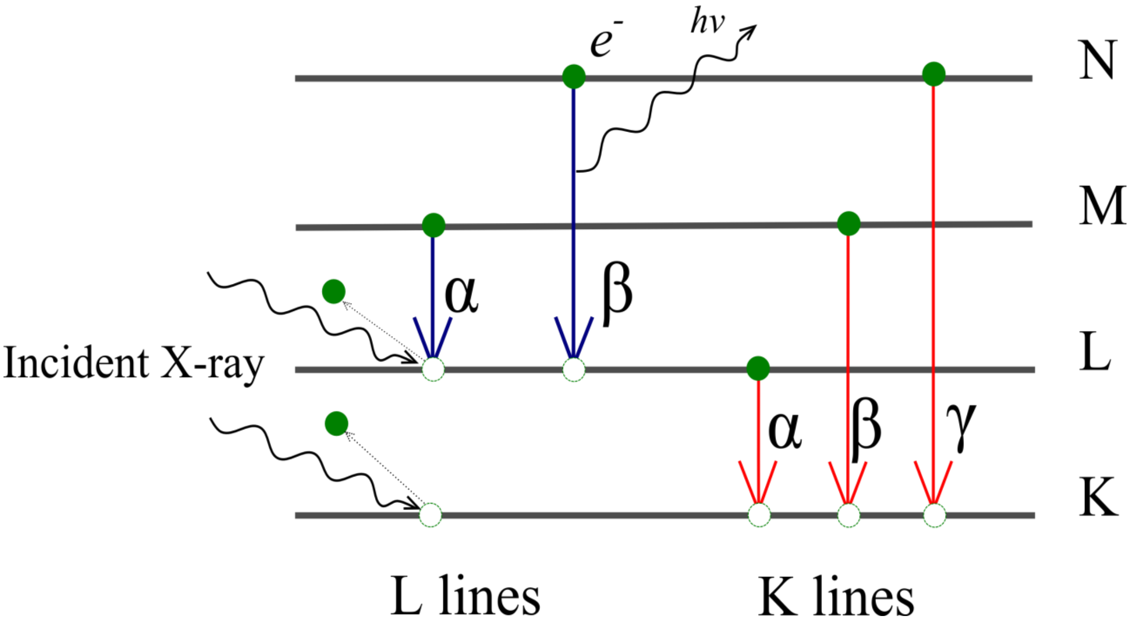

Figure 2. 6 - photoelectric effect resulting in fluorescence

The intensity of the line will correspond to the quantity of that element in the sample, thus it is necessary both to measure the intensity of lines as well as differentiate the different energies. There are two main approaches for this, energy dispersive or wavelength dispersive. In the case of energy dispersive (EDX), a solid state Si detector is used which is capable of measuring both the intensity and energy level of emitted X-ray photons. The ionisation caused by the photons on the Si measured by a series of electrodes. The energy dispersive spectrometers typically have high count rates due to collecting a large portion of emitted photons, but poor energy resolution. EDX detectors can suffer from two particular artifacts, escape peaks and sum peaks. Escape peaks occur when X-rays undergo photoelectric adsorption in-to the detector material and emit photoelectrons and X-rays characteristic of the detector material, commonly of 1.75 keV from Si detectors, which are picked up by the detector. Any fluorescence peaks of energy E are accompanied by escape peaks of energy E-1.75 keV. Sum peaks occur when multiple X-ray photons collide with the detector simultaneously which creates an electron pule which is measured as the sum of these two collisions creating lines of multiples of the true fluorescence energy.

Wavelength dispersive (WDX) spectrometers use detectors which only measure the intensity of emissions and use a series of crystal monochromators and focusing optics in order to filter the beam and measure only one wavelength of X-rays at a time, this enables a greater energy resolution but due to the use of monochromators some intensity is lost.

Measured intensities depend not only on the concentration of the analyte element but also the concentration of all other elements present (matrix), the sample type (solid, liquid or powder), method of sample preparation, shape and thickness of the sample. A simplified equation for relating the measured intensity to the weight fraction of an analyte is as follows:

$$I_i = k_i W_i + b_i \tag{2.14}$$

where:

I_i is the radiation intensity

k_i is a constant

W_i the weight fraction

b_i is the radiation intensity when the analyte concentration is zero

k_i and b_i are fitted constants determined via a least squares method on the basis of reference samples.

Matrix effects such as absorption and enhancement are also important factors to consider and thus a new term is added, M_i, when greater than 1 this indicates absorption of radiation by the matrix to be the dominate effect. When smaller than 1 enhancement is the dominant effect.

Absorption effects occur when the fluorescence of the analyte element is sufficient to excite an element from the matrix, i.e. the absorption edge of a matrix element is slightly less than the characteristic line of an analyte element. The strength of this effect is determined by the relative absorption of the matrix and sample. If the matrix element has stronger absorption than the sample the effect is far greater. The enhancement effect or secondary fluorescence occurs when a matrix element emit radiation of slightly higher energy than the absorption edge of the analyte element.

In reality the equation for intensity is significantly more complex. If a sample is “infinitely thick” so that transmittance is zero the intensity equation[79] can be written as:

$$I_i = \frac{d\Omega}{4\pi sin\emptyset_1} Q_i q_i W_i \int_{\lambda min}^{\lambda edge} \frac{\tau_i(\lambda) I_0(\lambda)}{\chi(\lambda,\lambda_i)} \left(1 + \sum_j W_j S_{ij}\right) d\lambda \tag{2.15}$$

$$S_{ij} = \frac{1}{2} q_j \tau_j(\lambda) \frac{\tau_i(\lambda_j)}{\tau_i(\lambda)} \left[ln\left(1 + \frac{\mu(\lambda)}{\mu(\lambda_j) sin\emptyset_1}\right) \frac{sin\emptyset_1}{\mu(\lambda)} + ln\left(1 + \frac{\mu(\lambda_i)}{\mu(\lambda_j) sin\emptyset_2}\right) \frac{sin\emptyset_2}{\mu(\lambda_i)} \right] \tag{2.16}$$

where:

$d\Omega$ is the differential solid angle for the radiation, added as a geometric term for the irradiated surface area of the sample

q_i is the sensitivity of the spectrometer for the characteristic line for analyte i

W_i and W_j are the weight fractions for analyte i and matrix element j

λ_{min} and λ_{edge} are short wavelength limit and wavelength of the analyte absorption edge respectively, to integrate the area under the characteristic line

$\tau_1(\lambda)$ is the photoelectric absorption coefficient for analyte i and wavelength λ, to take account of the absorption of the sample

$I_o(\lambda)$ is the intensity of the primary radiation

$\chi(\lambda, \lambda_i)$, $\mu(\lambda)$ and $\mu(\lambda_i)$ are total mass-attenuation coefficients of the samples and specimens for incident and fluorescent radiation to account for the Cöester-Kronig transition probabilities (where an electron from a higher subshell fills a vacancy in the same shell and an Auger electron is emitted) if the L_α or L_β lines are used.

S_{ij} is the matrix enhancement term as described above

Obviously the matrix effect is non-trivial but this shows how there is some dependence between the different compounds as the weight fractions rather than each analyte being treated individually with no consideration of other species present.

2.2-5 Scanning Electron Microscopy (SEM)

Similar to when an X-ray is incident upon a material, when an electron beam is used a number of effects are observed as depicted in Figure 2.7:

- Secondary electrons are emitted from which topological information can be gathered
- Auger electrons are emitted when a higher electron drops down to fill the hole left by the excited electron, from which the surface sensitive composition can be examined as these electrons are of characteristic energy of an element and would be reabsorbed by the bulk sample;
- Backscattered electrons, which can give topological information;
- Characteristic X-rays are emitted from transitions in a similar fashion to XRF which give compositional information;
- Cathodoluminescence – where an electron is incident upon a luminescent material and results in the emission of a photon of energy in the visible region.

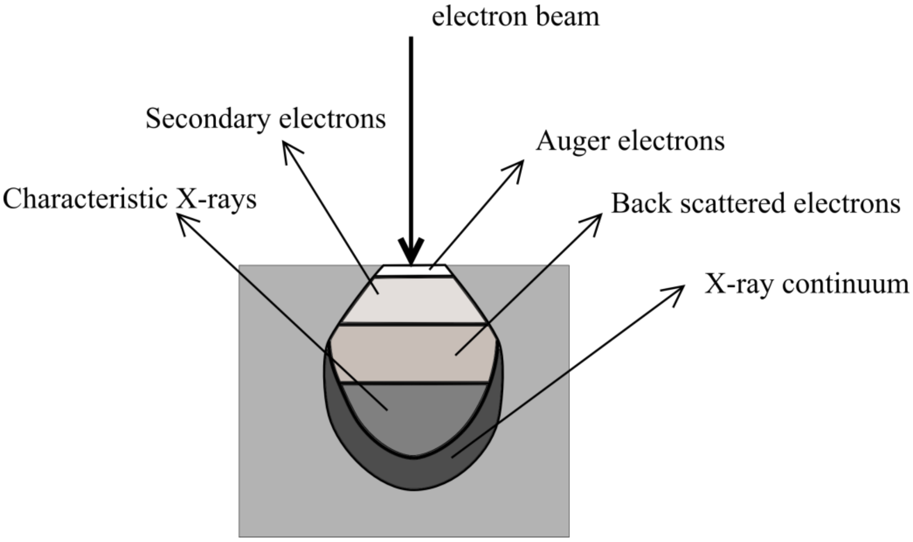

Figure 2. 7 - Penetration depth of electron beam and resultant emissions

Secondary electron detection is most commonly used for generating images. The number of secondary electrons detected is a function of the angle between the surface and the beam, thus images can be generated by the scanning across a sample with the electron beam in two dimensions. Emitted secondary electrons are often of lower energy (<50 eV) so that only those from the top surface (within a few nanometres) reach the detector before being reabsorbed.

Backscattered electrons (BSE) present another way to gather topographical information about a sample. These are higher energy electrons which undergo one or more scattering events and escapes from the surface with energy greater than 50 eV. In addition to topological information, BSE offers some degree of compositional information as well since the degree of backscattering is dependent upon which element the electron collides with, higher atomic numbers resulting in a greater proportion of backscattering due to a more highly charged nucleus. Whilst offering greater elemental contrast in images, BSE offer poorer resolution than secondary electrons. The higher energy of these electrons prevents them from being reabsorbed by the sample leading to a contribution from a larger sample area.

Characteristic X-rays are generated in a similar fashion to in XRF. A higher energy electron drops down in energy, emitting an X-ray photon in the process, to fill a positive hole left by a displaced electron excited by the incident beam, in this case an electron beam rather than X-ray beam. Energy rather than wavelength dispersive spectroscopy is more common when used in conjunction with SEM.

2.2-6 Ion Chromatography

Ion chromatography is a technique used to separate ions from a mixture in solution by using mobile and stationary phases which the ions interact with to different degrees.

The stationary phase consists of a solid medium presenting a charge opposite to that of the analyte ions so that the ions are attracted to the column. In the case of the system used in this work, a schematic shown in Figure 2.8, (Dionex ICS-1000) the column comprises a resin with quaternary ammonium ions.

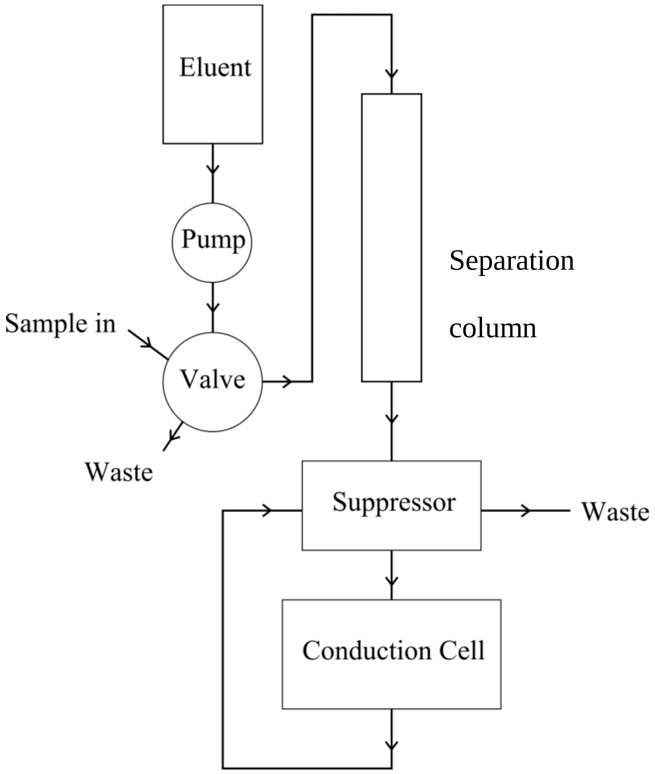

Figure 2. 8 - Schematic of Ion chromatography system

The mobile phase is used to push the analyte through the system; in this work dilute methylsulphonic acid (~0.275%) was used as the eluent. The analyte ions will be bound to the stationary phase until the increase in concentration of the eluent becomes high enough to exchange with them. This is referred to as the retention time of the ion; the more highly charged or polarizable a cation the longer the retention time.

Once through the column ions pass into a conductivity cell shown in Figure 2.9, where two stainless steel electrodes measure the conductance, in order to generate a signal.

The conductance of the eluent is minimised by the use of a suppressor, where water is electrolysed and forms O_2 gas and hydronium cations in the anode chamber, and H_2 gas and hydroxide ions in the cathode chamber. Due to an applied potential, eluent cations such as methylsulphonic acid (MSA) pass through a membrane towards the anode to combine with hydronium ions whilst the hydroxide ions in the cation chamber pass into the eluent chamber to neutralize the eluent reducing conductivity.

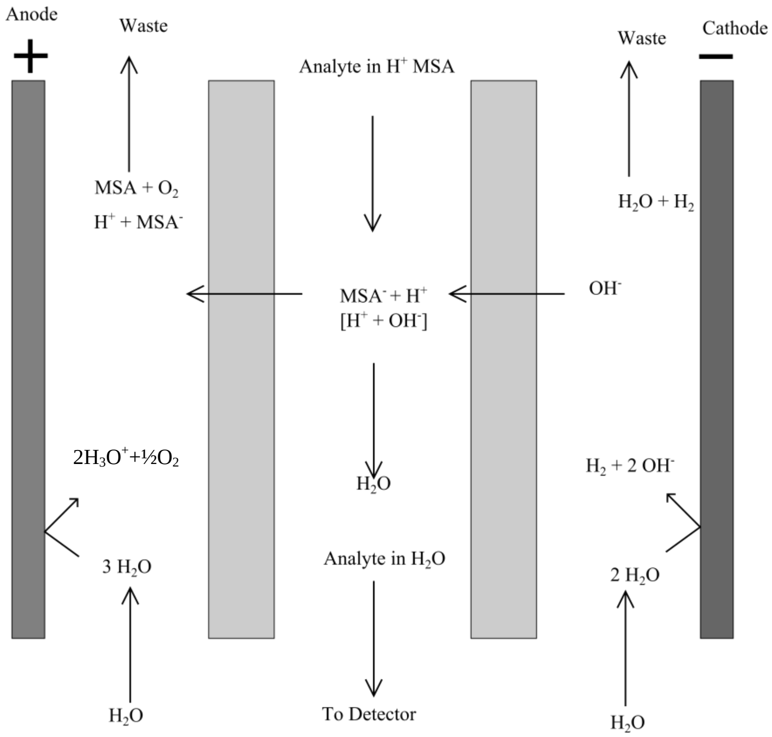

Figure 2. 9 - Schematic of conductance cell

2.2-7 Radiotracer studies

^{85}Sr was used as a radiotracer in order to test ion exchange capacity within a highly dilute system. In order to examine the uptake, the activity of the ion exchange solution was measured before and after exchange. ^{85}Sr decays primarily via electron-capture, emitting a gamma-ray of 514.01 keV with $t½$=64.84 days.

When gamma rays interact with matter three events may occur, the probability being dependent upon the energy of the incident gamma-ray and material:

- Photoelectric effect;
- Compton scattering;
- Pair production.

The photoelectric effect as described previously in the XRF section occurs most likely with lower energy gamma-rays, however, it should be noted that in addition to the emission of an X-ray when an electron from a higher shell drops down, it is also possible for the emission of another low-energy electron, known as an Auger electron.

The Compton Effect occurs when the energy of the gamma-ray is high enough that it interacts with a valence orbital directly, rather than a core electron. In this case an electron is ejected from the atom to form an ion pair, and the gamma-ray is deflected at an angle with a lower energy:

$$E\gamma_2 = E\gamma_1 - I.P. - E_e$$

where

- $E\gamma_1$ and $E\gamma_2$ are the energies of the incident and deflected gamma-rays respectively
- I.P. is the ionization potential of the ejected electron and
- E_e is the kinetic energy of the ejected electron

Pair production occurs when the gamma ray interacts with the coulomb field of the nucleus converting into an electron and a positron. The positron encounters another electron resulting in annihilation and two orthogonal gamma rays, each of 0.51 MeV. As according to $E = mc^2$, the minimum energy necessary to form an electron is 0.51 MeV, this process only occurs with gamma-rays above 1.02 MeV.

In this work, solid state semiconductor hyperpure Ge or NaI crystal scintillation detectors were used to measure the activity. These detectors use a scintillation material to produce photons via the photoelectric effect, Figure 2.10, which are then detected by a photomultiplier tube, Figure 2.11. When the photons interact with the semiconductor and form positive holes, the charges are separated due to an applied electric field and a pulse of collected charge can be recorded.

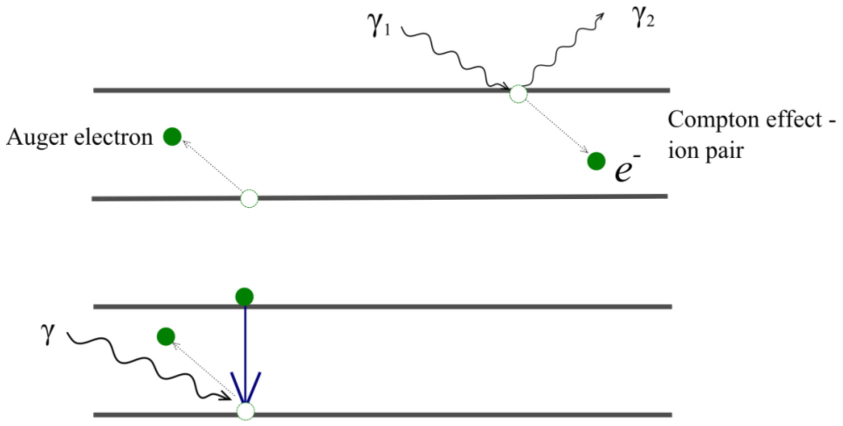

Figure 2. 10 - Example of photoelectric effect

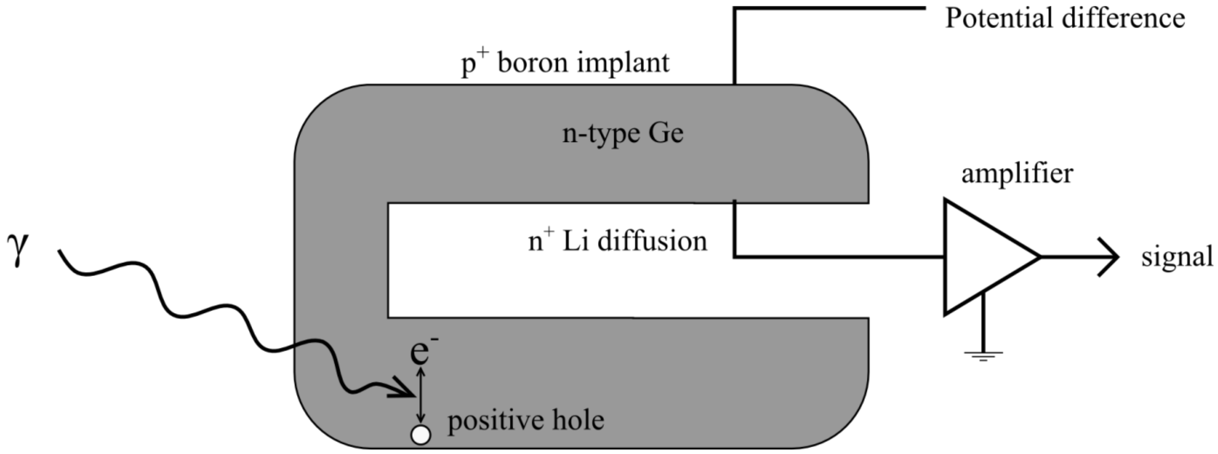

Figure 2. 11 - Schematic of Ge semiconductor photomultiplier detector

Chapter 3: Titanosilicates and Zirconosilicates

3.1 Introduction

Many titanosilicates and zirconosilicates have been well studied and demonstrate good ion exchange capacity[36,35,61]. This chapter will focus on some the work done to attempt to synthesise new materials based on existing mineral phases for ion exchange applications. Noonkanbahite, shown in Figure 3.1, is a natural mineral with the formula $BaKNaTi_2Si_4O_{14}$, a member of the bakovite group of minerals which also includes batisite, $BaNa_2Ti_2Si_4O_{14}$, and shcherbakovite, $(K,Ba)KNaTi_2Si_4O_{14}$[80]. These minerals contain 4 SiO_4 tetrahedral unbranched single-width chains within the unit cells which are connected by chains of TiO_6 octahedra. These materials appear to be interesting candidates for ion exchange due to the different cations in the structure. The divalent cations in the structure indicate a potential affinity for strontium cations; additionally different cation sites in the pores could potentially allow for uptake of both strontium and caesium without competition for the same site. The initial focus of this work was the synthesis of noonkanbahite or related natural minerals such as bakovite and shcherbakovite, which proved challenging. Whilst focus eventually shifted to other materials the synthesis of noonkanbahite remained a goal throughout the project.

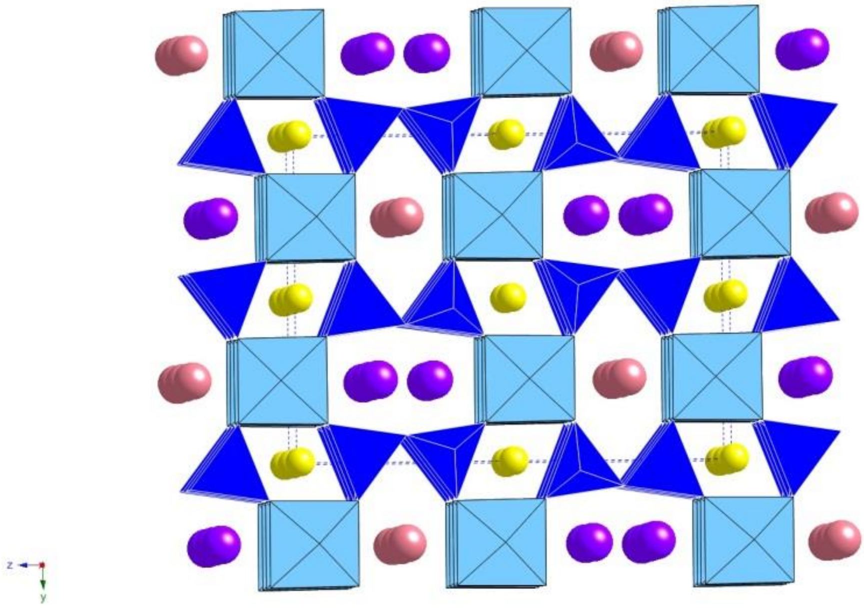

Figure 3. 1 - Noonkanbahite along (100) showing connectivity of the polyhedra chains, with TiO octahedra in cyan, SiO_4 tetrahedra in blue and sodium,, potassium and barium cations in yellow, purple and pink respectively

The synthesis of zirconium silicate materials has been well studied in particular the Na_2O-ZrO_2-SiO_2 system [36]. However the addition of fluoride which acts as a mineralizer to increase the rate of dissolution of starting materials which can lead to the formation of different phases has not been reported so this was briefly investigated to see the effects.

Strontium zirconosilicates occur in nature, e.g. aqualite. This would indicate that hydrothermal synthesis of a strontium zirconosilicate should be possible. A strontium zirconosilicate could potentially be ion exchanged to remove the strontium and obtain the sodium or proton form, allowing for uptake of strontium into a lattice suited for strontium remediation. This chapter contains brief investigations into the synthesis of these zirconosilicate materials followed by the structural changes induced by initial ion exchanges and subsequent heat treatment of AV-3, a synthetic equivalent of petarasite.

3.2 Experimental

3.2-1 Noonkanbahite & related phases

Attempts to prepare a synthetic form of the natural mineral noonkanbahite type titanosilicate using a sol-gel type method were attempted after a significant number of attempts using a standard hydrothermal route yielded a mixture of amorphous glassy materials and simple silicate materials. Titanium isopropoxide(TIP) and Ludox® colloidal silica were mixed in 10ml ethanol solutions as in the table below, before being added to an aqueous solution of the group I and group II metal salts. The gels were aged for 40 minutes before heating hydrothermally at 200°C for 5 days.

Table 3. 1 – Titanosilicate synthesis gel preparations

Ref	TIP (g)	LUDOX® HS-40 (g)	NaOH (g)	KOH (g)	KF (g)	$Ba(OAc)_2$ (g)	Molar ratio Ti:Si:Na:K:F:Ba
1	1.000	2.393	0.997	0	0.858	0	1: 4.5: 7.1 : 4.2: 4.2: 0
2	1.000	2.393	0	0.997	0	0	1: 4.5: 0 : 5.1: 0: 0
3	1.000	2.393	0.997	0	0	0.195	1: 4.5: 7.1 : 0: 0: 0.2
4	1.000	2.393	0.997	0	0.858	0.195	1: 4.5: 7.1 : 4.2: 4.2: 0.2

A switch was made from a sol gel type method to a simpler one with barium as the only extra-framework cation. The mixing of reagents was improved by using anhydrous titanium isopropoxide and tetraethylortho silicate (TEOS), in the amounts tabulated below, in 10ml ethanol to avoid premature hydrolysis. After thorough mixing of the solution, the barium hydroxide solution was added to allow the hydrolysis before aging for 40 minutes and heating the gels hydrothermally at 200°C for 5 days.

Table 3. 2 - Titanosilicate synthesis gel attempts

Ref	TIP (g)	TEOS (g)	$Ba(OH)_2 \cdot 8H_2O$ (g)	H_2O (g)	Molar ratio Ti:Si:Ba:H_2O
SG_1	1.000	1.066	0.700	18.504	1: 1.5: 0.6: 298
SG_2	1.000	1.218	0.800	21.147	1: 1.7: 0.7: 340
SG_3	1.000	1.421	0.933	24.671	1: 1.9: 0.8: 398
SG_4	1.000	1.705	1.120	29.606	1: 2.3: 1: 478
SG_5	1.000	2.132	1.399	37.008	1: 2.9: 1.3: 584

Returning to previously reported starting reagents of $TiCl_4$ [81] and colloidal silica, a number of gels were prepared by dissolving KOH, KF and NaOH in water according to the masses in Table 3.3, followed by adding 1.0g $TiCl_4$ in liquid form and Ludox® HS-40 collodial silica. After homogenizing for 30 minutes the gel was heated the gels hydrothermally at 200°C for 5 days.

Attempts were also made to prepare synthetic shcherbakovite which is related to noonkanbahite but contains no barium. In this case the Si/Ti ratio was kept constant except in the case of sample H, in an effort to prepare the desired phase as shown in Table 3.3.

Table 3. 3 - Scherbakovite synthesis attempt gels

Ref	$TiCl_4$ (g)	Ludox (g)	NaOH (g)	KOH (g)	KF (g)	Molar ratio Ti:Si:Na:K:F
A	1.000	1.335	5.003	3.472	0.654	1: 1.7: 23.7: 13.9: 2.1
B	1.000	1.335	2.497	1.733	0.654	1: 1.7: 11.8: 8: 2.1
C	1.000	1.335	5.003	2.315	0	1: 1.7: 23.7: 7.8: 0
D	1.000	1.335	2.497	1.733	0	1: 1.7: 11.8: 5.9: 0
E	1.000	1.335	5.003	3.472	0	1: 1.7: 23.7: 11.7: 0
F	1.000	1.335	3.361	2.315	0	1: 1.7: 15.9: 7.8: 0
G	1.000	1.322	0	6.945	0	1: 1.7: 15.4: 23.5: 0
H	1.000	2.670	5.003	3.472	0	1: 3.4: 23.7: 11.7: 0

Attempts to prepare a calcium titanosilicate involved dissolving $Ca(OH)_2$ in H_2O as in Table 3.4 followed by addition of titanium isoproxide and Ludox® HS-40 collodial silica allowing the mixture to gel. The gel was allowed to homogenize for 30 minutes before heating hydrothermally at 230°C for 5 days.

3.2-2 Titanite synthesis gels

Table 3. 4 - Titanite synthesis gels

Ref	TIP (g)	Ludox® (g)	$Ca(OH)_2$ (g)	H_2O (g)	Molar Ratio Ti:Si:Ca:H_2O
$CaTi_xSi_yO_z$ A	0.570	2.567	1.000	28.558	0.15: 1.27: 1: 124
$CaTi_xSi_yO_z$ B	1.061	2.572	1.000	19.039	0.28: 1.27: 1: 85
$CaTi_xSi_yO_z$ C	0.820	0.856	1.000	19.039	0.21: 0.42: 1: 80
$CaTi_xSi_yO_z$ D	0.950	1.711	1.000	19.039	0.25: 0.85: 1: 83

3.2-3 Zirconosilicate synthesis gels

In order to attempt the preparation of a strontium zirconosilicate, a series of gels was prepared according to Table 3.5, where $ZrCl_4$ powder and $Sr(OH)_2{\cdot}8H_2O$ were dissolved in H_2O before adding Ludox® HS-40 colloidal silica. Thick white gels were formed which were allowed to homogenize by stirring for 40 minutes before heating hydrothermally at 230°C for 5 days.

Table 3. 5 - Sr-Zr-Silicate synthesis attempts gel

Ref	$ZrCl_4$ (g)	LUDOX (g)	$Sr(OH)_2 \cdot 8H_2O$ (g)	H_2O (g)	Molar Ratio Zr:Si:Sr:H_2O
SrZrSiO2_1	1.000	1.000	0.548	37.020	1: 2.3: 0.5: 488
SrZrSiO2_2	1.000	1.000	1.245	37.020	1: 2.3: 1.1: 495
SrZrSiO2_3	1.000	1.000	2.191	37.020	1: 2.3: 1.9: 497
SrZrSiO2_4	1.000	1.000	2.448	37.020	1: 2.3: 2.1: 509
SrZrSiO2_5	1.000	1.000	4.191	37.020	1: 2.3: 3.7: 480

A final series of gels were prepared in an effort to investigate what effect, if any, fluoride would have on the synthesis of sodium zirconosilicates. Gels were prepared according to Table 3.6 where $ZrCl_4$ and NaF powders along with NaOH pellets were dissolved in 20 cm^3 H_2O before adding Ludox® HS-40 collodial silica. Thick white gels were formed which were allowed to homogenize by stirring for 40 minutes before heating hydrothermally at 230°C for 5 days.

Table 3. 6 - Na-Zr-SiO_2 -F synthesis gel preperations

Ref	$ZrCl_4$ (g)	LUDOX (g)	NaOH (g)	NaF (g)	Molar Ratio Zr:SiO_2:Na:F
Zr_Si_NaF A	1.000	1.00	2.50240	1.111	1: 1.55: 14.7: 6.2
Zr_Si_NaF B	1.000	3.00	2.50240	1.111	1: 4.66: 14.7: 6.2
Zr_Si_NaF C	1.000	9.00	2.50240	1.111	1: 13.98: 14.7: 6.2

AV-3 was prepared as per literature[82] by dissolving 1.43g NaOH pellets, 2g NaCl, 1g KCl and 0.84g $ZrCl_4$ powder in 7.21 cm^3 deionized water. To this was added 5.35 g sodium silicate solution (23% m/m SiO_2, 8% m/m Na_2O). The gel was then allowed to homogenize before heating under autogenous pressure for 10 days at 230°C.

3.2-4 Ion exchanges

1.00g of ground AV-3 was added to 25cm^3 of $Sr(NO_3)_2$ solutions of concentrations 0.001 mol^{-1} dm^3, 0.05 mol^{-1} dm^3, 0.5 mol^{-1} dm^3 or 1.0 mol^{-1} dm^3, before shaking for 24 hours. The resultant suspension was filtered, washed well with deionized water and the solids formed into fused beads for XRF analysis.

3.3 Results and discussion

3.2-1 Noonkanbahite and related phases

Preparing precursor gels as an aqueous mixture using colloidal silica and water-soluble metal salts did not produce a material with a Ti-O-Si framework , only TiO_2 and SiO_2 phases as seen in Figure 3.2. This may be due to the rapid gelling of the silica as it hydrolyses rapidly in a basic environment. A very thick gel was produced; where the TIP did not appear to mix properly forming an inhomogeneous emulsion rather than the homogeneous colloidal sol as in a typical sol-gel process.

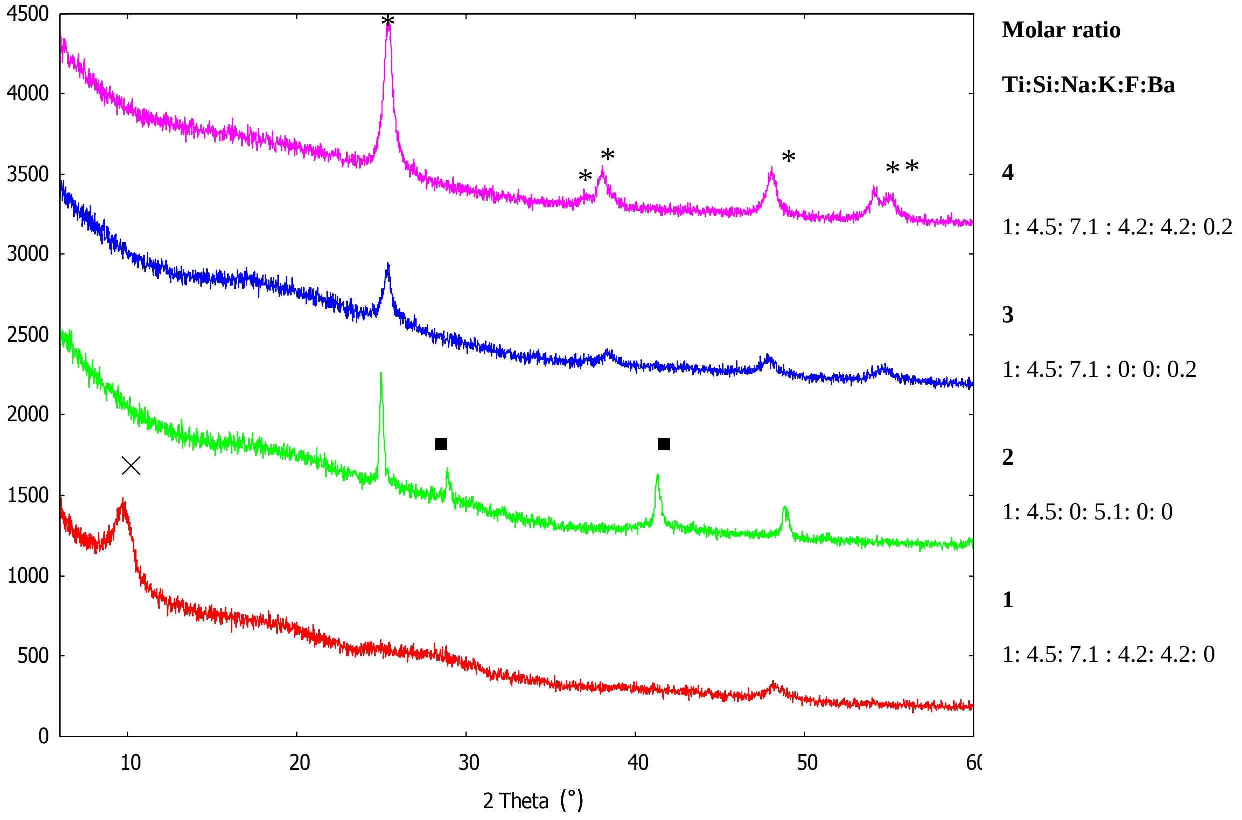

Figure 3. 2 – XRD patterns of the first synthesis attempt of a new titanosilicate
*** - TiO_2 Anatase – PD F 01-086-1157**

■ - TiO_2 – PDF 04-001-1352

× - SiO_2 - PDF 01-089-1667

The sol-gel type method did not yield any interesting phases either, as seen in Figure 3.3, the phases are predominately amorphous material with a small amount of crystalline TiO_2. There is a small trace of a crystalline phase, however due to very low intensity peaks and poor signal to noise ratio this assignment is somewhat dubious.

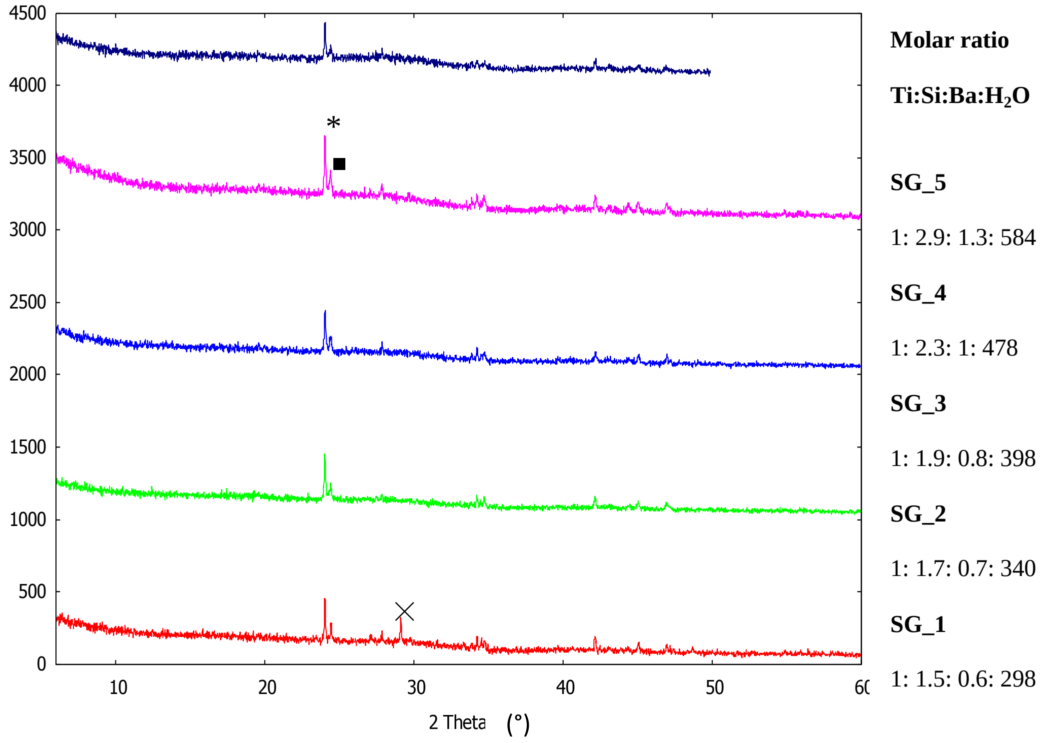

Figure 3. 3 - XRD patterns of sol-gel attempts at noonkanbah

*** - $Ba_2Si_3O_8$ – PDF 04-011-1317**

■ - TiO_2 – PDF 01-070-2556

× - $BaTiSiO_5$ – PDF 00-011-0150

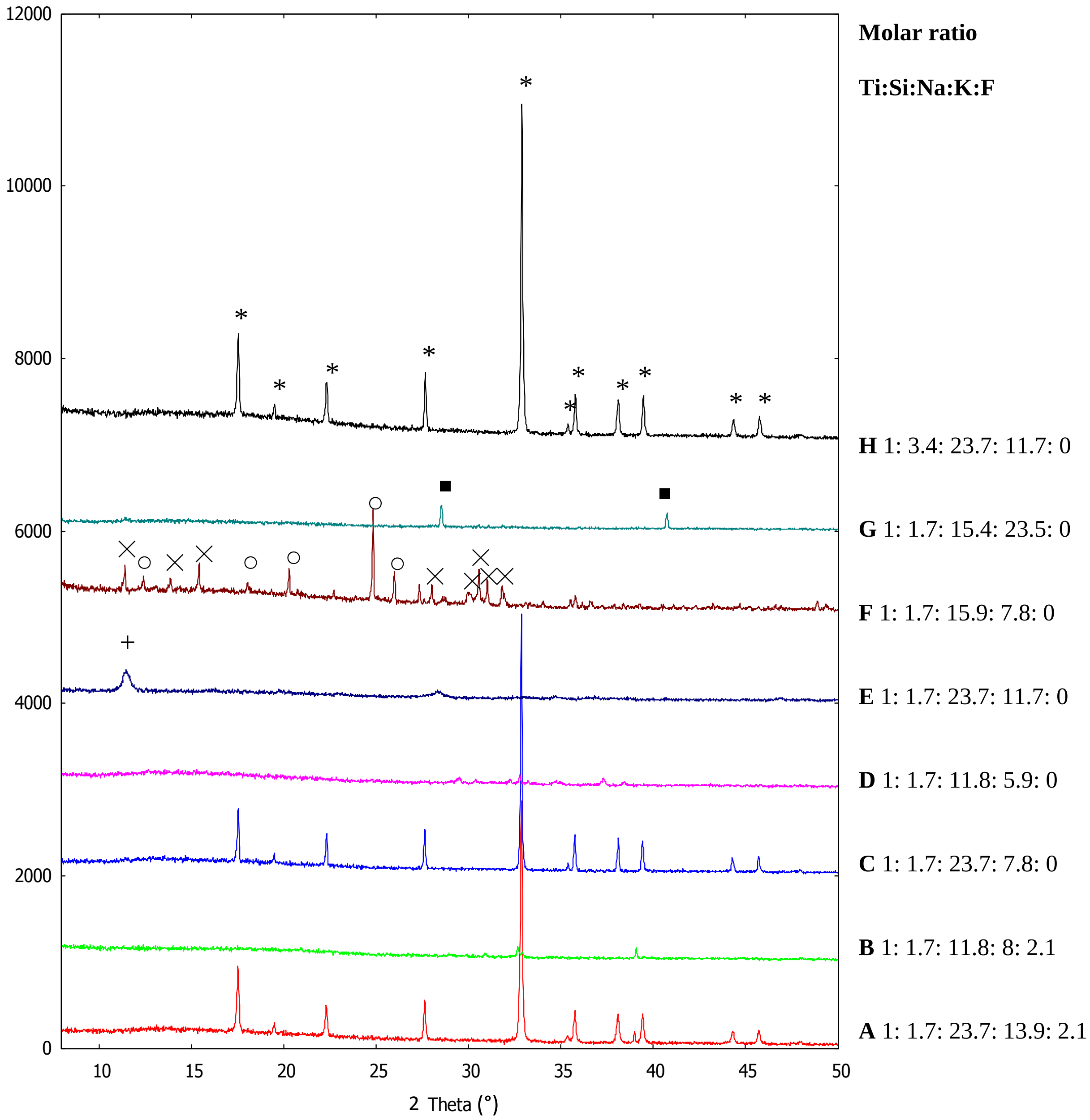

Figure 3. 4 - XRD patterns of scherbakovite attempts

*** - $Na_2Ti(SiO_4)O$ Natisite PDF – 04-011-0023**
■ – KCl PDF - 04–002–3657

× - $K_2TiSi_3O_9(H_2O)$ Umbite PDF – 04-012-4486

○ - $Na_2TiSi_5O_{13}$ ETS-10 PDF -04-013-2831
+ - SiO_2 - PDF 01-089-1667

Figure 3.4 shows natisite was the major crystalline phase observed in this series identified in samples A,C & H. However natisite has been shown to be a poor ion exchanger[83] unless modified due to sodium cations being trapped between layers of TiO. However, more recently some work has been undertaken by Readman *et al.* where doping Zr in to the natisite structure was shown to improve Cs uptake slightly [84]. Sample F shows of umbite along with ETS-10, both known and well-studied titanosilicate materials.

3.2-2 Titanite

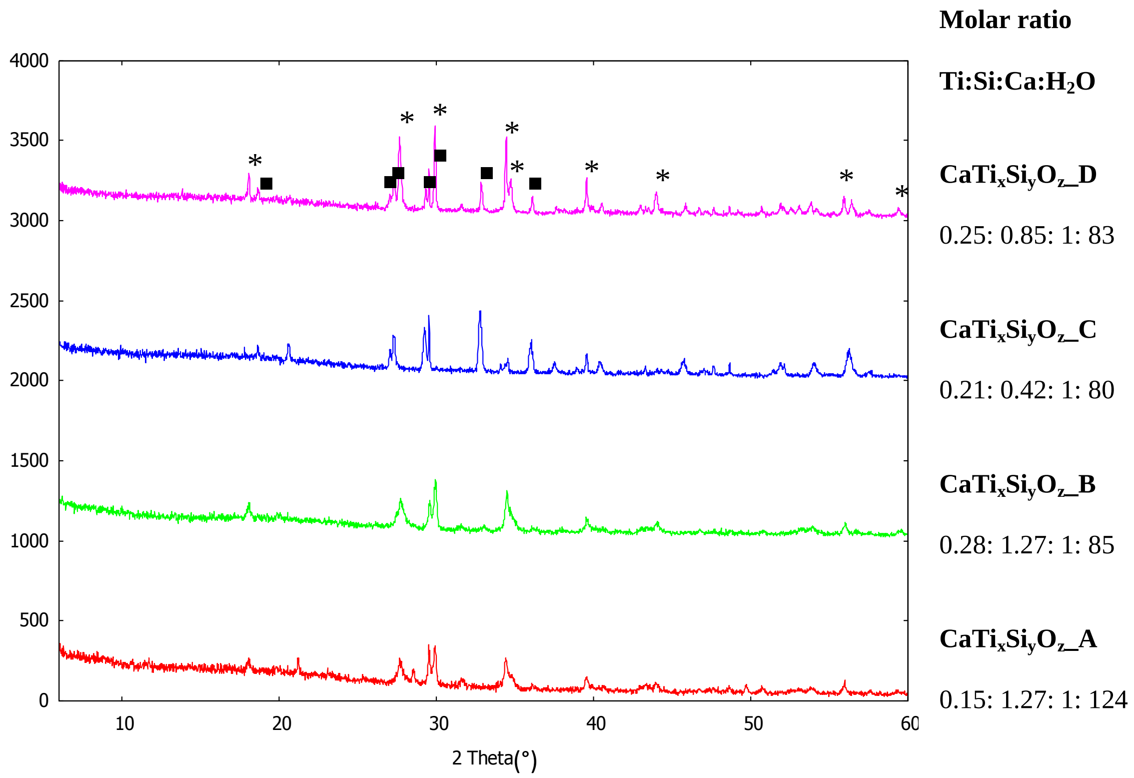

Figure 3. 5 - XRD patterns of CaOH - TiO_2-SiO_2 system syntheses

*** - CaTi(SiO_4)O Titanite – PDF 04-013-2626**
■ - Ca ($Ti_2O_4(OH)_2$) Kassite – PDF 01-072-6913

In addition to a lack of work reported on the subject on calcium titanosilicates, ^{90}Sr is known to replace calcium in bone tissue[85] so in order to obtain a material which could potentially selectively uptake strontium , a material with exchangeable extra-framework calcium cations was a synthesis target. Initial synthesis attempts, shown in Figure 3.5, through hydrothermal, sol-gel and solid state methods yielded mostly amorphous end phases. Only hydrothermal synthesis with titanium as the framework metal resulted in any crystalline products, of these mixed phase systems the titanite phase was observed via a pattern search and match against the PDF database. Titanite was later prepared again as a pure poorly crystalline phase via a hydrothermal synthesis route. Rietveld refinement of this phase, from data acquired on a Bruker D8 in reflection geometry using a structure from the PDF database[86] as a starting model, Figures 3.6 & Table 3.7, yielded a structure shown in Figure 3.7 with selected bond distances and angles shown in Table 3.8.

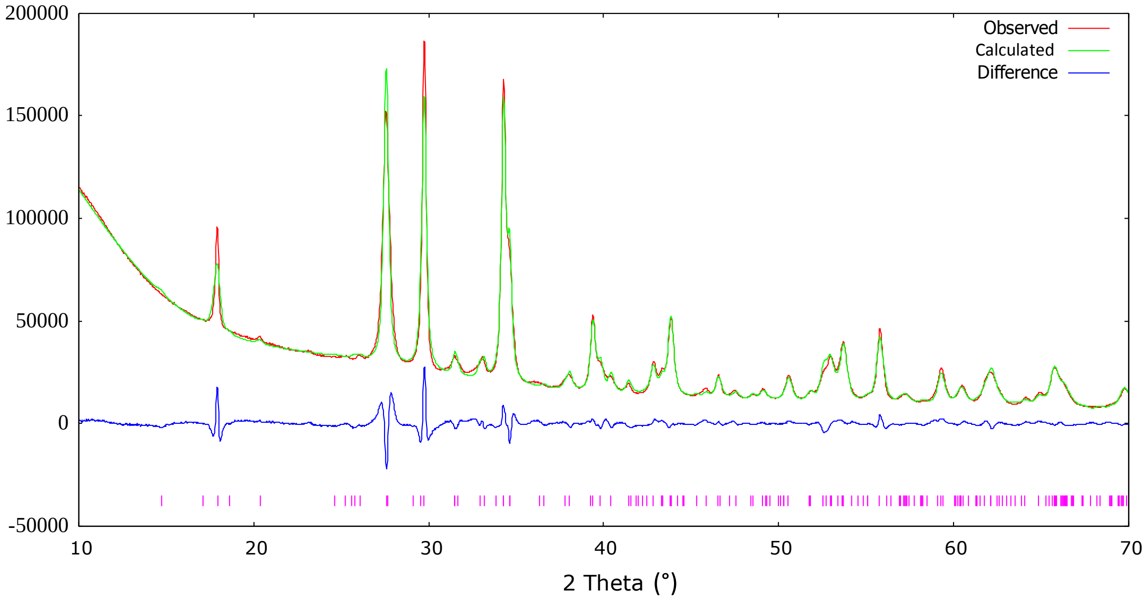

Figure 3. 6 - Rietveld refinement of Ca-titanite using TOPAS Academic 4.3

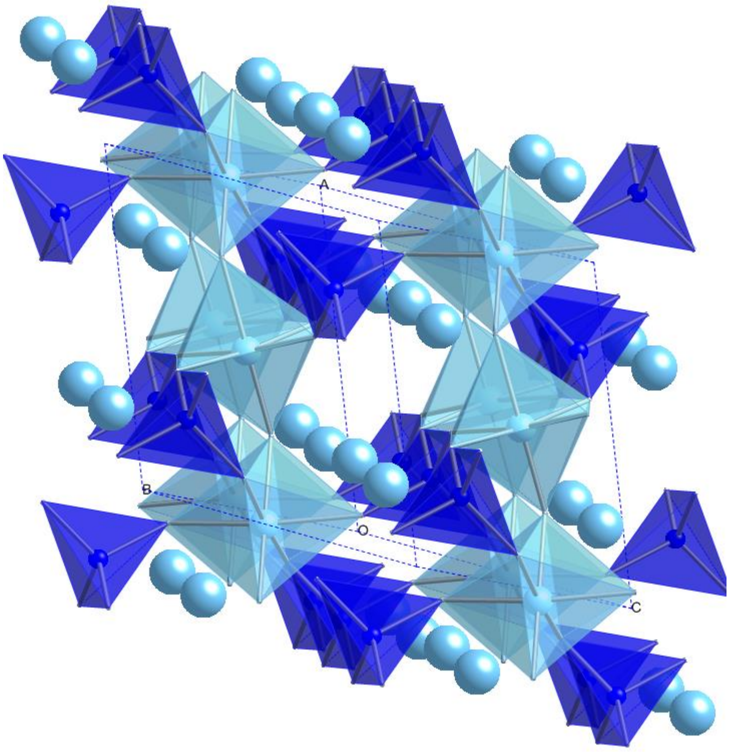

Figure 3. 7 - Refined structure of Ca-titanite with blue SiO_4 tetrahedra, cyan TiO_6 octahedra and Ca spheres.

Table 3. 7 - Rietveld refinement parameters of Ca-titanite occupancies and displacement parameters (B_{eq}) were both fixed at 1 Å^2.

a /Å	7.0337(4)	**X-ray source**	Cu Kα1 and Kα2
b /Å	8.7125(6)	**Scan time**	8 hours
c /Å	6.5534(5)	**Step size**	0.02°
V /Å^3	367.78(7)	**Background**	Chebyshev
β /°	113.74(7)	**Peak shape profile**	Tompson-Cox Hastings
space group	P2$_1$/a		
Z	4		
Nº independent parameters	50		
R_{wp}	4.781		
R_{exp}	0.487		
R_p	2.863		

Site	**x**	**y**	**z**
Ca1	0.217(1)	0.4175(5)	0.251(2)
Ti1	0.501(2)	0.2499(9)	0.743(2)
Si1	0.749(3)	0.4354(8)	0.253(4)
O1	0.716(4)	0.305(1)	0.753(4)
O2	0.920(4)	0.326(3)	0.450(5)
O3	0.087(4)	0.183(3)	0.074(5)
O4	0.396(4)	0.472(3)	0.668(4)
O5	0.593(3)	0.031(3)	0.851(5)

Table 3. 8 - Bond distances and angles from Ca-titanite Rietveld refinement

Bond	Distance (Å)	Bond	Angle °	Bond	Angle °
Ca1-O1	2.46(2)	**O1-Ti-O1**	173.3(2)	**O1-Ca-O2**	137.4(2)
Ca1-O2	3.05(1)	**O1-Ti-O2**	89.6(1)	**O1-Ca-O3**	152.1(1)
Ca1-O2	2.40(1)	**O1-Ti-O3**	84.8(2)	**O1-Ca-O4**	58.2(1)
Ca1-O3	2.50(1)	**O1-Ti-O4**	85.6(2)	**O1-Ca-O4'**	78.1(2)
Ca1-O4	2.54(1)	**O1-Ti-O5**	88.6(1)	**O1-Ca-O5**	80.6(1)
Ca1-O4	2.75(1)	**O2-Ti-O3**	172.6(3)	**O1-Ca-O5'**	74.7(2)
Ca1-O5	2.41(2)	**O2-Ti-O4**	94.96(9)	**O2-Ca-O3**	64.9(2)
Ca1-O5	2.33(2)	**O2-Ti-O5**	94.7(1)	**O2-Ca-O4**	84.0(1)
Ca1-Si1	3.06(2)			**O2-Ca-O4'**	74.2(1)
		O2-Si-O3	105.5(2)	**O2-Ca-O5**	122.7(1)
Ti1-O1	2.166(9)	**O2-Si-O4**	116.6(2)	**O2-Ca-O5'**	143.2(2)
Ti1-O2	1.93(1)	**O2-Si-O5**	114.5(1)	**O3-Ca-O4**	124.5(1)
Ti1-O3	2.06(1)	**O3-Si-O4**	91.6(2)	**O3-Ca-O4'**	129.7(1)
Ti1-O4	2.12(1)	**O3-Si-O5**	110.5(1)	**O3-Ca-O5**	71.7(2)
Ti1-O5	1.996(9)	**O4-Si-O5**	115.0(1)	**O3-Ca-O5'**	93.0(1)
				O4-Ca-O4'	76.4(1)
Si1-O2	1.56(1)			**O4-Ca-O5**	91.6(2)
Si1-O3	1.74(1)			**O4-Ca-O5'**	132.0(1)
Si1-O4	1.55(2)			**O5-Ca-O5'**	71.2(2)
Si1-O5	1.75(1)				
Si1-Ca1	3.06(1)				

The refined cell and average Ca-O, Ti-O and Si-O bond distances all agree with those reported in the literature[86,87] which are predominantly data derived from single crystal diffraction experiments on natural titanite samples. The agreement of atom positions between literature and the refined data is acceptable, although there is some displacement of the cations, considering the poor quality of the sample as indicated by the wide peaks shown in Figure 3.6, which prevented a good fit from being obtained.

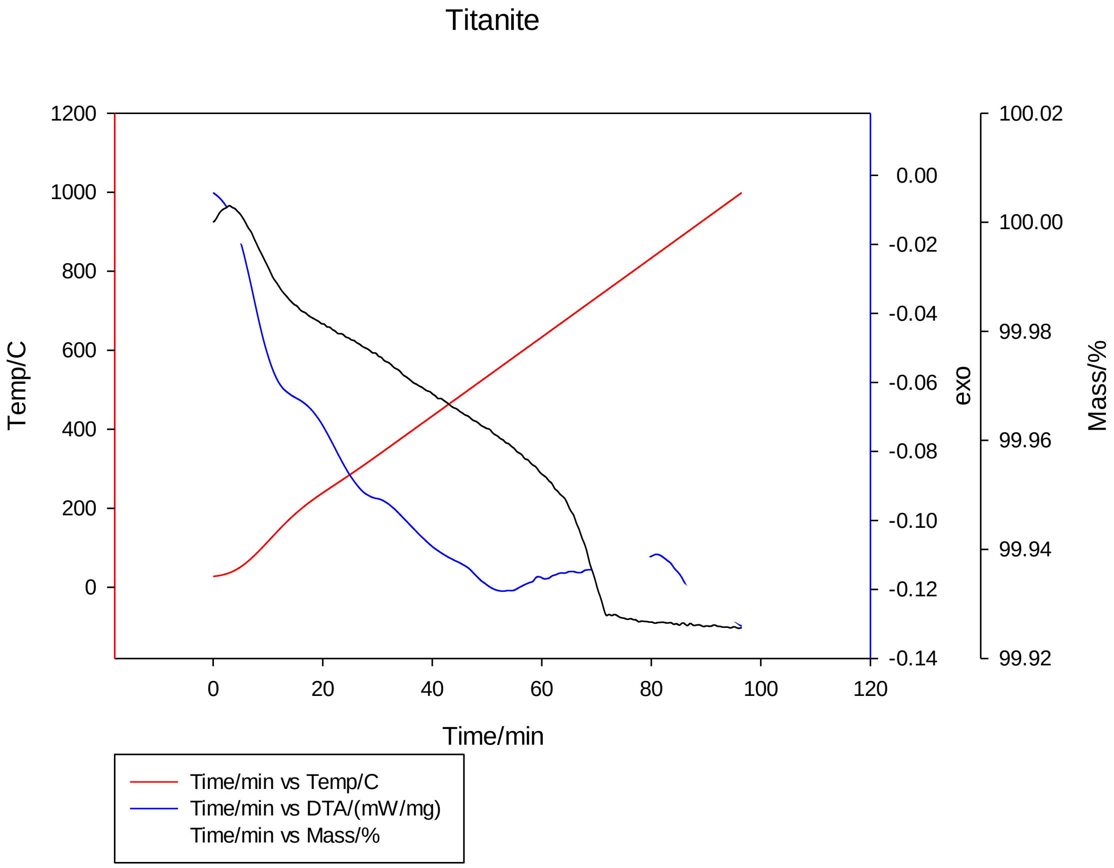

Figure 3. 8 TGA trace of Ca-titanite between 30 and 1000 °C under N_2

Titanite shows good thermal stability; powder XRD of a sample heated in a furnace to 1000°C indicates no notable change to the structure and TGA shows little change in mass loss or the DTA trace. A drop of 0.04% at approx. 700°C is the most significant event which could be due to the loss of some small amount of volatile impurity present. A small change is evident between 200 and 300°C which coincides with a structural change from $P2_1/a$ to $A2/a$ as described by Taylor and Brown[87].

Unfortunately titanite did not show any significant strontium ion exchange behaviour from initial ion exchange experiments analysed by XRF and preliminary ^{85}Sr ion exchange work, as described in Chapter 5 section 3.4.

3.3-3 Fresnoite

Attempts to produce a new barium titanite phase yielded primarily amorphous products and mixtures of simple condensed materials; the only product of note was a synthetic analogue to the natural mineral fresnoite ($Ba_2TiSi_2O_8$) with a small amount of an unknown impurity. Fresnoite is a porous layered titanosilicate containing titanium in an unusual 5 coordinate square pyramidal geometry. Unfortunately, as in the case of titanite, no ion exchange behaviour was observed during preliminary ion exchange experiments studied using XRF. A Rietveld refinement, Figures 3.9 & 3.10, Table 3.9 & 3.10, was obtained from data acquired using a Bruker D8 diffractometer in reflection mode using a structure from the PDF database as a starting point[88]. Fresnoite shares some structural characteristics with natisite (Na_2TiSiO_5) such as the square pyramidal TiO_5 units and both materials being layered structures. In this case it may not be surprising that fresnoite does not exchange well as the cations are locked in place by the layered structure.

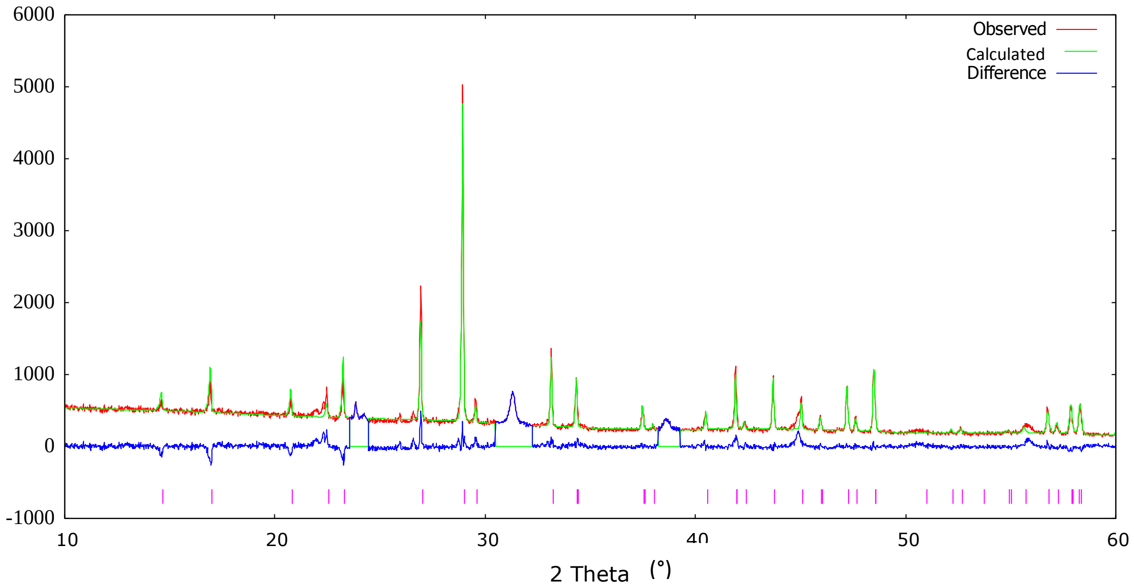

Figure 3. 9 - Rietveld refinement of fresnoite phase with excluded areas

Table 3. 9 - Rietveld refinement parameters and atom positions for Fresnoite refinement where occupancies and displacement parameters (B_{eq}) were fixed at 1 Å^2

a /Å	8.5188(2)	**X-rays**	Cu Kα1 and Kα2
c /Å	5.2067(2)	**Scan time**	3 hours
V /Å^3	377.85(3)	**Step size**	0.02°
space group	*P*4*bm*	**Background**	Chebyshev
		Peak shape profile	Thompson-Cox Hastings
Z	8		
Nº independent parameters	21		
R_{wp}	9.777		
R_{exp}	5.086		
R_{p}	6.877		
excluded region 1	30.5-32.2		
excluded region 2	23.6-24.4		
excluded region 3	38.25-39.24		

Site	***x***	***y***	***z***
Ti1	0	0	0.444(7)
Ba1	0.329(9)	0.828(8)	0
Si1	0.127(3)	0.626(8)	0.483(1)
O1	0.371(6)	0.549(5)	0.578(2)
O2	0.135(5)	0.635(2)	0.288(8)
O3	0	0.5	0.659(2)
O4	0	0	0.445(2)

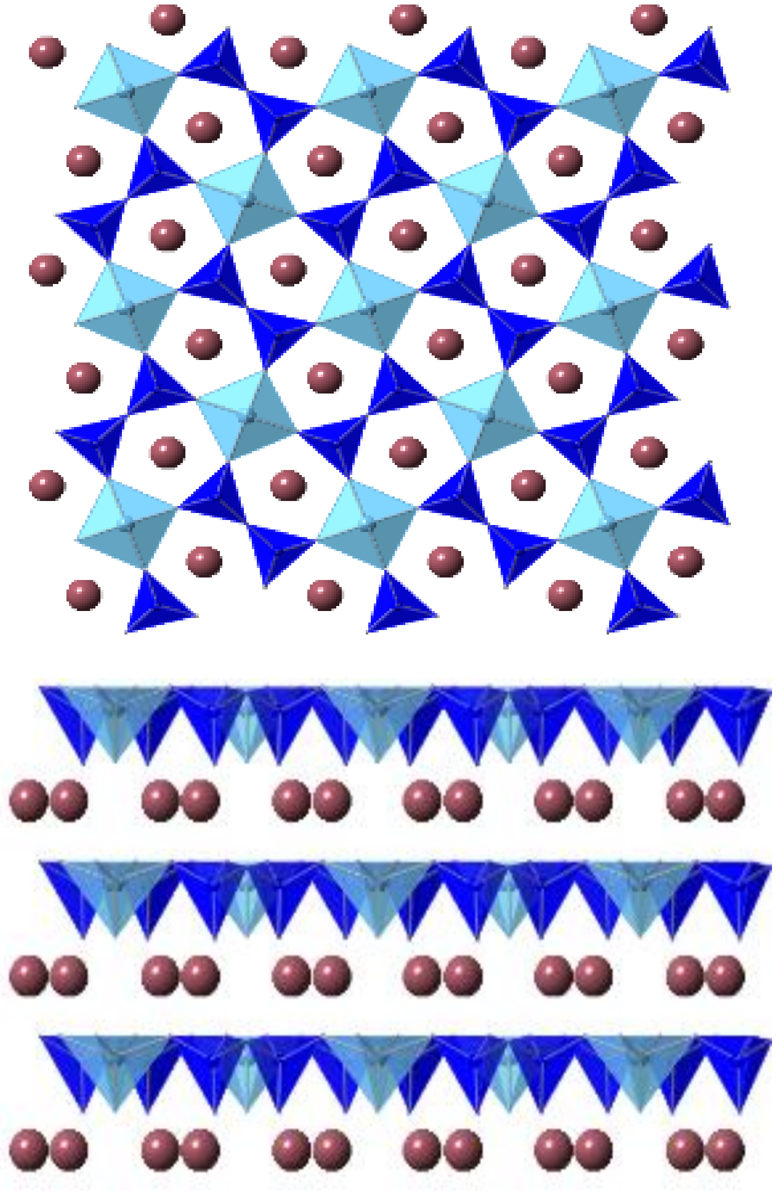

Figure 3. 10 - Refined structure of fresnoite viewed along (001) above and (010) below with TiO_5 in cyan, SiO_4 in blue and barium cations in brown

Table 3. 10 - Selected refined bond distances and angles of fresnoite

Bond	Distance (Å)	Bond	Angle 1 (deg)	Angle 2 (deg)	Angle 3 (deg)
Ti1 - O4	1.70(9)	**O1-Ti-O4**	106.2(2)		
Ti1 - O1	1.98(6)	**O1-Ti1-O1**	85.6(7)	148.0(8)	
Ba1 - O2	2.77(4)	**O1-Si1-O1**	104.3(5)		
Ba1 - O1	2.82(5)	**O1-Si1-O2**	117.0(4)		
Ba1 - O3	2.83(4)	**O1-Si1-O3**	103.8(4)		
Si1 - O2	1.59(7)	**O1-Ba1-O1**	55.0(4)	96.6(5)	
Si1 - O3	1.62(7)	**O1-Ba1-O2**	71.9(5)	118.3(3)	163.8(4)
Si1 - O1	1.62(6)	**O1-Ba1-O3**	52.2(3)	91.0(5)	
Si1 - Si1	3.02(4)	**O2-Ba1-O3**	74.1(5)	160.8(6)	

Despite the sample being impure, the fit can be compared acceptably in terms of unit cell and average bond distances to the literature[88] where single crystal data was collected, however, the R-factors in the overall fit are high as are the errors in the atomic positions. Whilst the atomic positions are reasonably close, with the exception of the titanium atom, which is displaced by approximately 0.5 Å along the *z* direction, the model generated is only reliable in terms of backing up the assignment of the main phase produced as fresnoite rather than as a definitive crystal structure.

3.3-4 Zirconosilicate synthesis

Whilst much work has been done on the synthetic phases of the NaOH–ZrO_2–SiO_2 system, the introduction of fluoride to act as a mineralizing agent may alter which phases crystallize and if a novel phase was possible. Furthermore, the use of $ZrCl_4$ instead of ZrO_2 may also result in a difference in the observed phases for a given composition. Figure 3.11 shows the formation of various Zr:Si ratios with the addition of fluoride. In the case of all of these syntheses NaF is present in large amounts; the formation of a simple salt such as this would likely occur rapidly. The phases produced, $Na_2ZrSi_2O_7 \cdot H_2O$ and $Na_2ZrSi_3O_9 \cdot 3H_2O$ were not novel and have been studied for ion exchange previously in literature[45,47] so no further steps to obtain a pure phase were taken.

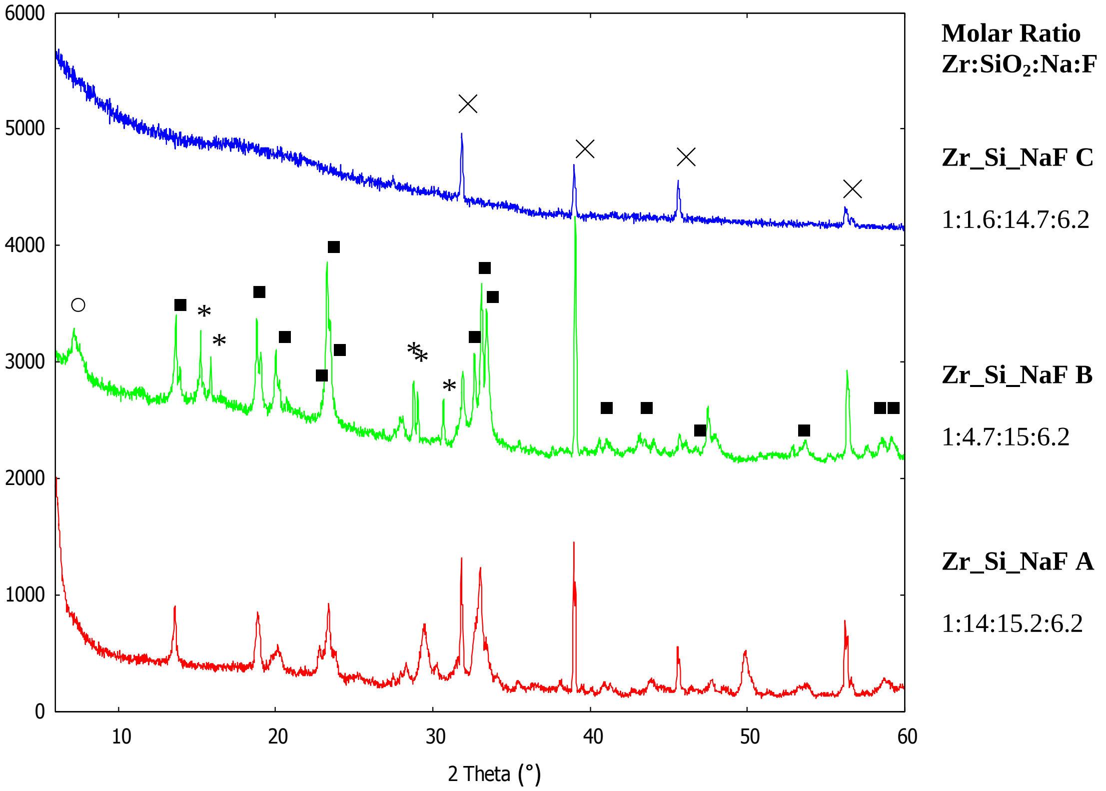

Figure 3. 11 - XRD patterns of the ZrO_2-SiO_2-NaOH-NaF system

× - NaF – PDF 00-004-0793

○ - SiO_2 – PDF 01-075-3900

■ - $Na_2ZrSi_2O_7 \cdot H_2O$ – PDF 04-017-2269

*** - $Na_2ZrSi_3O_9 \cdot 3H_2O$ (Gaidonnayite) PDF 04-012-8668**

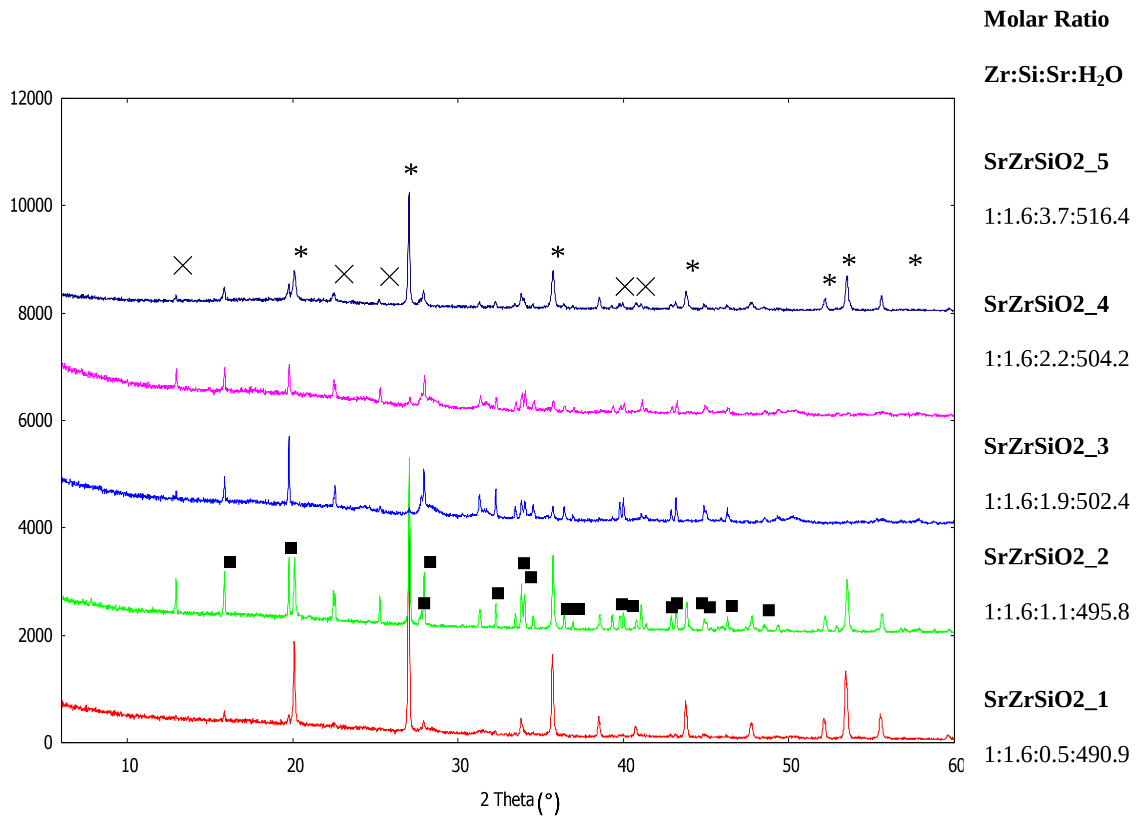

Figure 3. 12 - XRD patterns of synthesis attempts at Sr-zirconosilicate

× - $SrCl_2{\cdot}6H_2O$ PDF 04-010-2886

■ - $SrCl_2{\cdot}2H_2O$ PDF 00-025-0891

*** - $ZrSiO_4$ (Zircon) PDF 01-076-0865**

An attempt was made to prepare a strontium zirconosilicate, a strontium-containing metal silicate that could potentially then be acid-exchanged under highly forcing conditions to remove the strontium leaving a potentially strontium specific material. However, under these conditions the formation of zircon was too favourable to produce any other phases with the strontium forming hydrated chloride salts, including $SrCl_2{\cdot}6H_2O$ which should be too soluble to collect. The observation of the hexahydrate salt may be due to the hydrothermal bombs leaking water vapour which resulted in a supersaturated gel, allowing the salt to crystallize. The formation of only zircon and not a strontium zircon silicate could possibly be due to the $Sr(OH)_2{\cdot}8H_2O$ not being as strong a base or as soluble as the typical NaOH/KOH for these types of syntheses. Adding another base such as tetrabutylammonium hydroxide was thought to be able to lower the pH of the starting gel to disfavour the formation of zircon however hydrothermal heating of these gels resulted in amorphous materials. Whilst it may have been possible to investigate further the possibility of creating this strontium phase, a thorough investigation was deemed to be too time and equipment intensive and a broad approach was taken to synthesis attempts.

3.3-4a- Synthesis and characterisation of synthetic petarasite (AV-3)

AV-3 is a synthetic analogue to the natural zirconosilicate petarasite with the formula $Na_5Zr_2Si_6O_{18}(OH, Cl) \cdot 2H_2O$. AV-3 was reproduced using hydrothermal methods according to work by Lin *et al.*[66] and the structure refined against data acquired from a Bruker D8 X-ray diffractometer in reflection geometry (Figure 3.13& 3.14 and Tables 3.11-3.13). The initial model used for the refinement was from the PDF database[82].

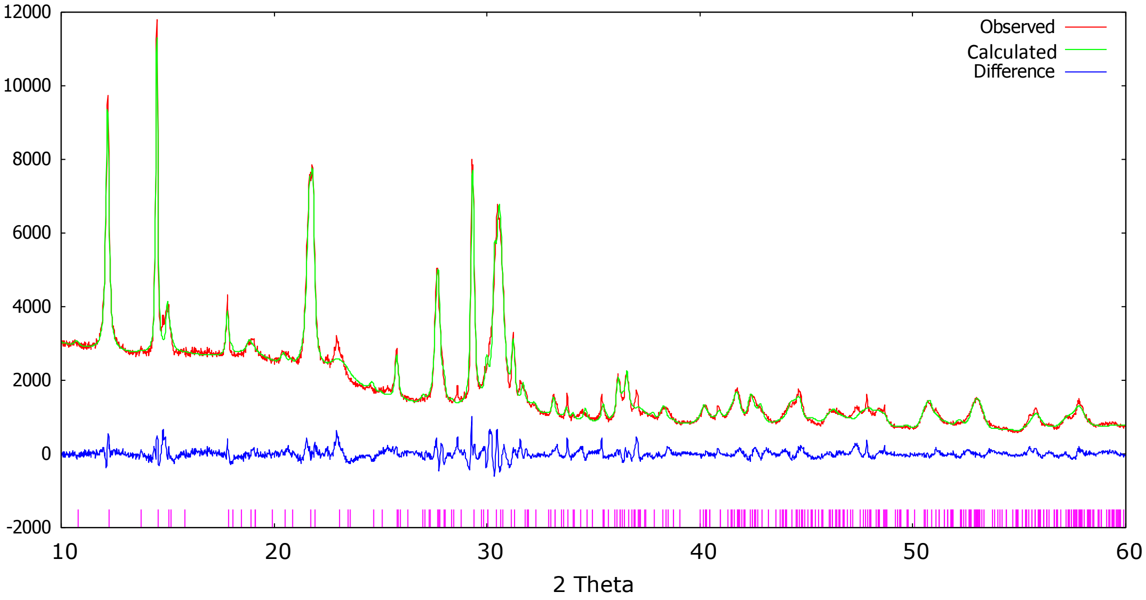

Figure 3. 13 - Rietveld refinement of as made petarasite (AV-3) using TOPAS academic V4.1

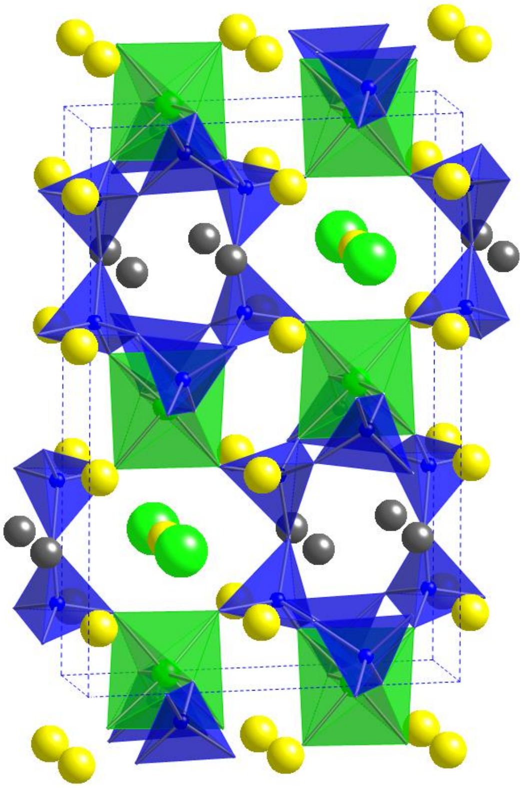

Figure 3. 14 - Refined structure of a petarasite (AV-3) along (001) Blue tetrahedra show SiO4 units and green octahedra ZrO_6 units. Yellow spheres indicate Na+ cations, green Cl- anions and grey water molecules

Table 3. 11 - Rietveld refinement parameters of petarasite (AV-3) displacement parameters (B_{eq}) were fixed at 1 Å^2

***a* / Å**	10.785(9)	**X-ray**	Cu Kα1 and Kα2
***b* / Å**	14.42(2)	**Scan time**	8 hours
***c* / Å**	6.708(5)	**Step size**	0.02°
***V* / Å^3**	944.3(2)	**Background**	Chebyshev
		Peak shape	Thompson-Cox
***β* / °**	113.24(6)	**profile**	Hastings
space group	$P2_1/m$		
Z	4		
NO. independent parameters	107		
R_{wp}	5.609		
R_{exp}	2.441		
R_p	3.975		

Site	***x***	***y***	***z***	***occ***
Na1	0.506(3)	0.087(2)	0.883(5)	0.96(4)
Na2	0.944(2)	0.130(2)	0.018(4)	0.88(4)
Na3	0.794(3)	0.25	0.483(7)	1.06(4)
Zr	0.7532(7)	0.009(5)	0.511(2)	1
Si1	0.032(2)	0.141(2)	0.577(4)	1
Si2	0.290(2)	0.046(2)	0.993(4)	1
Si3	0.448(2)	0.151(2)	0.368(3)	1
O1	0.062(5)	0.25	0.562(1)	1
O2	0.920(3)	0.114(2)	0.586(8)	1
O3	0.102(4)	0.068(3)	0.467(8)	1
O4	0.134(4)	0.100(2)	0.881(9)	1
O5	0.762(3)	0.027(3)	0.882(7)	1
O6	0.695(3)	0.038(3)	0.233(6)	1
O7	0.755(4)	0.120(3)	0.122(9)	1
O8	0.640(3)	0.123(3)	0.430(6)	1
O9	0.438(4)	0.25	0.482(9)	1
O10	0.422(3)	0.084(2)	0.517(9)	1
Wat1	0.143(4)	0.25	0.257(2)	0.8(4)
Wat2	0.489(5)	0.25	0.883(1)	0.95(6)
Cl	0.801(2)	0.25	0.036(6)	0.78(4)
O-H1	1.051(4)	0.25	0.187(2)	0.9(4)
O-H2	0.7393(4)	0.25	0.094(1)	0.70(8)

Table 3. 12 Selected bond distances from refinement of AV3

Bond	Distance (Å)	Bond Valence	Bond	Distance (Å)
Na1_O5	2.97(7)	0.042	**Zr_O2**	2.13(7)
Na1_O6	2.49(5)	0.156	**Zr_O2**	2.37(4)
Na1_O6	2.96(6)	0.044	**Zr_O5**	2.45(5)
Na1_O7	2.80(4)	0.068	**Zr_O5**	2.51(4)
Na1_O10	2.21(3)	0.334	**Zr_O6**	1.76(7)
Na1_Wat2	2.29(5)	0.267	**Zr_O6**	1.85(5)
Na1_Cl	3.72(7)		**Zr_O8**	2.17(8)
Na1_O-H2	3.08(3)	0.032	**Zr_O8**	2.43(8)
SUM		0.942		
			Si1_O1	1.66(7)
Na2_O2	2.52(7)	0.143	**Si1_O2**	1.36(8)
Na2_O3	3.13(3)	0.028	**Si1_O3**	1.51(5)
Na2_O4	2.38(7)	0.211	**Si1_O4**	1.93(3)
Na2_O5	2.40(8)	0.201		
Na2_O5	3.02(6)	0.037	**Si2_O4**	1.74(7)
Na2_Wat1	2.72(6)	0.083	**Si2_O7**	1.20(7)
Na2_Cl	2.30(5)			
Na2_O-H1	2.15(7)	0.391	**Si3_O7**	1.66(5)
SUM		1.093	**Si3_O8**	1.71(5)
			Si3_O9	1.70(3)
Na3_O1	2.68(5)	0.094	**Si3_O10**	1.56(7)
Na3_O2	2.26(6)	0.289		
Na3_O8	2.47(3)	0.167		
Na3_Cl	3.02(7)	0.038		
Na3_Cl	3.60(4)			
Na3_O-H2	2.36(7)	0.222		
SUM		0.810		

Table 3. 13 Selected bond angles from refinement of AV3

Bond	Angle(°)	Bond	Angle(°)
O2_Zr_O2	94.6(8)	**O1_Si1_O2**	115.3(7)
O2_Zr_O5	87.5(5)	**O1_Si1_O3**	112.4(8)
O2_Zr_O6	91.9(7)	**O1_Si1_O4**	105.8(8)
O2_Zr_O6	113.5(6)	**O2_Si1_O3**	124.8(4)
O2_Zr_O8	83.6(6)	**O2_Si1_O4**	92.7(6)
O2_Zr_O8	167.1(8)	**O3_Si1_O4**	99.5(6)
O2_Zr_O5	95.8(8)		
O2_Zr_O6	106.5(4)	**Si2_Si2_O4**	113.6(7)
O2_Zr_O6	82.4(6)	**Si2_Si2_O7**	135.7(8)
O2_Zr_O8	174.9(5)	**O4_Si2_O7**	98.9(6)
O2_Zr_O8	73.2(7)		
O5_Zr_O6	157.7(8)		
O5_Zr_O6	158.9(6)	**O7_Si3_O8**	115.5(4)
O5_Zr_O8	88.9(7)	**O7_Si3_O9**	121.4(8)
O5_Zr_O8	97.8(6)	**O7_Si3_O10**	101.9(5)
O6_Zr_O6	31.0(6)	**O8_Si3_O9**	111.4(6)
O6_Zr_O8	68.9(7)	**O8_Si3_O10**	106.6(8)
O6_Zr_O8	87.6(8)	**O9_Si3_O10**	96.3(4)
O6_Zr_O8	93.9(4)		

Whilst the overall structure matches well with that reported in literature[82], some bond distances shown in Table 3.12 appear to be erroneous. The Zr-O6 bond distances reported are too small at 1.79 Å and 1.85 Å as the expected average bond distance is ~2 Å; This may be due to some disorder in the structure or, more likely given the reasonably high errors in this refinement, that the O6 position is inaccurate. The bond valence sums of the cation positions are approximately 1, which is what is expected for a monovalent cation.

After obtaining a pure product, AV-3 was added to solutions of varying concentrations of $Sr(NO_3)_2$ in order to examine any ion exchange capacity as shown in Table 3.14.

Table 3. 14 - Compositions of solids, reported as oxides as measured by XRF after initial exchange experiments

→$Sr(NO_3)_2$ concentration ↓Compound	Parent	0.01 M	0.05 M	0.5 M	1.0 M
ZrO_2	49.29	57.18	60.61	46.95	54.12
SiO_2	31.58	29.62	25.79	28.78	28.68
SrO	0.00	5.49	4.85	13.34	10.77
Na_2O	15.26	4.14	4.67	7.91	3.56
Cl	3.87	3.57	4.07	3.01	2.89

Elemental analysis of the solid after exchange by XRF indicated the presence of strontium in the material with a decrease in the levels of sodium, which is a good indication of ion exchange occurring and not adsorption on the surface of the material of strontium salts.

SEM and EDX, Figures 3.15 & 3.16, were used to examine the crystal size and shape and to check for the presence of any strontium-containing amorphous material which would not be evident from X-ray diffraction but would likely appear as globular or irregularly shaped materials on SEM images. The SEM used to acquire these images was a Philips XL-30 FEG Environmental SEM with EDS. To acquire images an accelerating voltage of 15 keV with a spot size of 3, for EDX the spot size was increased to 5 and a voltage of 20 keV was used.

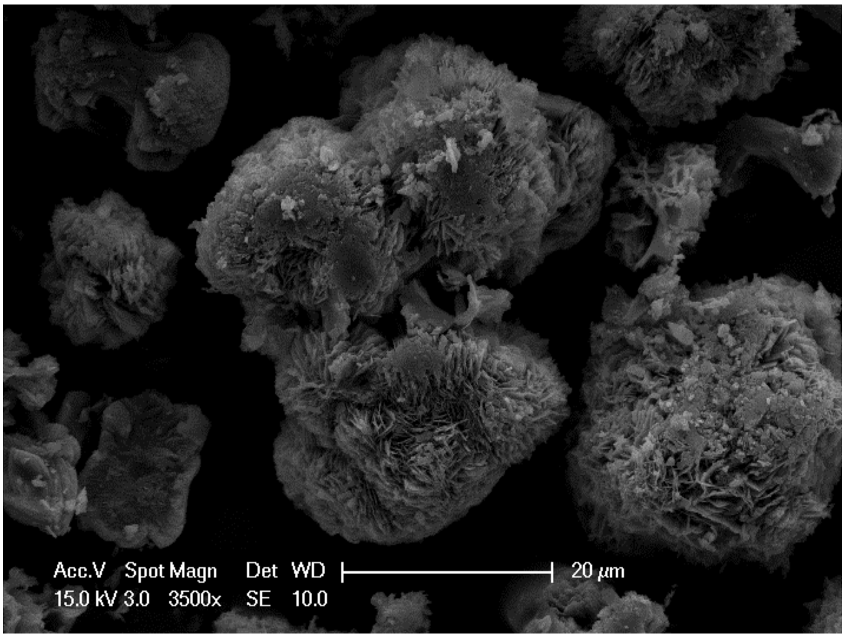

Figure 3. 15 - SEM image of AV-3 as a powder dispersed over carbon tape followed by platinum sputter coating

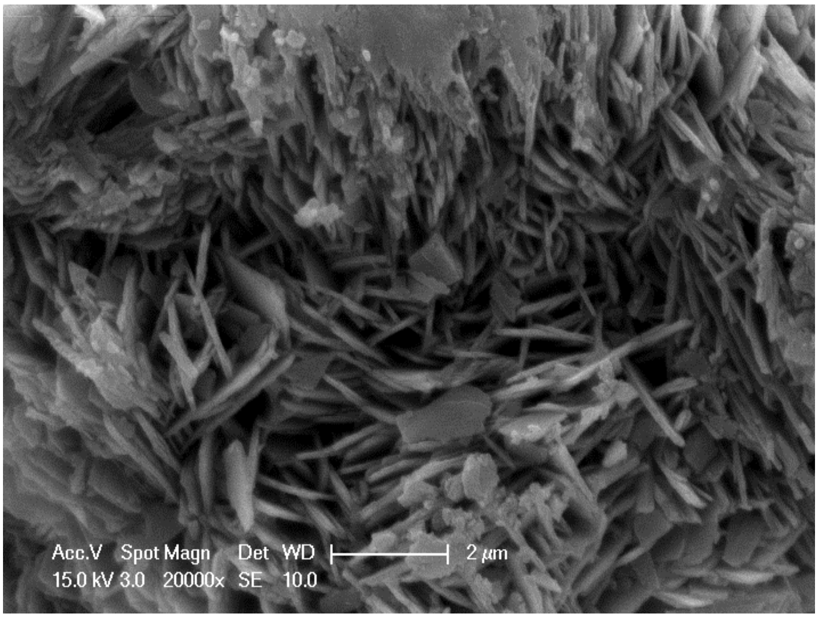

Figure 3. 16 - SEM image of AV-3 as a powder dispersed over carbon tape followed by platinum sputter coating

The parent material can be seen to be composed of plate-like crystals clustered together, with no obvious signs of amorphous material. EDX over an area indicates the average composition

After ion exchange the plate-like crystals are maintained with no morphology changes or amorphous material evident. As seen in Figure 3.17 the strontium peak in the EDX cannot be distinguished from the silicon peak due to the overlapping emission energies.

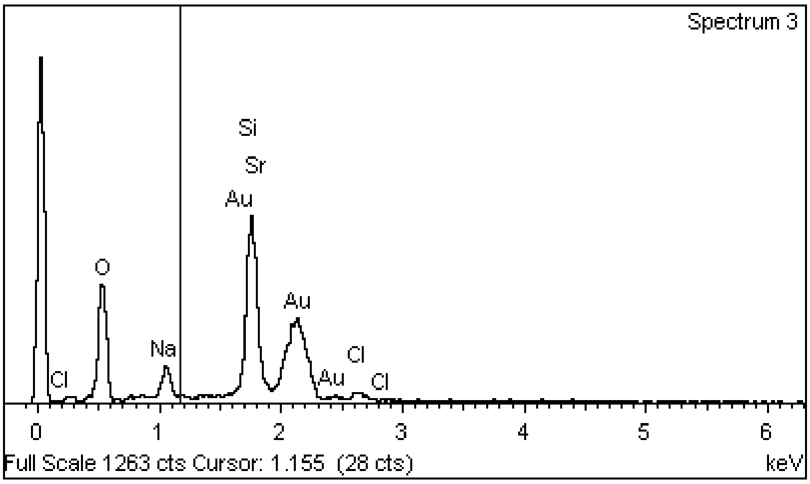

Figure 3. 17 - EDX spectrum of SEM images indicating Sr/Si overlap

Initially a powder X-ray diffraction pattern for the strontium-exchanged material was obtained with a lab-based Bruker D8 diffractometer which resulted in poor quality data with very broad peaks similar to the previous pattern recorded as shown in Figure 3.13, however, later high quality synchrotron data was obtained from the I11 beamline at the Diamond Light Source which allowed for a much better fit to be obtained. The data in Figure 3.18 were acquired using the I11 MAC detectors with a wavelength of 0.825704(2) Å and a zero-point of 0.000792(2)°.

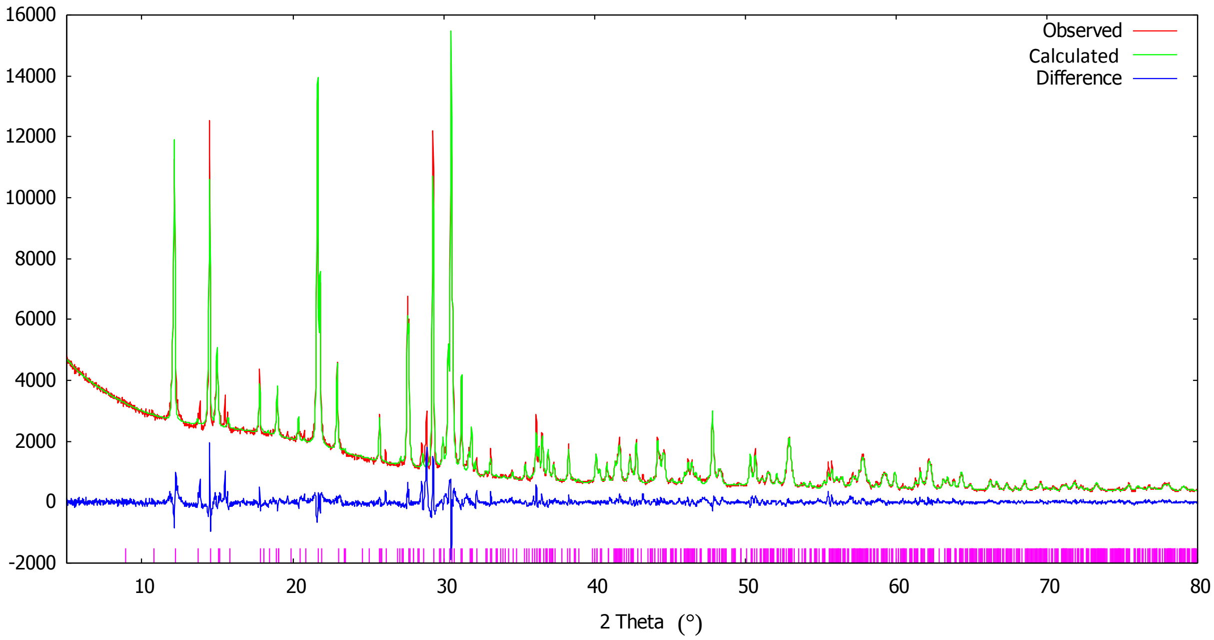

Figure 3. 18 - Rietveld refinement of AV-3 performed using TOPAS 4.1 Academic

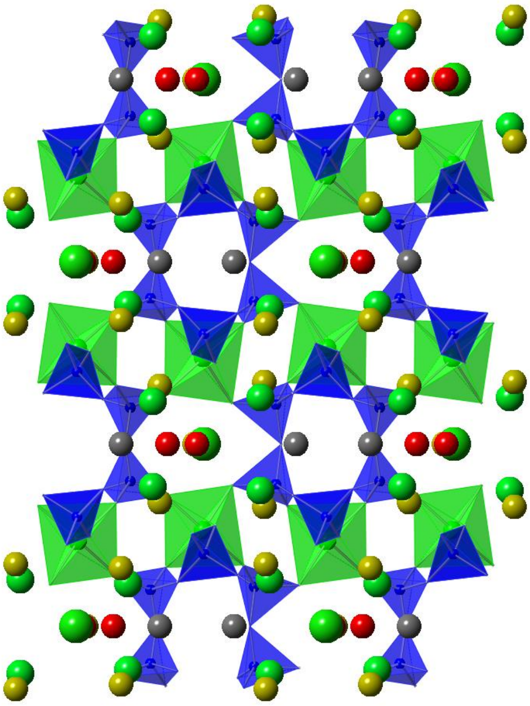

Figure 3. 19 - Refined structure of Sr-exchanged AV-3 viewed along (001) with blue SiO tetrahedral, green ZrO_6 octahedra, yellow Na^+ spheres, large green Cl^- spheres, small green Sr^{2+} spheres and red and grey water spheres.

Table 3. 15 - Rietveld refinement parameters for AV-3 displacement parameters were fixed

***a* /Å**	10.801(1)		
***b* /Å**	14.494(2)	**Background**	Chebyshev
***c* /Å**	6.613(7)		
β /°	113.251(8)	**Peak shape profile**	Thompson-Cox Hastings
V /Å^3	951.9(8)		
space group	$P2_1/m$		
Z	4		
NO. independent parameters	115		
R_{wp}	4.17		
R_{exp}	0.562		
R_p	3.073		

Site	***x***	***y***	***z***	***occ***	**B_{eq}**
Na1	0.526(6)	0.136(6)	0.989(7)	0.620(4)	1.0
Na2	0.509(4)	0.006(6)	-0.089(9)	0.444(5)	1.0
Na3	0.964(9)	0.25	0.568(9)	0.436(7)	1.0
Sr1	0.925(9)	0.116(2)	0.917(4)	0.401(1)	1.0
Sr2	0.806(9)	0.215(9)	0.024(9)	0.101(1)	1.0
Sr3	0.759(3)	0.25	0.608(5)	0.436(1)	1.0
Zr	0.749(1)	0.015(1)	0.514(2)	1	1.0(1)
Si1	0.043(2)	0.126(2)	0.593(7)	1	0.7(6)
Si2	0.254(3)	0.055(2)	1.007(9)	1	1.2(5)
Si3	0.459(2)	0.157(2)	0.4(5)	1	0.7(4)
O1	0.06(4)	0.25	0.622(9)	1	1.2(3)
O2	0.902(3)	0.122(4)	0.436(7)	1	1.8(5)
O3	0.096(4)	0.108(4)	0.454(9)	1	1.1(9)
O4	0.145(3)	0.121(3)	0.876(7)	1	0.7(8)
O5	0.787(4)	0.02(4)	0.862(9)	1	0.5(7)
O6	0.698(3)	0.043(4)	0.049(9)	1	1.0(4)
O7	0.393(3)	0.05(3)	0.289(7)	1	0.7(8)
O8	0.64(2)	0.111(5)	0.431(8)	1	0.8(5)
O9	0.441(3)	0.25	0.386(9)	1	1.1(5)
O10	0.409(4)	0.097(4)	0.584(7)	1	1.0(6)
Wat1	0.078(3)	0.25	0.131(9)	1	1.1(7)
Wat2	0.375(5)	0.25	0.878(8)	1	1.2(6)
Cl	0.732(5)	0.25	0.063(6)	0.651(7)	1.0
O-H1	0.778(9)	0.25	-0.163(7)	0.338(9	1.0
O-H2	0.821(9)	0.25	0.432(9)	0.562(7)	1.0

Table 3. 16 - Refined bond distances and valence sums for AV-3

Bond	Distance (Å)	Bond Valence Sums
Na1-O6	2.22(7)	0.33
Na1-O7	2.33(6)	0.24
Na1-O10	2.42(6)	0.19
Na1-O6	2.54(8)	0.13
Na1-Wat2	2.81(8)	
Na1-O7	3.10(8)	0.03
Na1-O8	3.42(7)	0.01
Na1-O5	3.59(6)	0.01
	Total	0.94

Bond	Distance (Å)	Bond Valence Sums
Sr1-Wat2	2.34(6)	
Sr1-O10	2.35(5)	0.538
Sr1-O6	2.45(5)	0.41
Sr1-O7	2.57(5)	0.294
Sr1-O6	3.11(8)	0.069
Sr1-O-H1	3.34(9)	
Sr1-O9	3.41(7)	0.03
Sr1-O8	3.48(7)	0.025
Sr1-O8	3.54(6)	0.022
Sr1-O7	3.56(6)	0.02
Sr1-O5	3.60(5)	0.018
Sr1-O4	3.92(7)	0.008
	Total	1.434

Bond	Distance (Å)	Bond Valence Sums
Na2-O5	2.00(6)	0.58
Na2-O3	2.50(6)	0.15
Na2-Wat1	2.78(8)	
Na2-O-H1	2.79(8)	
Na2-O6	2.86(7)	0.06
Na2-O2	3.12(7)	0.03
Na2-O5	3.15(5)	0.03
Na2-O4	3.17(8)	0.02
Na2-O4	3.32(6)	0.02
Na2-O-H2	3.45(8)	
	Total	0.89

Bond	Distance (Å)	Bond Valence Sums
Sr2-Wat1	2.12(6)	
Sr2-O-H1	2.45(5)	
Sr2-O5	2.48(5)	0.38
Sr2-O4	2.65(7)	0.24
Sr2-O3	2.73(6)	0.19
Sr2-O2	2.75(6)	0.18
Sr2-O5	3.19(5)	0.06
Sr2-O-H2	3.46(8)	
Sr2-O6	3.53(9)	0.02
Sr2-O1	3.80(8)	0.01
Sr2-O8	3.86(5)	0.01
Sr2-O1	3.95(4)	0.01
Sr2-O2	3.96(6)	0.01
	Total	1.11

Bond	Distance (Å)	Bond Valence
Na3-O8	2.45(7)	0.18
Na3-O8	2.45(8)	0.18
Na3-O-H2	2.70(6)	0.09
Na3-O2	2.79(6)	0.07
Na3-O2	2.79(5)	0.07
Na3-Wat1	3.23(8)	0.02
Na3-O9	3.45(7)	0.01
Na3-O1	3.54(6)	0.01

Bond	Distance (Å)	Bond Valence
Sr3-O8	2.04(7)	1.24
Sr3-O8	2.04(7)	1.24
Sr3-O-H1	2.20(7)	
Sr3-O2	2.53(8)	0.33
Sr3-O2	2.53(5)	0.33
Sr3-O9	3.22(9)	0.05
Sr3-O1	3.24(4)	0.05
	Total	3.24

	Total	0.62

Table 3. 17- Refined bond angles for AV-3

Bond	Angle °	**Bond**	Angle °
O2-Zr-O3	85.3(3)	**O1-Si1-O2**	121.0(3)
O2-Zr-O5	86.2(3)	**O1-Si1-O3**	114.6(3)
O2-Zr-O6	92.7(4)	**O1-Si1-O4**	102.3(4)
O2-Zr-O8	82.4(2)	**O2-Si1-O3**	110.9(4)
O2-Zr-O10	171.6(2)	**O2-Si1-O4**	100.2(5)
O3-Zr-O5	84.6(1)	**O3-Si1-O4**	104.7(3)
O3-Zr-O6	94.44(9)		
O3-Zr-O8	167.6(2)	**O4-Si2-O5**	108.4(4)
O3-Zr-O10	95.4(1)	**O4-Si2-O6**	120.0(2)
O5-Zr-O6	178.6(2)	**O4-Si2-O7**	105.2(1)
O5-Zr-O8	93.2(2)	**O5-Si2-O6**	107.4(1)
O5-Zr-O10	85.5(3)	**O5-Si2-O7**	108.1(2)
O6-Zr-O8	87.5(3)	**O6-Si2-O7**	107.3(3)
O6-Zr-10	95.6(2)		
O8-Zr-O10	96.3(4)	**O7-Si3-O8**	107.4(1)
		O7-Si3-O9	112.2(2)
		O7-Si3-O10	112.5(2)
		O8-Si3-O9	98.8(4)
		O8-Si3-O10	114.9(4)
		O9-Si3-O10	110.3(2)

When examining Tables 3.16 and 3.17 it should be considered that X-ray diffraction and the Rietveld method have been used to derive the structure thus the sites are averaged and so whereas there appears to be two cations in each pore it is more likely the case there is only one cation with equal occupancies over the two equivalent positions. In the case of the cations within the pore they refined as if all the species present in the pore void of the framework—Na, Sr, Cl, OH and H_2O—were in the pore at the same time but have fractional occupancies. When introducing Sr^{2+} into the structure a sodium atom will need to be removed, this may cause the framework around this vacant site to shift to move closer to another cation within the pore. The averaging of defects in the framework caused by missing cations may be the cause of the apparent shorter than expected bond distances observed, such as Na2-O5, however, it is difficult to confirm this and further work would be useful.

For this refinement Na and Sr sites were initially constrained to be on the same positions with occupancies fixed to ensure charge balancing; as the refinement became more stable these constraints were relaxed. This method, whilst helping to ensure a stable refinement, can limit the movement of cations within the pore and in addition it assumes all sites will exchange equally, which is not likely to be the case.

The Sr3 sites in particular have bond valence sums which appear normally high, due to duplicate Sr3-O8 bonds which are unusually small, implying that the Sr^{2+} cations would not reside in the Sr3 site due to the proximity to O8. However, the refined occupancies indicate that the Sr3 site does contain a high portion of the exchanged strontium. In this case if the refined occupancies are to be believed it is likely that either cation site position is not exactly correct and the true bond distances are larger, or that the framework differs when the pore contains strontium compared to when the pore contains sodium and this discrepancy causes an apparently small bond which does not exist in reality.

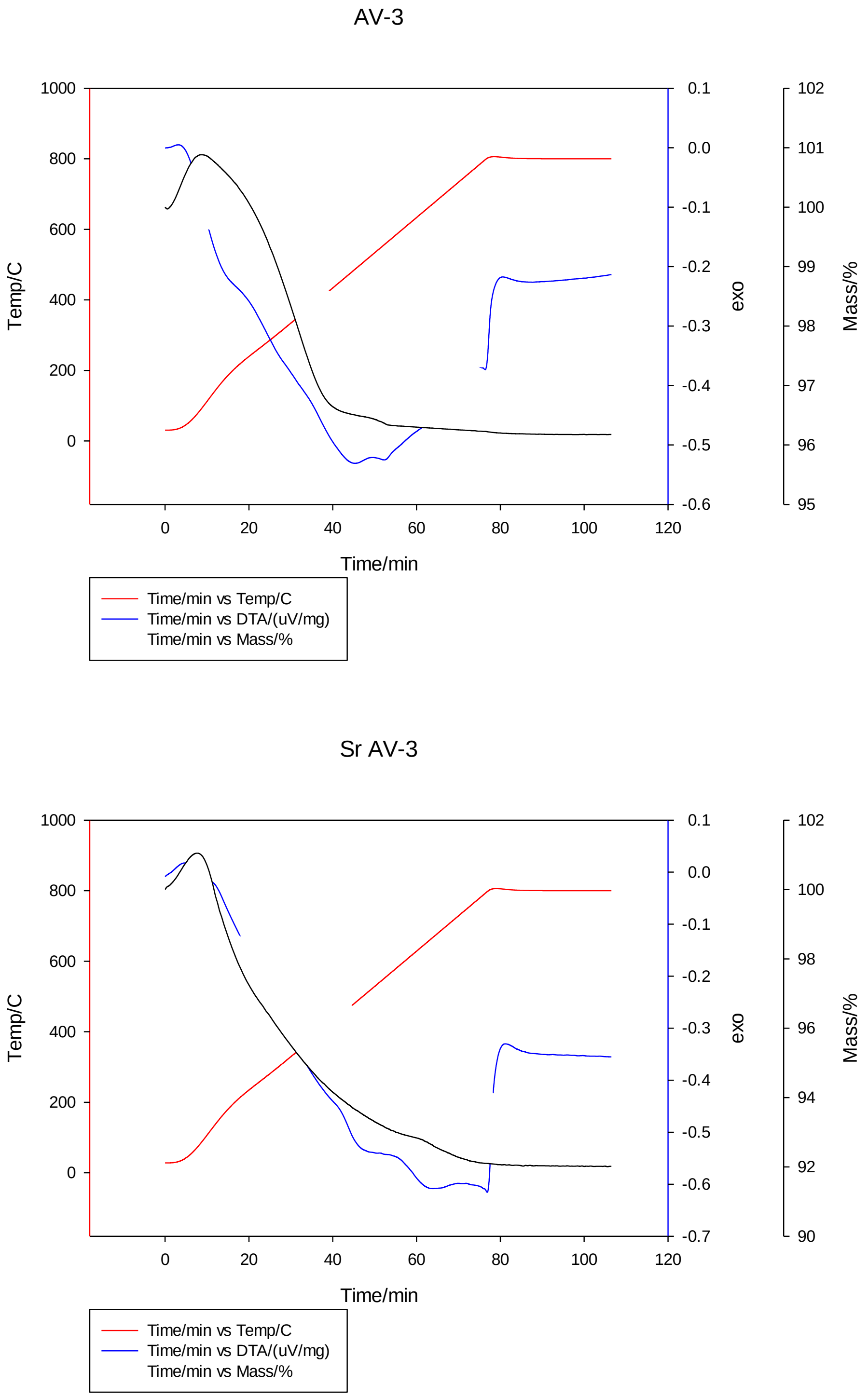

Figure 3. 20 - TGA traces of AV3 (above) and Sr-AV3 (below) including DTA trace

By examining the TGA data shown in Figure 3.20, strontium exchange appears to lead to a change in the strength of structurally bound water based, on the DTA trace and temperature of water loss observed. This is also observed in Chapter 4 when examining TGA data of Sr-AV7. The mass loss due to water occurring from 200°C is more rapid in the strontium-exchanged sample compared to the pristine material and the DTA trace indicates a more intense endothermic event in the pristine material.

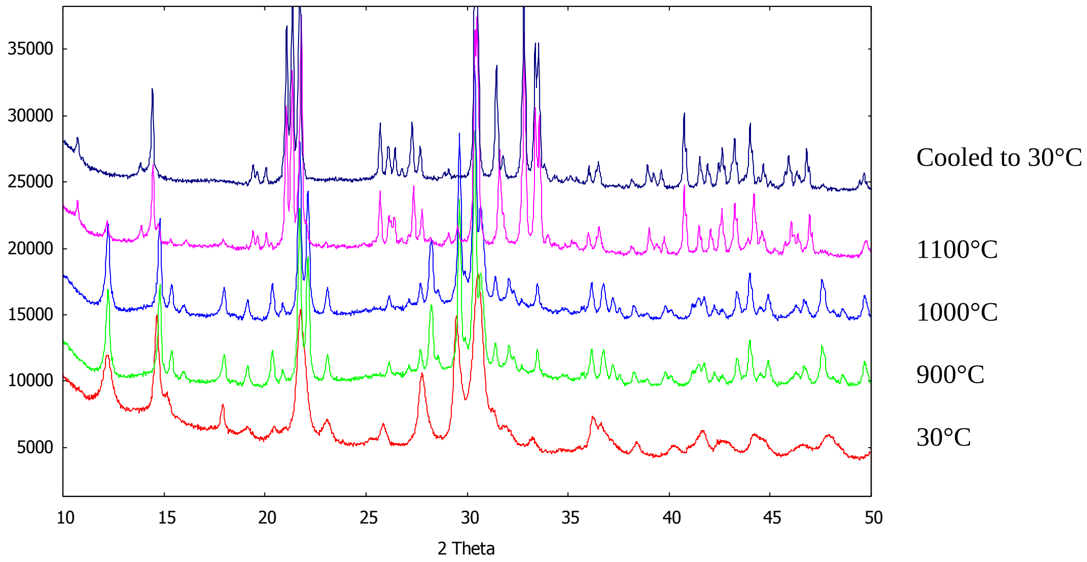

Figure 3. 21 - Variable temperature XRD patterns of AV-3 heated from room temperature to 1000 °C followed by cooling back to room temperature

High temperature treatment could potentially lead to collapsed structures with more desirable low leaching properties; to study this samples have been heat treated slowly at 1 °C/min using an Anton-Parr heating stage coupled to a Bruker D8 X-ray diffractometer. Sr-AV3 undergoes a phase transition to a trinclinic phase (*P*-1) parakeldyshite when heated to high temperatures as shown in Figure 3.21. The phase change is non-reversible. It is unclear whether this proceeds via an intermediate phase or gradual transformation with an expansion in the unit cell as expected from heating. No impurity Sr-containing phases have been detected after cooling, suggesting any strontium remains in the structure or is in an amorphous phase.

The parakeldyshite phase was refined as shown in Figure 3.22 to obtain a model shown in Figure 3.23; data was acquired from the I11 beamline at Diamond light source using the MAC detector and a wavelength of 0.825704(2) Å and a zero-point of 0.000792(2)°.

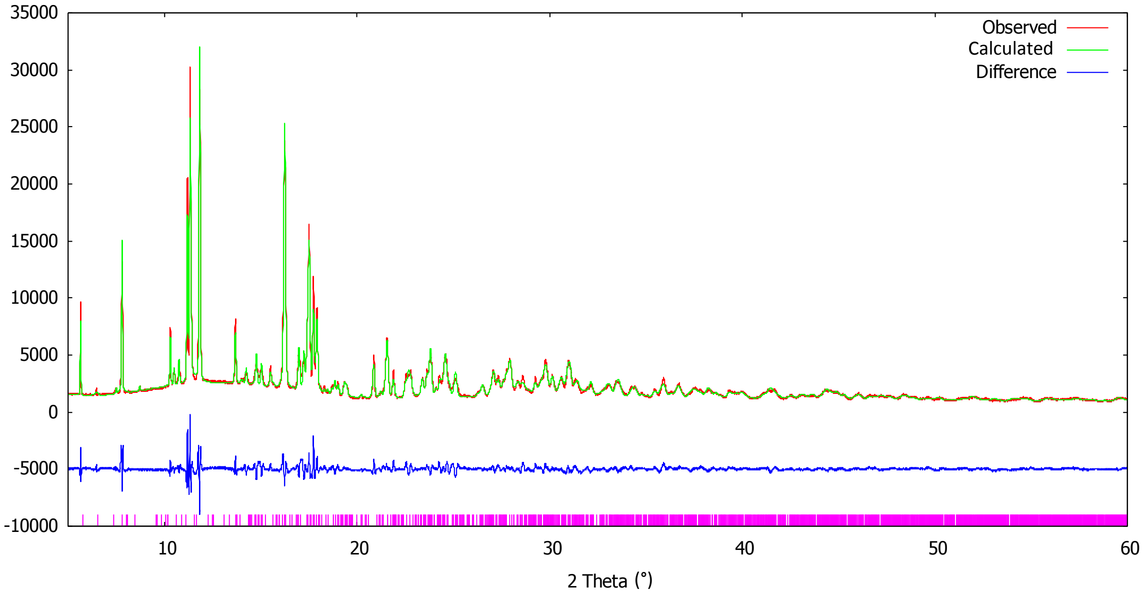

Figure 3. 22 - Rietveld refinement of parakeldyshite performed using TOPAS academic 4.1 from synchrotron data acquired from the I-11 beamline at the Diamond light source

In comparison to AV-3, parakeldyshite has lost some of the SiO_4 connectivity. In AV-3 the tetrahedra form rings of 6 units whereas in parakeldyshite the tetrahedra form pairs connected by ZrO_6 octahedra. In comparing the bond valence sums shown in Tables 3.16 & 3.19, site Sr1 and Sr2 in AV-3 both have less strong binding between the Sr^{2+} cation and the framework in comparison to parakeldyshite, 1.434 & 1.11 vs 2.46 &1.88, although the Sr3 site in AV-3, which does not exist in parakeldyshite, remains the strongest binding site for Sr^{2+} with a bond valence sum of 3.24, which is significantly higher than the expected value of 2. The higher than expected value is due to the close proximity of 4 structural oxygen atoms in the framework, although it is possible that the Sr3 position is in fact an averaged position and the Sr^{2+} cation in this site has equal occupancy in positions closer to one pair of these four oxygen atoms. Refining the displacement parameter may have been able to reveal this, however, due to the correlation to occupancy it was decided to fix this parameter in favour of refining the occupancy. It should also be noted that the Zr-O6 bond distance appears abnormally long, ~2.2 Å compared to an average of ~2 Å. Whether this is an artefact of the refinement or a real bond distance is unclear; as this is a high temperature phase it would not be unreasonable to expect some distortions or disorder.

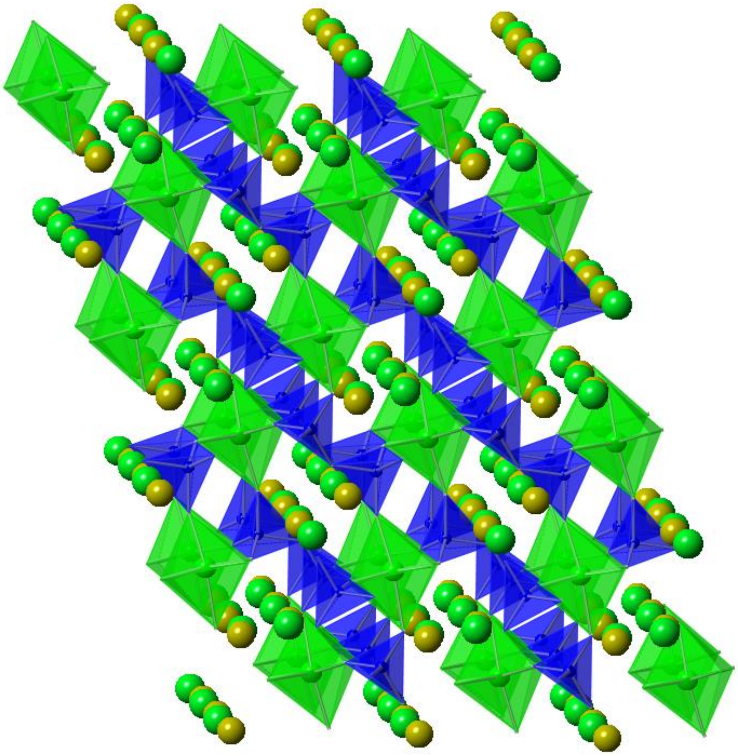

Figure 3. 23 - Refined structure of Sr-parakeldyshite - high temperature phase from AV-3 viewed along the c axis with ZrO_6 in green, SiO_4 in blue and sodium and strontium cations in yellow and green, respectively.

Table 3. 18 - Rietveld refinement details of parakeldyshite

***a* /Å**	6.674(1)	**α /°**	92.35(2)
***b* /Å**	8.829(2)	**β /°**	93.78(1)
***c* / Å**	5.433(1)	**γ /°**	71.09(2)
V /Å^3	302.1(1)		
space group	*P*-1	**Background**	Chebyshev
Z	2		
NO. independent parameters	100	**Peak shape profile**	Thompson-Cox Hastings
R_{wp}	6.264		
R_{exp}	1.078		
R_p	4.79		

Site	***x***	***y***	***z***	***occ***	**B_{eq}**
Zr1	0.288(2)	0.2673(2)	0.2237(3)	1	1.08(8)
Si1	0.6442(7)	0.1542(5)	0.769(8)	1	1.27(8)
Si2	0.9329(7)	0.3305(5)	0.6865(9)	1	1.30(7)
Na1	0.859(3)	0.078(2)	0.251(2)	0.55(3)	1
Na2	0.34(5)	0.512(4)	0.817(9)	0.39(5)	1
Sr1	0.912(3)	0.121(3)	0.28(3)	0.12(8)	1
Sr2	0.356(2)	0.4965(2)	0.756(5)	0.22(4)	1
O1	0.289(1)	0.0392(8)	0.175(1)	1	1.11(2)
O2	0.876(1)	0.1794(8)	0.738(1)	1	0.75(2)
O3	0.4988(9)	0.2219(7)	0.521(1)	1	1.26(9)
O4	0.552(1)	0.2444(9)	0.017(1)	1	1.1(1)
O5	0.016(1)	0.3121(8)	0.417(1)	1	0.7(2)
O6	0.111(1)	0.3376(8)	0.853(1)	1	1.0(2)
O7	0.243(1)	0.5207(7)	0.2687(1)	1	0.6(2)

Table 3. 19 - Selected bond distances from the refined structure of parakeldyshite

Bond	Distance(Å)	Bond	Distance(Å)	Bond Valence	Bond	Distance(Å)	Bond Valence
Zr1 -O1	2.02(7)	**Na1-O1**	2.75(2)	0.08	**Sr1-O1**	2.48(2)	0.38
Zr1 -O3	2.03(6)	**Na1-O1'**	2.84(2)	0.06	**Sr1-O2**	2.53(2)	0.33
Zr1 -O4	2.09(7)	**Na1-O2**	2.38(2)	0.21	**Sr1-O2'**	2.57(2)	0.29
Zr1 -O5	2.08(8)	**Na1-O2'**	2.77(2)	0.07	**Sr1-O2''**	2.99(2)	0.09
Zr1 -O6	2.27(6)	**Na1-O2''**	2.98(2)	0.04	**Sr1-O3**	2.98(2)	0.10
Zr1 -O7	2.17(8)	**Na1-O3**	2.804(2)	0.07	**Sr1-O4**	2.64(2)	0.24
		Na1-O4	2.41(2)	0.19	**Sr1-O5**	2.11(3)	1.02
Si1-O1	1.65(8)	**Na1-O5**	2.71(2)	0.09		**Total**	2.46
Si1-O2	1.55(9)		**Total**	0.81	**Sr2-O3**	2.62(2)	0.26
Si1-O3	1.63(7)	**Na2-O3**	2.90(5)	0.05	**Sr2-O4**	2.61(2)	0.26
Si1-O4	1.59(9)	**Na2-O4**	2.59(4)	0.12	**Sr2-O4'**	2.61(2)	0.26
		Na2-O5	2.66(4)	0.10	**Sr2-O5**	2.65(2)	0.24
Si2-O2	1.65(9)	**Na2-O6**	2.52(4)	0.14	**Sr2-O6**	2.57(2)	0.29
Si2-O5	1.59(9)	**Na2-O7**	2.57(6)	0.13	**Sr2-O7**	2.64(2)	0.24
Si2-O6	1.46(9)	**Na2-O7'**	2.77(4)	0.07	**Sr2-O7'**	2.70(3)	0.21
Si2-O7	1.48(7)	**Na2-O7''**	3.00(6)	0.04	**Sr2-O7''**	2.92(3)	0.11
				0.65		**Total**	1.88

Table 3. 20 - Selected framework bond angles from the refined structure of parakeldyshite

Bond	Angle °	Bond	Angle °	Bond	Angle °
O1-Zr-O3	94.69(3)	**O1-Si1-O2**	102.77(4)	**O2-Si2-O5**	107.96(4)
O1-Zr-O4	95.26(3)	**O1-Si1-O3**	107.55(5)	**O2-Si2-O6**	109.48(3)
O3-Zr-O6	166.61(3)	**O1-Si1-O4**	118.46(6)	**O2-Si2-O7**	112.41(4)
O4-Zr-O5	174.56(6)	**O2-Si1-O3**	106.71(7)	**O5-Si2-O6**	105.88(3)
O1-Zr-O7	172.46(4)	**O2-Si1-O4**	107.55(4)	**O5-Si2-O7**	114.40(3)
O4-Zr-O7	171.47(6)	**O3-Si1-O4**	114.5(3)	**O6-Si2-O7**	106.42(6)
O4-Zr-O8	88.86(4)				

3.4 Conclusions

In this chapter brief investigations aimed at preparing new titano and zirconosilicate materials were made, with a hydrothermal synthesis and characterization of titanite and attempts at preparing ion-exchanged forms reported. Titanite appears not to undergo ion exchange easily due to strong binding of the calcium cation although computational modelling would help support this. Synthetic petarasite-AV-3 has been prepared along with an ion-exchanged counterpart and the structural changes through ion exchange and heat treatment investigated. Upon heat treatment AV-3 can be seen to transform in to a denser parakeldyshite phase.

Chapter 4: Tin silicates

4.1 Introduction

As previously discussed in chapter 1 little work has been undertaken on the synthesis of tin silicate materials and less on the ion exchange properties of these materials. The majority of papers are based on the structure of mineralogical samples although some work on synthesis was done on behalf of the Exxon Research and Engineering group[89]; e.g. Lin *et al.* described the structure of a synthetic tin variant of the natural mineral kostylevite, AV-7, as described in Chapter 1. This work was followed up with a report on the structure of another tin silicate[90] Sn AV-11, $K_4SnSi_6O_{18}$, a rhombohedral system with similar extended chains of –O-Si-O- units as in AV-7 and umbite. AV-11can be produced directly or by the high temperature treatment of AV-7. High temperature treatment of materials commonly leads to more dense phases and so the heat treatment of ion-exchanged materials has the potential to lead to more ideal waste forms for long term storage with lower porosity and ion exchange properties. Tin has two common oxidation states, II and IV, the latter being the more stable. Adjusting the oxidation state of tin could potentially lead to new materials and/or change the ion exchange properties due to a change in the charge of the framework and thus the attraction between framework and cations. This chapter contains results from exploratory synthesis in the sodium-tin-silicate system. Conditions similar to those used to produce AV-7 by Lin *et al.* [37] were used as a starting point. Preliminary ion exchange work on AV-7 followed along with the structural changes caused by this ion exchange and subsequent heat treatments.

4.2 Experimental

4.2-1 Hydrothermal SnO_2-SiO_2-NaOH synthesis survey

Informed by the synthesis conditions of AV-7, a brief survey in varying compositions was attempted to find possible new materials. Ten different ratios (Table 4.1) of SiO_2 (colloidal silica, Ludox® HS-40), SnO_2 and NaOH were combined by dissolving NaOH and SnO_2 in 20 cm^3 water before adding Ludox® HS-40 to form gels before homogenizing for 40 minutes then heating hydrothermally under autogenous pressure in Parr acid digestion vessels to 230°C for one week.

Table 4. 1 - Mass compositions (g) of SiO_2-SnO_2-NaOH survey

Ref	SnO_2	SiO_2	NaOH	Mole Ratio
Sn_Si_1	1	5.02	0.60	1: 2: 0.9
Sn_Si_2	1	5.02	1.26	1: 2: 1.9
Sn_Si_3	1	5.02	2.83	1: 2: 4.2
Sn_Si_4	1	5.02	4.85	1: 2: 7.3
Sn_Si_5	1	5.02	7.54	1: 2: 11.3
Sn_Si_6	1	5.02	11.30	1: 2: 17
Sn_Si_7	1	6.27	1.88	1: 2.5: 2.8
Sn_Si_8	1	6.27	3.23	1: 2: 4.8
Sn_Si_9	1	6.27	5.02	1: 2.5: 7.5
Sn_Si_10	1	6.27	7.54	1: 2.5: 11.3
Sn_Si_11	1	4.18	1.57	1: 1.67: 2.4
Sn_Si_12	1	4.18	2.69	1: 1.67: 4.0
Sn_Si_13	1	4.18	4.19	1: 1.67: 6.3
Sn_Si_14	1	4.18	6.28	1: 1.67: 9.4

4.2-2 Microwave Tin^{II} survey

A brief investigation into forming mixed sodium Sn^{II}/Sn^{IV} silicate species, altering the ratio of Sn^{II} : Sn^{IV} whilst maintaining the Na:Si:Sn ratio of 30:5.7:1 was made. A high proportion of NaOH was used to promote hydrolysis of the tin and silicate species, along with high amounts of silica to prevent formation of tin species with no sodium or silicon.

Reagents were combined into a gel according to the compositions in table 4.2 below, by dissolving NaOH, $SnCl_2$ and $SnCl_4·5H_2O$ in 20 cm^3 water before adding Luodx® HS-40 and colloidal silica and homogenizing for 40 minutes before heating to 210°C for 10 h under autogenous pressure using a CEM MARS6 microwave system.

Table 4. 2 – Mass Compositions (g) for microwave Sn^{II} Survey

Ref	$SnCl_4·5H_2O$	$SnCl_2$	colloidal silica	NaOH	Mole ratio
Sn^{II}_1	1.75	0.3	2.7	4	1: 0.3: 9.0: 20.0
Sn^{II}_2	2.63	0.15	2.7	4	1: 0.1: 6.0: 13.3
Sn^{II}_3	0.8	0.45	2.7	4	1: 1.0: 19.7: 43.8
Sn^{II}_4	0	0.6	2.7	4	0: 1: 14.2: 31.6

Following this $SnCl_2$ was replaced with Sn^{II} oxalate and the compositions in table 3 below were made up into precursor gels by dissolving NaOH and Sn^{II} oxalate in 30 cm^3 water followed by adding Ludox® HS-40 colloidal silica. The precursor gels were allowed to homogenize for 30 minutes before heating under autogenous pressure to 210°C for 10 h using a CEM MARS6 microwave system.

Table 4. 3 - Compositions (g) for soidum Sn^{II} oxalate silicates synthesis gels

Ref	Sn^{II} Oxalate	colloidal silica	NaOH	Mole ratio
A	2.067	4.5	0.4	01:03:01
B	2.067	4.5	0.8	01:03:02
C	2.067	4.5	1.2	01:03:03

4.2-3 AV-7 - synthetic tin kostylvite

AV-7 was prepared by dissolving 2.16g KF powder and 4.08g NaOH pellets in 10 cm^3 deionized water. To this was added 3.25 g $SnCl_4 \cdot 5H_2O$ which was stirred until fully dissolved followed by 10.19 g Ludox® HS-40 colloidal silica as opposed to the metasilicate used in the Lin *et al.*[37] method. The mixture was then allowed to homogenize for 40 minutes before heating under autogenous pressure for 5 days at 230°C.

4.2-4 Ion exchanges

4.2-4a Bulk ion exchange

1.00 g of ground AV-7 was added to 25cm^3 of $Sr(NO_3)_2$ solutions of concentrations 0.001 mol^{-1} dm^3, 0.05 mol^{-1} dm^3, 0.5 mol^{-1} dm^3 and 1.0 mol^{-1} dm^3, before shaking for 24 hours. The resultant suspensions were filtered, washed well with deionized water and the solids formed into fused beads for XRF analysis.

4.2-4b Low concentration ion exchange

0.02 g of AV-7 was added to 10 cm^3 of 50 ppm of $Sr(NO_3)_2$ solution in triplicate before shaking for 24 hours before filtering to examine the filtrate by ion chromatography. Each ion chromatography sample is run in triplicate and the session is calibrated with 8 standards of purchased K^+, Na^+ and Sr^{2+} 1000 ppm solutions made up to 5 ppm, 10 ppm, 20 ppm, 30 ppm, 40 ppm, 60 ppm, 100 ppm and 200 ppm of each cation.

4.2-4c Fused bead XRF

Fused beads of each sample were prepared by grinding 0.15 g sample with 3.0 g of mixed 64%/36% lithium metaborate / tetraborate flux. The mixture was then added to a gold-platinum alloy crucible and heated to 1050°C for 7 minutes before removing and adding a small amount (<0.1 g) of ammonium iodide to act as a releasing agent to prevent the glass bead from sticking to the platinum. After re-heating for a further 7 minutes the crucible was removed again then swirled to remove air bubbles. The glass was heated for a further 2 minutes to re-melt the glass and form a smooth even surface before finally cooling and removing the bead from the crucible. This particular flux and high dilution were used due to the propensity of tin to form inclusions within the fused bead matrix. XRF data was collected on an Bruker S8 Tiger spectrometer using a calibrated method using standards prepared with fused beads. The measurement method used a customized method for this system where each element was measured for either 10 or 100 seconds depending on the intensity of the $K\alpha_1$ emission lines used, the total measurement time being approximately 8 minutes a sample.

4.3 Results and discussion

4.3-1 SnO_2-SiO_2-NaOH synthesis survey

Whilst the literature contains a great deal of work done on the mapping of the SiO_2 - ZrO_2 - NaOH system[59], little work has been done on the SnO_2 – SiO_2 – NaOH system. In this series of experiments the hydrothermal method was used with constant time and temperature throughout the series. It is evident that under all conditions, when starting from SnO_2, no metal silicate formation is taking place as cassiterite, SnO_2 adopting the rutile structure, is observed throughout all experiments with various silica and sodium silicate phases as seen in Figure 4.1. It was first considered that the SnO_2 was not decomposing due to lack of a mineralizing agent such as KF, however, these experiments were run with the addition of KF by a year 4 project student, Ryan George and a similar trend was observed. In comparison to the procedure to prepare AV-7 ($NaKSnSi_3O_9 \cdot H_2O$) where $SnCl_4 \cdot 5H_2O$ is used as the source of tin which dissolves readily in water to form hydrated salts, SnO_2 is insoluble in dilute base, requiring a fused alkali hydroxide to form an intermediate, and will not hydrolyse without harsher reaction conditions such as even lower pH or higher temperatures. The rate of hydrolysis of the metal salt vs. the rate of hydrolysis of SiO_2 and indeed the exact identity of the hydrated metal species in the reaction gel is likely an important issue in the formation of these types of metal silicates as the reaction between the M-OH and Si-OH species.

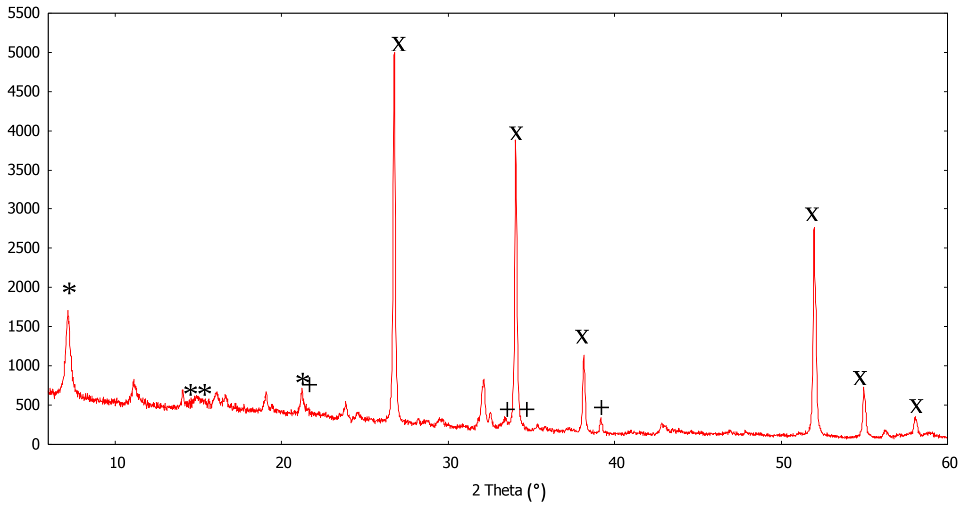

Figure 4. 1 - Typical PXRD pattern from NaOH-SnO_2-SiO_2 series

*** - SiO_2 PDF 04-012-2128**

+ - γ-$Na_2Si_2O_5$ PDF 00-018-1242

x- SnO_2 PDF 04-003-0649

4.3-2 Microwave Tin^{II} survey

Tin^{II} metal silicates are uncommon due to the favourable oxidation of Sn^{II} to Sn^{IV}, under standard hydrothermal conditions, resulting in formation of SnO_2 over several days. However, due to the rapid uniform heating conditions of microwave synthesis Sn^{II} can be used to form a stannosilicate before oxidation occurs, whilst the exact reason for the prevention of oxidation from heating via microwaves is not yet understood it has been proposed that due to Sn^{II}O absorbing microwave radiation much more intensely than Sn^{IV}O$_2$ [91], which may also be the case for the hydrated tin hydroxide species thought to be present in the synthesis gels. Thus microwave heating of precursor gels containing Sn^{II} were attempted in an effort to produce new phases.

Initially a mixture of Sn^{II} and Sn^{IV} chlorides were in varying ratios used in the precursor gels along with NaOH and colloidal silica before microwave treatment. Despite varying the ratio of Sn^{II}:Sn^{IV} there was no great difference in the observed phases, as seen in Figure 4.2, tin-containing phases appearing to be various chlorides and silicon-containing phases to be primarily sodium silicate type phases however, there are a number of unidentified peaks which may correspond to a stannosilicate material although indexing the pattern was not successful.

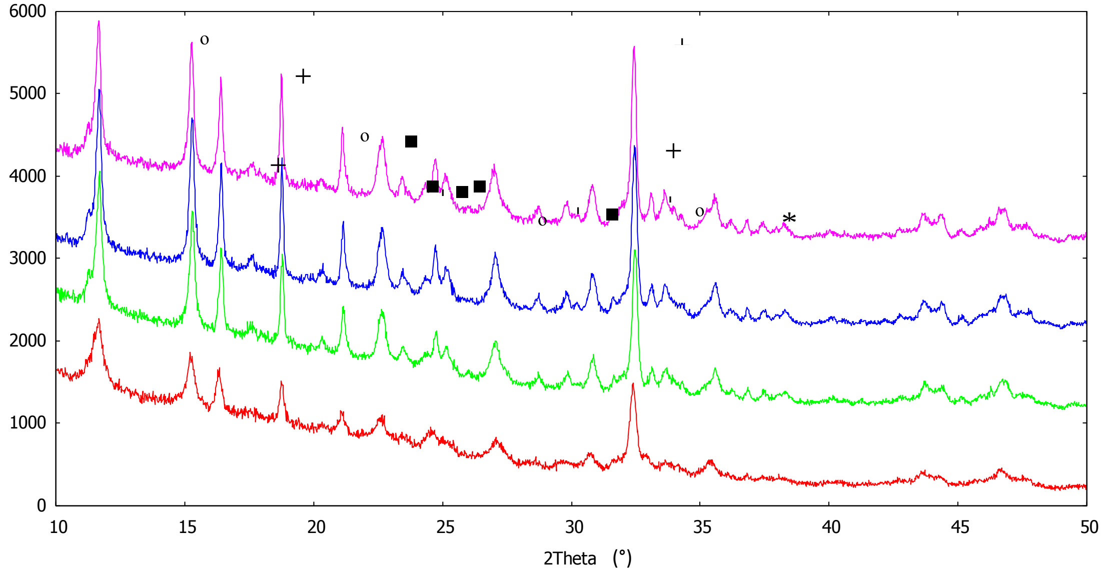

Figure 4. 2 - Diffraction patterns of Sn^{II}:Sn^{IV} chloride microwave synthesis attempts

■ - δ-$Na_2Si_2O_5$ PDF 00-053-1234

o - γ-$Na_2Si_2O_5$ PDF 04-014-8492

+ - $Na_2(SiO_2(OH)_2)$ ·$8H_2O$ PDF 00-060-0360

Upon switching to a different source of Sn^{II}, tin oxalate, a new phase was prepared across a variety of Sn:Si ratios and pH conditions which may indicate the new phase is a thermodynamically stable, easy to form phase. No structure matching this diffraction pattern has been found in the PDF database, nor any structure which matches the cell which has been indexed as face centred cubic system, with a=10.39 Å. Using space group of Fm-3m, one of five in the F--- extinction group, a Pawley fit, Figure 4.3, has been performed which indicates good agreement between the predicted peak positions and observed without an excessive number of unobserved reflections. The structure of the new material has yet to be solved, however ion exchange experiments have been performed and no observed uptake has been shown.

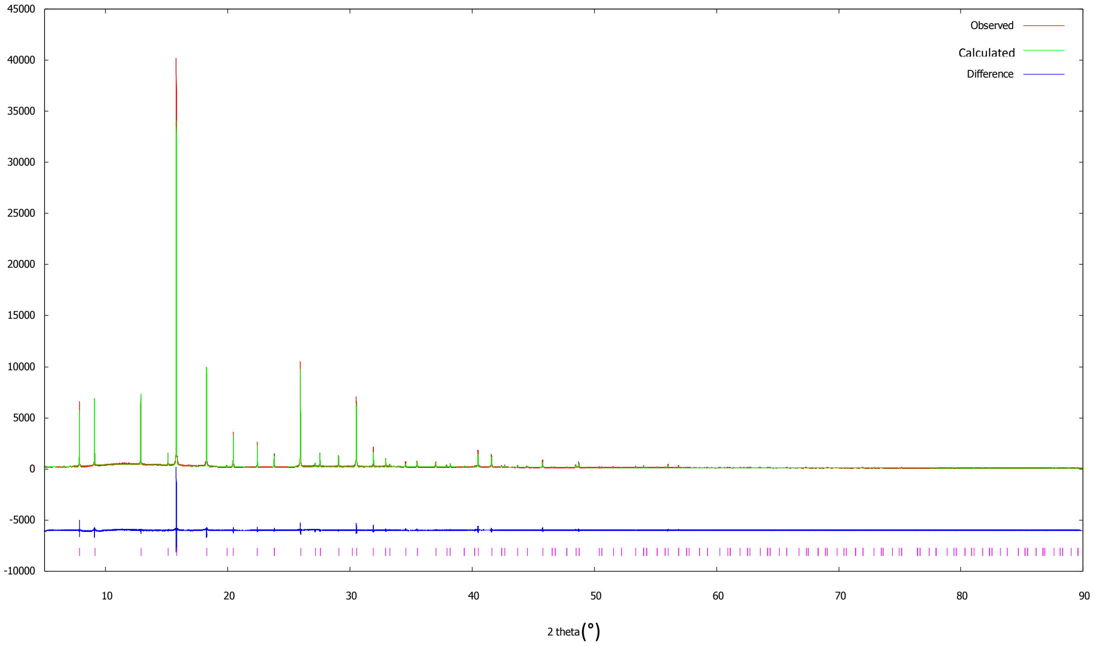

Figure 4. 3 - Pawley refinement of new Sn-Si-O phase using *Fm*-3m space group

HF digestion and subsequent ICP analysis performed by Warwick analytical service gave a composition of 35.79% Sn and 25.62% Si giving an estimated atomic ratio of 1:3 Sn:Si. Solid state NMR data was also obtained from the EPSRC National Solid-state NMR Service at Durham for both ^{29}Si and ^{119}Sn. ^{119}Sn NMR proved difficult. The interpretation provided indicated a very weak signal was located around -200 & -300ppm with a large chemical shift anisotropy suggesting a single Sn^{II} environment rather than a Sn^{IV} species, as this would show a chemical shift of ~-600ppm with less anisotropy. It should be noted, however, that the data quality is very poor and this interpretation is somewhat tenuous.

The ^{29}Si NMR signal, Figure 4.4, was collected using a recycle time of 60 seconds, spin-rate of 6000 Hz and a pulse duration of 6.4 µs. Whilst the signal is still reasonably broad indicating the material is not highly ordered, it can be resolved into 3 component peaks at -111.5 ppm, -101.7 ppm and -92.7 ppm, corresponding to Q_4, Q_3 and Q_2 tetrahedral silicon, respectively. The most intense peak is the Q_4 peak at -111.5ppm which indicates the majority of silicon in the framework is bound through oxygen atoms to four other silicon atoms. The abundance of Si-O-Si bonds would suggest either Sn atoms are clustered in a siliceous framework or the majority of the Sn atoms are in a different phase to the silica framework.

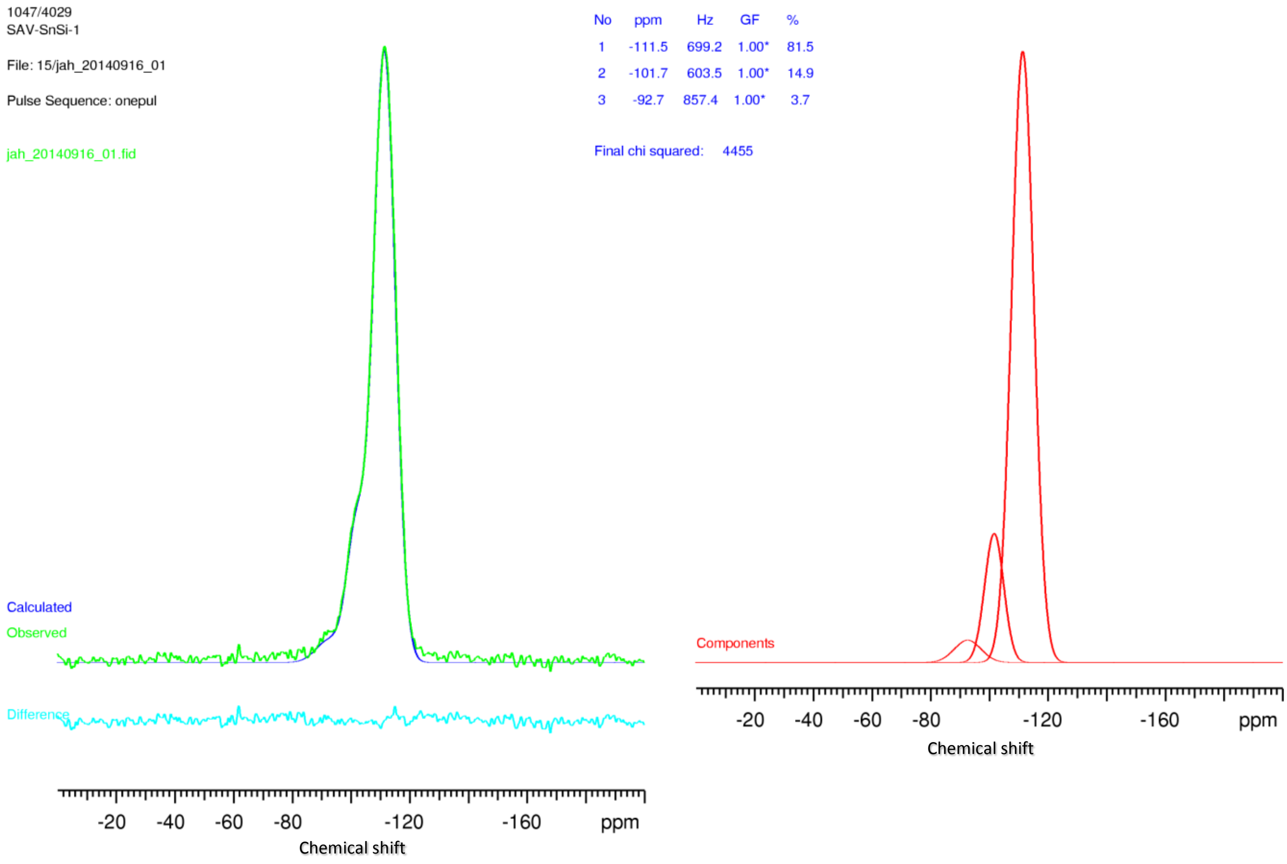

Figure 4. 4 - ^{29}Si NMR of unknown Sn-Si-O sample

Attempts to solve the structure have proceeded by three main routes:

Attempting to build manually an initial model by adding atoms to the Wyckoff positions of one of five possible space groups whilst maintaining the correct Si:Sn ratio and using a rough assumed volume per atom of ~18Å^3, which is a commonly used guideline for non-hydrogen atoms[92].

Generation of an initial model through charge flipping followed by simulated annealing using the Rietveld method.

Using the EXPO software which attempts to solve the structure using the biased random model generation method in direct space.

After the NMR data revealed the structure may have disorder, low temperature X-ray diffraction experiments were performed to try to reduce the thermal motion of the structure and thus reduce the degree of disorder.

An initial laboratory diffractometer scan at 100K revealed asymmetrical splitting of certain peaks: 002, 022, 004, 402, 422, 044, 622

Indexing the new pattern using EXPO, which uses TREOR90 to index, yielded the following cell with space group *I*2 a non-standard description of space group No. 5: a & c = 7.353 Å b = 10.300 Å   β = 91.466°.

However upon acquiring higher quality synchrotron data at 100 K from the I11 beamline at the Diamond Light Source, indexing yielded a new cell with primitive centring which allows for a more sensible transformation of the cell. A Pawley fit, Figure 4.5, was performed using this new data fitting to the new cell; $P4_2/n$ with $a = 7.2981(9)$ Å and $c = 10.5675(4)$ Å.

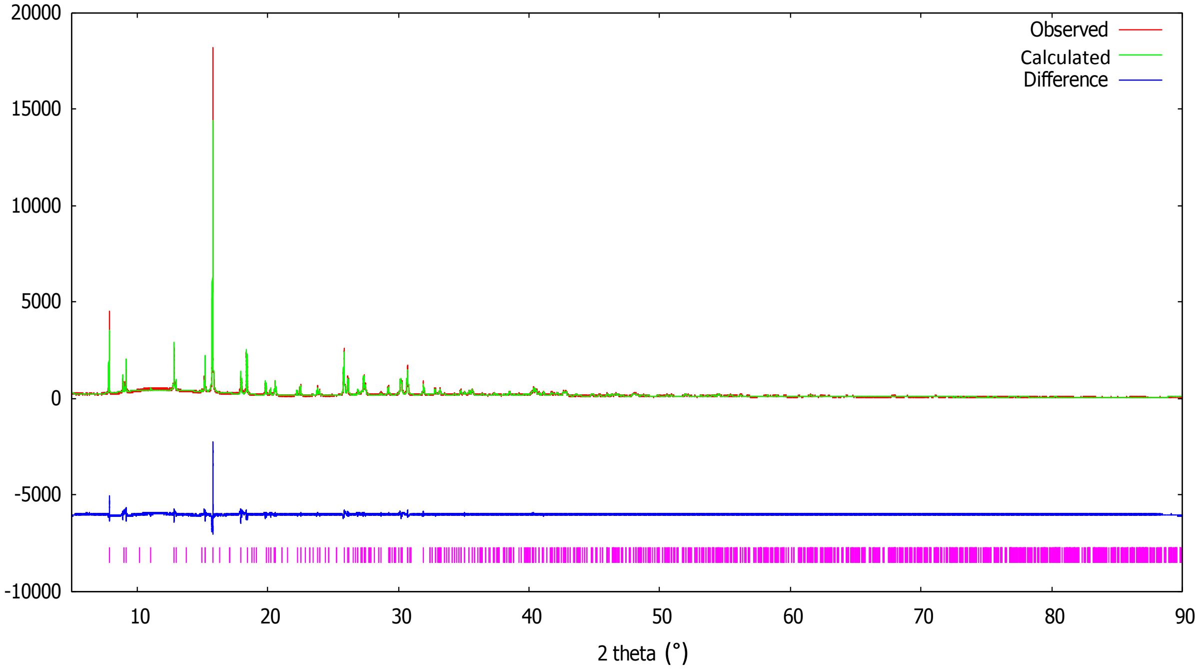

Figure 4. 5 - Pawley fit of Sn-Si-O sample at 100 K using synchrotron data

Thermal gravimetric analysis, Figure 4.6, of the sample under O_2/N_2 indicates mass loss over a wide temperature range but using the coupled mass spectrometer this can be broken down in to multiple steps. Loss of water is seen in two steps, from 30-80°C followed by 150-200°C. Water loss at lower temperature would likely be due to surface water on the sample, but higher temperature water loss would indicate the presence of structural water in the system. Loss of CO_2 indicates the presence of an organic compound as heating in O_2 should lead to complete combustion. As the synthesis of this material involves tin oxalate it is possible that the oxalate species is involved in the structure. XRF of the materials using a semi-quantitative method calibrated against standards, running each sample for 18 minutes, gave a composition of 42.44% O, 30.87% Sn, 29.27% Si and 1.83% Na. Based upon the elemental analysis by ICP-MS and XRF and TGA a possible composition would be $NaSn_3Si_9O_{25}\cdot0.5C_2O_4\cdot H_2O$ which maintains charge balance from oxalate with a small amount of sodium, which corresponds to approximately 1% by mass.

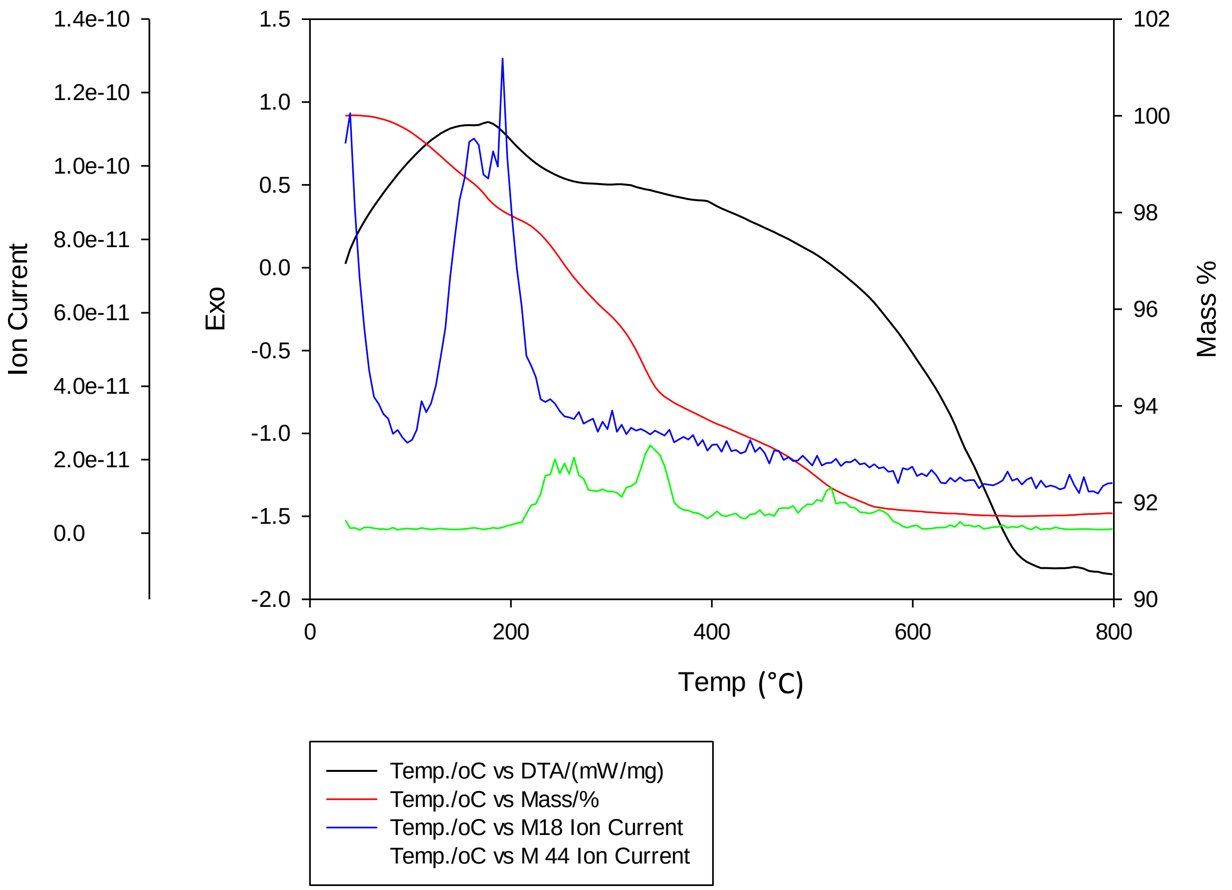

Figure 4. 6 - TGA plot with mass spectrometry signals of H_2O (blue) and CO_2 (green)

A range of information has been gathered about this material including some structural information from XRD and NMR together with compositional information from TGA/MS and ICP/MS, all of this information together should lead to the eventual solving of this structure but work is still on-going.

4.3-3 AV-7 - synthetic tin kostylvite

AV-7 is a stannosilicate material based upon the natural mineral Kostylvite first reported in a patent application by Corcoran[89] *et al.* for the Exxon group, but the structure was not solved until 2000 by Lin et al.[60] Due to the open hydrated framework containing both Na^+ and K^+ and structural similarity to K-umbite, a material shown to perform well as an ion-exchanger[49], this material was thought of as a potential ion exchange material itself.

AV-7 was synthesised according the literature with a change in the source of silica, with colloidal silica (Ludox HS-40) being used in place of sodium metasilicate due to availability and ease of preparation as it removes the need to dissolve the metasilicate during the preparation of the precursor gel. This change did not seem to affect the morphology of the sample when comparing SEM images.

4.3-4 Ion Exchanges

Following the successfully reproduced synthesis of AV-7, initial ion exchange experiments were performed. 1.00g of ground AV-7 was added to $25cm^3$ of $Sr(NO_3)_2$ solutions of varying concentrations and shaken for 24 hours, the resultant suspensions were filtered, washed well with deionized water and the solid formed into fused beads for XRF analysis as shown in Table 4.4.

Unfortunately XRF analysis for this material is not as accurate as possible due to problems with the sample preparation method. In forming a fused bead the material is heated to over 1000°C in the presence of a lithium borate flux in order to form a more diffuse and heterogeneous sample with a smooth surface. In this case the tin in the sample is oxidised to form SnO_2 which then forms an inclusion in the glass bead reducing the effectiveness of this technique. More routine sample preparations such as pressed pellets also proved to be inaccurate due to the heavy Sn atoms absorbing fluorescence from neighbouring lighter atoms.

Table 4. 4 - Compositions by percentage mass of solid samples derived from XRF

Material	Na	K	Sr	Sn	Si
Parent $NaKSnSi_3O_9$	7.3(1)	23.0(1)	0	24.00(6)	15.7(3)
0.01M	5.1(1)	22.9(1)	2.77(4)	24.72(6)	16.5(3)
0.05M	4.4(1)	13.9(1)	14.28(4)	19.68(6)	14.2(3)
0.5M	5.4(1)	13.4(1)	15.19(4)	18.95(6)	13.8(3)
1.0M	5.4(1)	12.6(1)	15.34(4)	17.42(6)	13.3(3)

Despite the lack of completely accurate results obtained from XRF, it is still evident from the data that some strontium is either being incorporated in to the material through ion exchange, adsorbing on the surface of the material or being precipitated out as an insoluble phase.

Through XRD no new phases were observed after ion exchange which would be due to a crystalline insoluble material and no higher background or areas of obvious amorphous material were observed, which would indicate the strontium has ion exchanged into the material.

SEM/EDX was performed to look for possible amorphous impurities; as seen below AV-7 can be seen form small cuboidal crystallites which tend to aggregate together in a flower-like cluster.

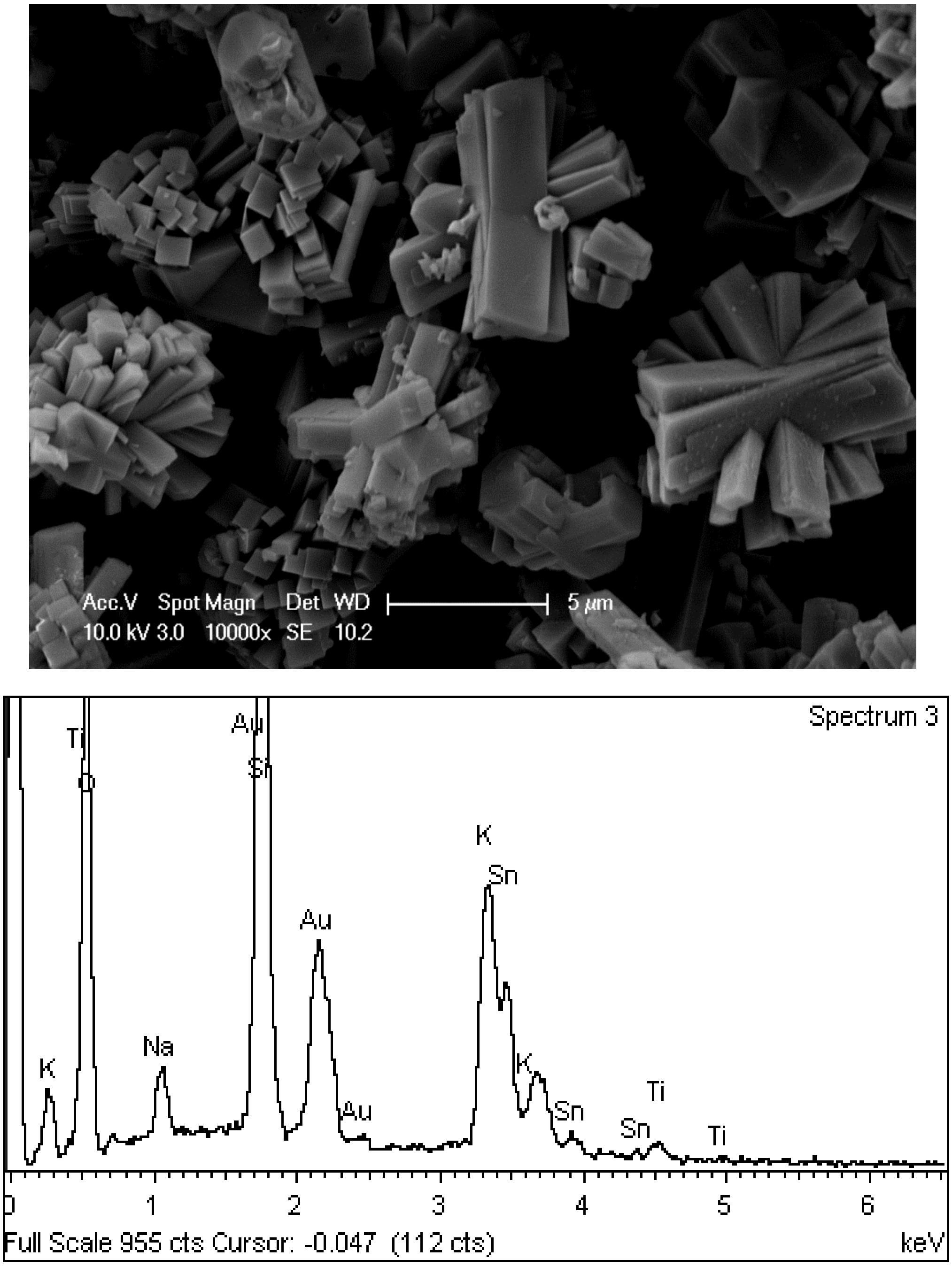

Figure 4. 7 - EDX (below) from above area of SEM (above) image with automatic peak assignment

SEM & EDX in Figure 4.7 indicates the presence of gold due to the conductive coating applied to the sample. The automatic assignment software also indicates the a large amount Ti due to the overlap of O. This amount of Ti is unlikely as an impurity would not have shown in up in the multiple scans of different regions of the sample. Unfortunately many of the elements present have emission lines which overlap, in this case it can be seen the potassium emission lines (Ka_1 3.31 keV, Ka_2 3.31 keV, Kb_1 3.59 keV) overlap with Sn (La_1 3.44 keV, La_2 3.43 keV, Lb_1 3.66 keV)

After ion exchange the sample appears to be mostly unchanged in terms of the morphology, with AV-7 remaining as aggregates of small cuboidal particles. EDX results cannot indicate the presence of strontium reliably due to overlap of Sr (La_1 – 1.81 keV, La_2 – 1.80 keV, Lb_1 – 1.87 keV) with Si (Ka_1 – 1.74 keV, Ka_2 -1.74 keV, Kb_1 1.84 keV)

Some large crystals can be observed in the SEM, and coupled with the reduction of the O peak for these it would imply this could be some residual NaF/KF which was not washed out from the material, F cannot be readily observed due to the only Ka1 emission being at 0.677 keV where there is only a small peak which would likely not correspond to the significant decrease of the O peak. However, there could be more F present than indicated due to the possible reabsorption of the low energy F emission by heavier elements present.

For every strontium atom being incorporated into the structure via an ion exchange mechanism, two corresponding sodium or potassium atoms must be removed to maintain charge balance. To observe this another ion exchange experiment was performed, this time at a much lower concentration level. 50 ppm $Sr(NO_3)_2$ solution was used for the experiment to simulate a more realistic level of strontium in a waste stream. To avoid the problems encountered with XRF and SEM/EDX, the ion exchange liquor was examined by ion chromatography, Figure 4.8, before and after ion exchange to examine the composition.

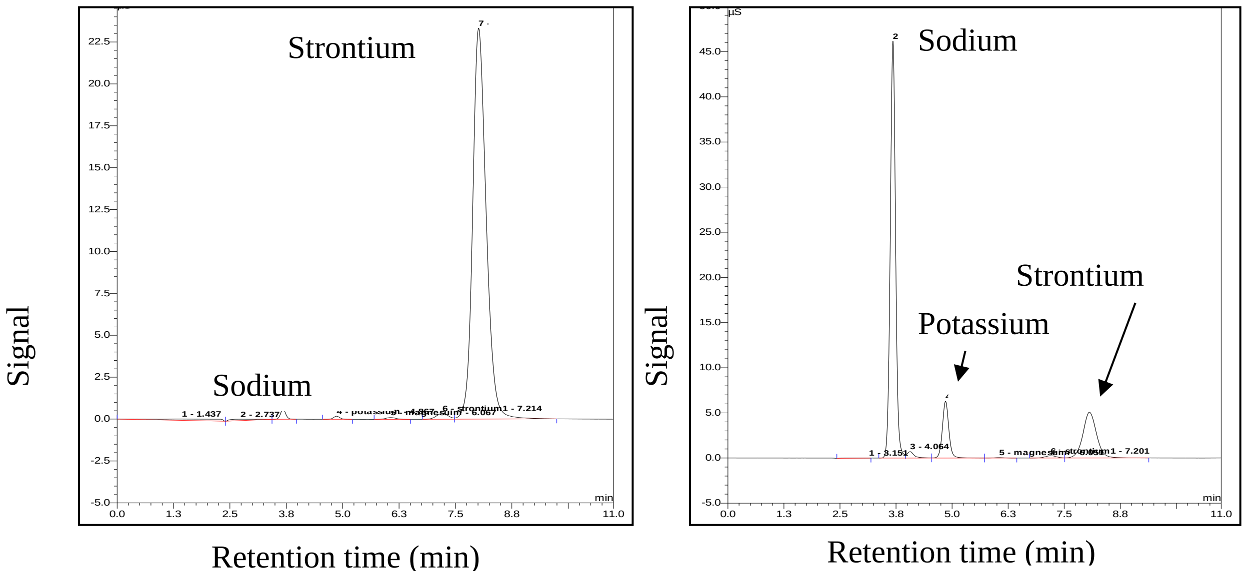

Figure 4.8 - Ion chromatogram of ion exchange solution before (left) and after (right) ion exchange with AV-7

The integrated intensities of the peaks, Table 4.5, directly correspond to the level of each ion in solution. It is evident the level of strontium is being significantly reduced and the sodium and potassium levels are indicative of an ion exchange reaction occurring. The K_d of the ion exchange shown in Figure 4.8 comes to ~1800.

Table 4. 5 - Integrated intensities and corresponding concentrations from ion chromatography

Peak Name	Before exchange		After Exchange	
	Integrated intensity (µS*min)	Concentration (ppm)	Integrated intensity (µS*min)	Concentration (ppm)
Sodium	0.11	0.56	6.36	45.22
Potassium	0.03	0.29	1.04	10.99
Strontium	8.11	49.52	1.78	10.77

Having shown AV-7 does ion-exchange strontium over a range of concentrations, from 1.0 mol dm^{-3} to 50 ppm, further detailed ion exchange studies will be described in chapter 5.

4.3-5 Structural characterization

4.3-5a Time of flight neutron diffraction

TOF Neutron diffraction data were collected for the AV-7 system and the exchanged equivalent. The data were calibrated using a NIST certified Si standard. Rietveld refinements (Tables 4.6-4.9 and Figures 4.9 & 4.10) were performed to obtain atomic positions and, in the case of the exchanged material, site occupancies. Refinement progressed by initially using structure reported by Lin *et al.*[37], fixing framework positions and refining cation positions before allowing all atomic positions to refine. Constraints were initially used to keep water molecules in position, along with occupancy constraints to ensure charge balancing of shared Na/K occupancy sites, however, these constraints were not applied to the final cycles of the refinement. In the case of Sr-exchanged AV-7 Sr positions and all cation occupancies were initially constrained to maintain charge balance and ensure Sr atoms remain in the pore; again these constraints were lifted for the final cycles of refinements. The data were collected at HRPD, ISIS running the samples for 10 hours and refined using TOPAS Academic 4.3 with a Chebyshev background function and a peak shape function for TOF neutron data contributed to the TOPAS Academic macro library by Professor W. I. F. David[93].

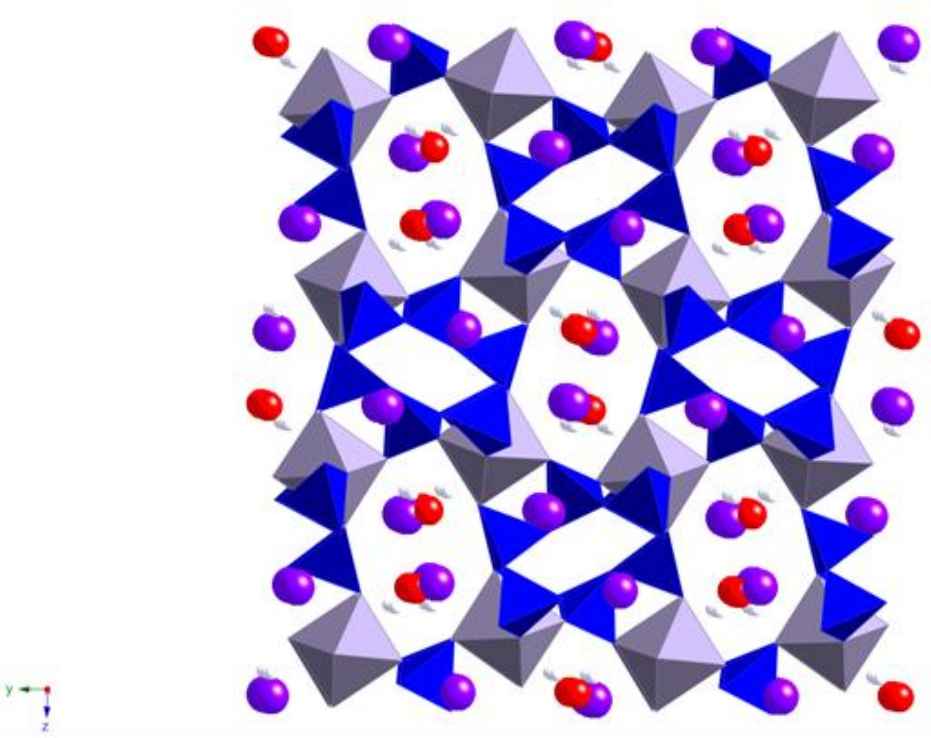

Figure 4. 9- Refined structure of AV-7 with grey SnO_6 octahedra, blue SiO_4 tetrahedra, purple K^+ spheres and red/white structural water

Table 4. 6 - Refinement parameters for AV-7

***a*(Å)**	6.47182(7)
***b* (Å)**	11.5540(1)
***c* (Å)**	12.9486(2)
V (Å^3)	935.07(2)
***β* (°)**	105.062(7)
space group	$P2_1/c$
Z	4
Nº independent parameters	82
R_{wp}	4.823
R_{exp}	1.602
R_p	4.224

Site	***x***	***y***	***z***	***occ***	B_{eq}
Sn1	0.1135(6)	0.7232(3)	0.2192(3)	1	0.56(5)
K1	0.685(1)	0.8796(7)	0.3918(6)	0.81(3)	1
Si1	0.8493(9)	0.4760(4)	0.1608(5)	1	0.23(4)
Si2	0.2014(8)	0.7361(4)	-0.0177(5)	1	0.23(4)
Si3	0.5851(9)	0.6996(5)	0.1581(4)	1	0.23(4)
Na1	0.792(1)	0.5473(8)	0.5908(6)	0.83 (6)	1
K2	0.839(6)	0.484(4)	0.593(3)	0.17(5)	1
O1	0.0650(6)	0.5508(4)	0.1916(3)	1	1.25(6)
O2	0.0522(7)	0.7635(4)	0.0609(3)	1	1.25(3)
O3	0.8022(6)	0.7660(3)	0.2077(4)	1	1.25(3)
O4	0.1863(7)	0.8930(4)	0.2467(4)	1	1.25(3)
O5	0.1544(7)	0.6822(4)	0.3771(4)	1	1.25(3)
O6	0.4374(7)	0.6910(4)	0.2383(4)	1	1.25(3)
O7	0.1551(7)	0.8992(4)	0.4450(4)	1	1.25(3)
O8	0.3652(7)	0.0600(5)	0.3723(4)	1	1.25(3)
O9	0.4548(7)	0.7489(4)	0.03972(4)	1	1.25(3)
O10	0.6041(6)	0.5137(2)	0.3896(5)	1	1.25(3)
D1	0.666(1)	0.4615(5)	0.3438(5)	1	4.62(9)
D2	0.541(1)	0.5761(5)	0.3381(5)	1	4.62(9)

Table 4. 7 - Refinement parameters for Sr-exchanged AV-7

***a*(Å)**	6.47000(5)
***b* (Å)**	11.5495(1)
***c* (Å)**	12.9458(7)
V (Å^3)	934.15(1)
***β* (°)**	105.0411(8)
space group	$P2_1/c$
Z	4
NO. independent parameters	85
R_{wp}	4.207
R_{exp}	1.657
R_p	3.071

Site	***x***	***y***	***z***	***occ***	**B_{eq}**
Sn1	0.1134(8)	0.7202(4)	0.2161(4)	1	0.43(7)
K1	0.746(5)	0.7528(2)	0.403(3)	0.25(1)	1
Sr1	0.691(2)	0.8842(9)	0.3924(9)	0.5(2)	1
Si1	0.8511(1)	0.4748(5)	0.1589(7)	1	0.50(6)
Si2	0.203(1)	0.7354(5)	-0.0180(6)	1	0.50(6)
Si3	0.584(1)	0.7011(4)	0.1577(5)	1	0.50(6)
Na1	0.688(9)	0.542(4)	0.650(4)	0.16(1)	1
K2	0.8443(5)	0.5370(4)	0.607(6)	0.239(8)	1
Sr2	0.776(5)	0.5458(2)	0.586(2)	0.30(8)	1
O1	0.0653(8)	0.5510(4)	0.1911(4)	1	1.37(4)
O2	0.0535(8)	0.7634(4)	0.0626(4)	1	1.37(4)
O3	0.8002(8)	0.7669(4)	0.2070(5)	1	1.37(4)
O4	0.1811(9)	0.8918(5)	0.2456(4)	1	1.37(4)
O5	0.1541(9)	0.6821(4)	0.3789(5)	1	1.37(4)
O6	0.4299(8)	0.6929(5)	0.2371(5)	1	1.37(4)
O7	0.1534(9)	0.9000(5)	0.4445(4)	1	1.37(4)
O8	0.3634(6)	0.0624(5)	0.3715(5)	1	1.37(4)
O9	0.4525(8)	0.7500(4)	0.03930(5)	1	1.37(4)
O10	0.6068(8)	0.5151(3)	0.3923(4)	1	1.37(4)
D1	0.6162(2)	0.4616(1)	0.3338(7)	1	4.78(9)
D2	0.530(2)	0.5754(1)	0.3349(8)	1	4.78(9)

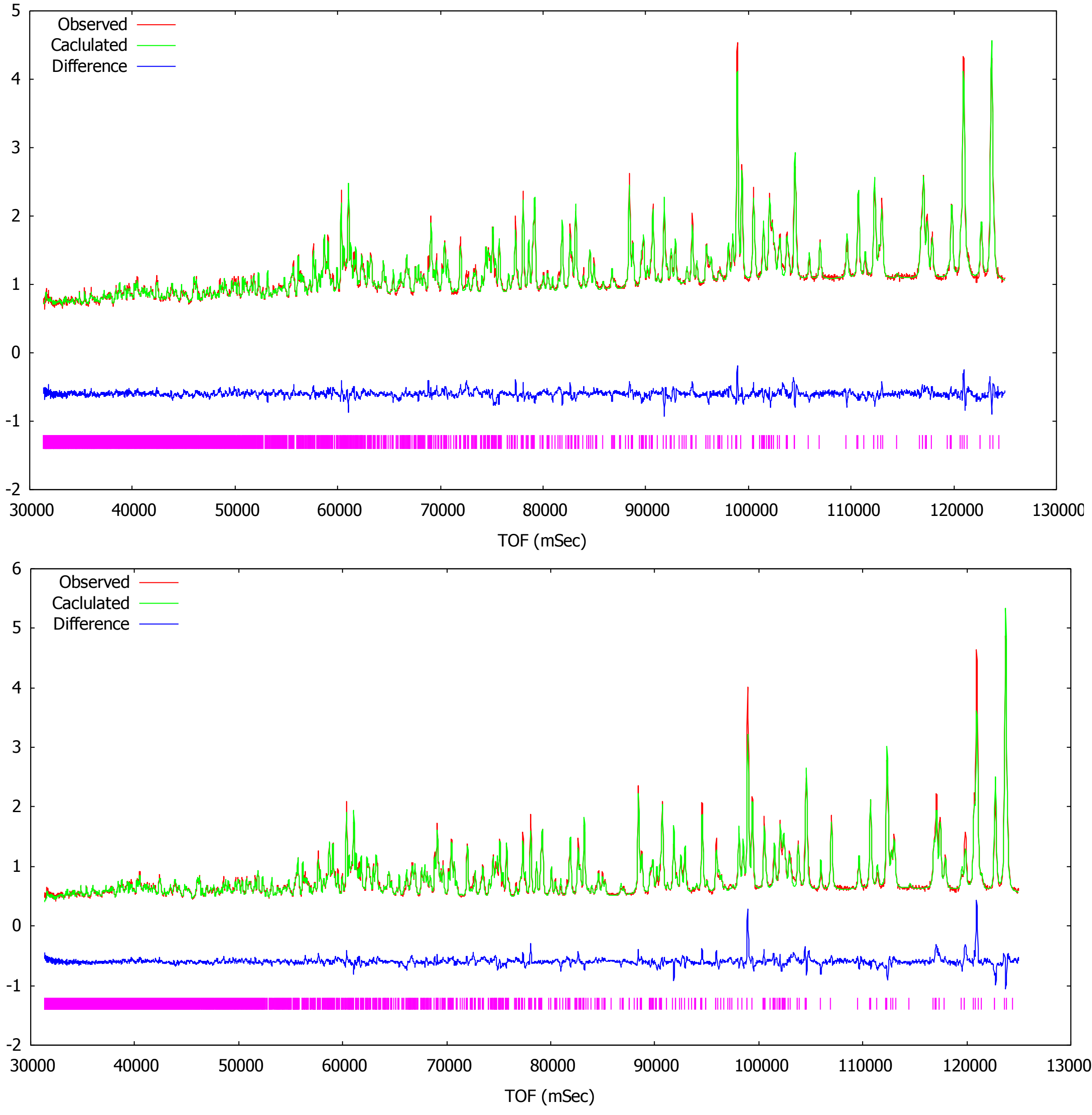

Figure 4. 10 - Observed, calculated and difference powder neutron diffraction pattern of AV-7 (top) and Sr-exchanged AV-7 (bottom)

Table 4. 8 - Refined bond distances and valence sums from neutron TOF diffraction of AV-7 and Sr-exchanged AV-7

AV7 bond distances						Sr-AV7 bond distances								
Bond	**Distance**	**Bond Valence**	**Bond**	**Distance**	**Valence**	**Bond**	**Distance**	**Valence**	**Bond**	**Distance**	**Valence**	**Bond**	**Distance**	**Valence**
Sn1_O1	1.971(5)	0.840	K1_O1	2.848(7)	0.126	Sn1_O1	1.991(5)	0.796	K1_O1	2.876(8)	0.117	Sr1_O1	2.876(8)	0.129
Sn1_O2	1.991(5)	0.797	K1_O2	3.190(8)	0.056	Sn1_O2	2.007(8)	0.762	K1_O2	3.234(4)	0.050	Sr1_O2	3.234(4)	0.049
Sn1_O3	2.015(5)	0.748	K1_O3	2.948(7)	0.099	Sn1_O3	2.045(3)	0.691	K1_O3	2.993(8)	0.089	Sr1_O3	2.993(8)	0.094
Sn1_O4	1.994(6)	0.791	K1_O4	3.169(7)	0.059	Sn1_O4	2.011(2)	0.756	K1_O4	3.222(2)	0.052	Sr1_O4	3.222(2)	0.051
Sn1_O5	1.988(5)	0.803	K1_O6	3.028(8)	0.082	Sn1_O5	2.021(3)	0.736	K1_O6	3.079(1)	0.073	Sr1_O6	3.079(5)	0.074
Sn1_O6	2.012(5)	0.754	K1_O7	2.907(8)	0.109	Sn1_O6	2.022(9)	0.733	K1_O7	2.925(9)	0.105	Sr1_O7	2.925(9)	0.113
	Sum	4.733	K1_O8	2.801(7)	0.141		Sum	4.472	K1_O8	2.833(8)	0.130	Sr1_O8	2.833(9)	0.144
Si1_O1	1.536(9)	1.226	K1_O9	2.99(7)	0.090	Si1_O1	1.557(6)	1.166	K1_O9	3.124(8)	0.082	Sr1_O9	3.124(8)	0.066
Si1_O4	1.545(6)	1.201		Sum	0.762	Si1_O4	1.573(3)	1.124		Sum	0.699	Sr1_O1	Sum	0.796
Si1_O7	1.598(6)	1.062				Si1_O7	1.606(3)	1.042						
Si1_O8	1.626(6)	0.995	K2_O1	2.857(3)	0.123	Si1_O8	1.652(5)	0.936	K2_O1	2. 876(9)	0.117		2.876(9)	0.129
	Sum	4.484	K2_O2	2.824(3)	0.133		Sum	4.269	K2_O2	2.860(9)	0.122	Sr2_O1	2.860(7)	0.134
Si2_O2	1.549(6)	1.190	K2_O3	2.584(6)	0.235	Si2_O2	1.557(2)	1.167	K2_O3	2.611(1)	0.220	Sr2_O2	2.611(1)	0.264
Si2_O5	1.577(6)	1.115	K2_O4	2.855(5)	0.124	Si2_O5	1.592(4)	1.076	K2_O4	2.871(1)	0.119	Sr2_O3	2.870(8)	0.131
Si2_O7	1.614(6)	1.023	K2_O5	2.592(3)	0.231	Si2_O7	1.641(6)	0.960	K2_O5	2.611(8)	0.220	Sr2_O4	2.611(7)	0.263
Si2_O9	1.594(6)	1.072	K2_O9	3.080(5)	0.073	Si2_O9	1.604(2)	1.047	K2_O9	3.128(1)	0.065	Sr2_O5	3.128(3)	0.065
	Sum	4.400	K2_O10	2.642(5)	0.205		Sum	4.250	K2_O10	2.552(4)	0.253	Sr2_O9	2.552(4)	0.309
Si3_O3	1.530(6)	1.243		Sum	1.123	Si3_O3	1.542(2)	1.209		Sum	1.117	Sr2_O10	Sum	1.295
Si3_O6	1.554(7)	1.176				Si3_O6	1.585(8)	1.093						
Si3_O8	1.624(6)	1.000				Si3_O8	1.646(7)	0.949						
Si3_O9	1.61(8)	1.033				Si3_O9	1.618(7)	1.012						
	Sum	4.452					Sum	4.262						

Table 4. 9 - Refined bond angles from neutron TOF diffraction of AV-7 and Sr-exchanged AV-7

AV7 Bond angles				Sr AV7 Bond angles			
O1_Sn1_O2	94.67(2)	O1_Si1_O4	116.3(4)	O1_Sn1_O2	95.103(1)	O1_Si1_O4	115.548(1)
O1_Sn1_O3	97.19(2)	O1_Si1_O7	109.06(3)	O1_Sn1_O3	97.269(1)	O1_Si1_O7	109.367(1)
O1_Sn1_O4	175.88(2)	O1_Si1_O8	111.07(3)	O1_Sn1_O4	175.817(1)	O1_Si1_O8	110.876(1)
O1_Sn1_O5	85.78(2)	O4_Si1_O7	108.96(3)	O1_Sn1_O5	85.638(1)	O4_Si1_O7	108.937(1)
O1_Sn1_O6	88.27(2)	O4_Si1_O8	106.47(3)	O1_Sn1_O6	88.318(1)	O4_Si1_O8	106.477(1)
O2_Sn1_O3	86.60(2)	O7_Si1_O8	104.25(3)	O2_Sn1_O3	86.931(1)	O7_Si1_O8	105.093(1)
O2_Sn1_O4	85.74(2)	O2_Si2_O5	114.11(3)	O2_Sn1_O4	85.575(1)	O2_Si2_O5	114.216(1)
O2_Sn1_O5	175.87(2)	O2_Si2_O7	105.94(3)	O2_Sn1_O5	176.436(1)	O2_Si2_O7	105.831(1)
O2_Sn1_O6	95.25(2)	O2_Si2_O9	113.48(4)	O2_Sn1_O6	94.936(1)	O2_Si2_O9	113.649(1)
O3_Sn1_O4	86.92(2)	O5_Si2_O7	109.05(3)	O3_Sn1_O4	86.886(1)	O5_Si2_O7	108.479(1)
O3_Sn1_O5	89.26(2)	O5_Si2_O9	106.98(3)	O3_Sn1_O5	89.517(1)	O5_Si2_O9	106.995(1)
O3_Sn1_O6	174.09(2)	O7_Si2_O9	107.02(3)	O3_Sn1_O6	173.941(1)	O7_Si2_O9	107.381(1)
O4_Sn1_O5	94.11(2)	O3_Si3_O6	111.86(3)	O4_Sn1_O5	93.939(1)	O3_Si3_O6	112.009(1)
O4_Sn1_O6	87.62(2)	O3_Si3_O8	111.11(3)	O4_Sn1_O6	87.511(1)	O3_Si3_O8	110.688(1)
O5_Sn1_O6	88.87(2)	O3_Si3_O9	112.03(3)	O5_Sn1_O6	88.568(1)	O3_Si3_O9	112.073(1)
		O6_Si3_O8	108.28(3)			O6_Si3_O8	107.753(1)
		O6_Si3_O9	112.04(3)			O6_Si3_O9	112.597(1)
		O8_Si3_O9	100.96(3)			O8_Si3_O9	101.112(1)

The structure described by the refinement, Figure 4.10, shows mostly good agreement with the structure described in literature with overall slightly decreased Sn-O bond distances, e.g Sn-O1 1.971(8) Å cf 2.084(8) Å. The Sn-O octahedron is also intact with a small deviation in bond angles, eg O1-Sn-O4 177.2(6) ° reported by Lin *et al.* with neutron refinement yielding the same angle as 175.88(2)°. Comparing the bond distances in Table 4.8 to the sum of the Shannon radii of the atoms would suggest many of the bond distances are too small. Sn-O and Si-O bonds would be 2.19 Å and 1.64 Å, respectively. The bond distances observed are all smaller, however, this is not an uncommon observation in these types of materials[49,60,90].

The K-O distance expected would be ~2.9 Å, however, sodium atoms also occupy the cation positions which would have an expected bond distance of ~2.56 Å. The average cation-oxygen bond distance in the cation sites in the unexchanged AV-7 are closer to the 2.9 Å K-O bond distance in the case of the K1 site and closer to the 2.56 Å Na-O bond distance in the case of the K2 site, this would suggest that the K2 cations sites are shared Na/K sites, which is also what is reported by Lin *et al.* [67]. After exchange there is not a significant change in the average cation-oxygen bond distances, but there is a slight decrease as seen by a decrease in the bond valence sum from 0.762 to 0.699 for the K1 site and 1.123 to 1.117 in the K2 site. As the Sr-O expected bond distance would be ~2.59 Å, any exchange would shift the average cation position closer to the framework decreasing the average bond distances.

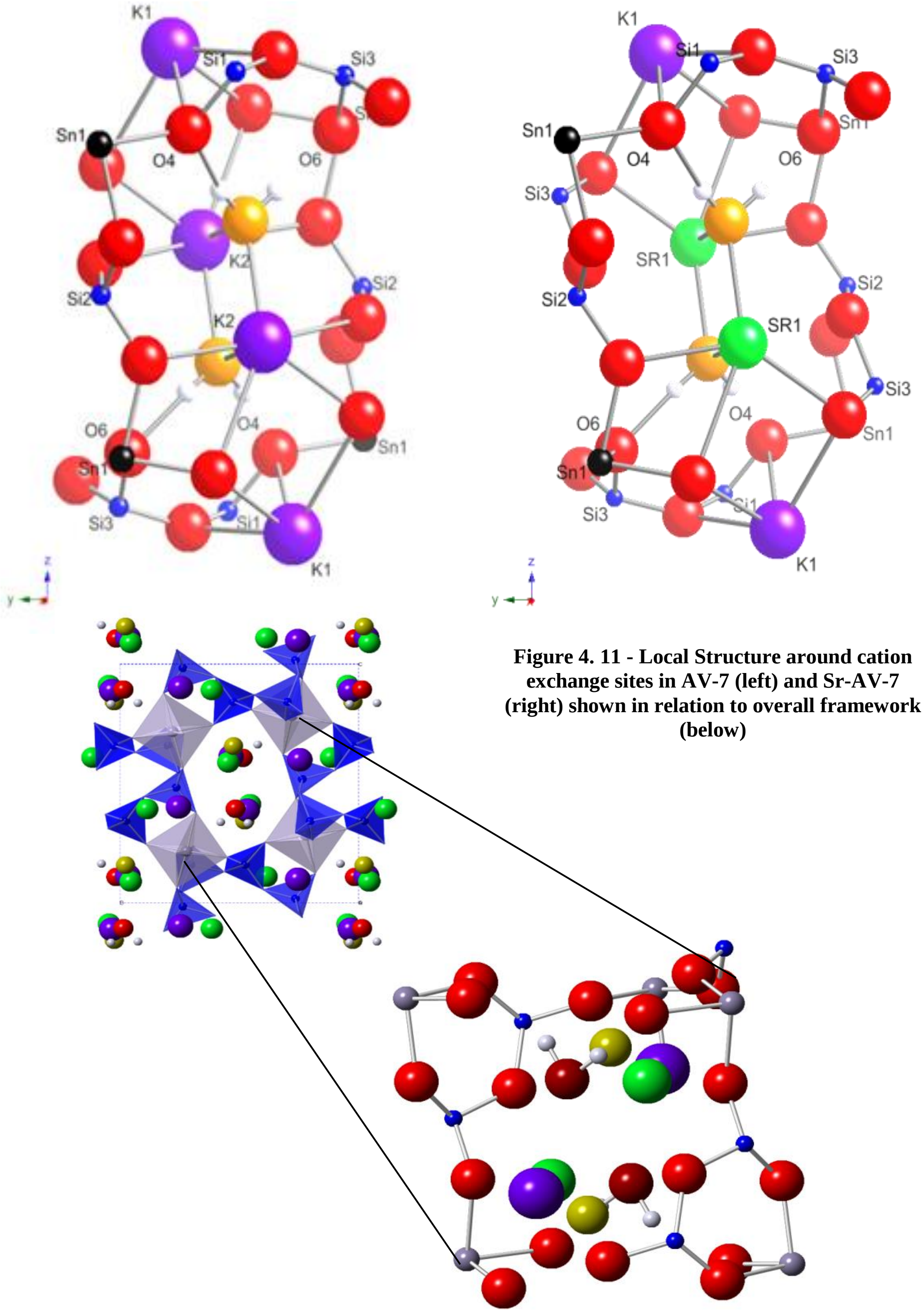

Figure 4. 11 - Local Structure around cation exchange sites in AV-7 (left) and Sr-AV-7 (right) shown in relation to overall framework (below)

Whilst the original paper describes cation sites as one site containing solely K^+ (K1) and a mixed occupancy site containing Na^+ and K^+ (K2), due to the similarity in the scattering cross sections of these elements in the case of neutrons, differentiation has proven difficult and for the sake of refinement only K^+ has been used initially, adding in Na atoms at a later date.

Upon exchange no great structural change is seen to occur, however an increase in the unit cell volume is seen, along with an increase in the Si-O bond distances as seen in Tables 4.8 & 4.9. Whilst Sr^{2+} has a smaller ionic radius than K^+, it is larger than Na^+ and an expansion of the unit cell would be expected if a large amount of Na^+ was replaced for Sr^{2+}.

Figure 4.11 shows the immediate environment around the exchanged cation environment and water molecules.

Water molecules (W1) in the pore can be seen to have oriented in a manner so as to favourably align the lone pairs with the cations and undergo hydrogen bonding with the surrounding framework. The deuterium atoms D1 & D2 are within 1.8 Å from O4 and O6 respectively, as shown in Figure 4.11, indicating likely H-bonds. Upon exchange the angle between the neighbouring cations and water molecule increases from 97.21(8) ° to 99.13(7) °. This is likely due to the higher charge density of Sr^{2+} in comparison to Na^+ and K^+.

From the diffraction data it can be inferred Sr^{2+} exchanges into both sites with a slight preference for the K2 site. This preference can be rationalized using bond valence calculations, shown in Tables 4.8 & 4.9, which also indicate the larger, more accessible K2 site to be the preferred ion exchange site.

4.3-5b Temperature stability and variable temperature X-ray diffraction

According to Lin *et al.* [62] AV-7 can be thermally decomposed to a rhombohedral phase known as AV-11. To examine this expected phase transition TGA and variable temperature lab X-ray diffraction data were collected along on AV-7 and Sr-exchanged AV-7. High quality synchrotron data from the I-11 beamline at the Diamond Light Source were also collected on thermally treated samples of Sr-exchanged AV-7. Thermal gravimetric analysis of both pristine and exchanged AV-7, shown in Figure 4.12, appears to indicate a difference in the loss of structural water. A mass loss of ~4.8% over a temperature range between 30 and 800°C for AV-7, which agrees with that reported by Lin and co-workers, beginning at ~ 200°C is seen to be more gradual with a more intense negative signal from the differential thermal analysis (DTA) indicating a more endothermic process. In the case of the Sr-exchanged AV-7 the mass loss is more rapid and the DTA peak less intense suggesting less tightly bound structural water.

Upon ion exchanging sodium for strontium, some of the pores will be less occupied due to removing two sodium atoms which are replaced by one strontium to maintain charge balance and creating pores with less cations. Removing the lone-pair interaction between the cation and water molecule could result in less tightly bound water and explain the trend observed in the TGA. Exchanging one Sr^{2+} cation in to the structure per two Na^{+} cations would result in a higher void volume in the pores of the structure and thus water in these empty pores would be less strongly bound, which agrees with the observation of water being removed slightly more easily after strontium ion-exchange.

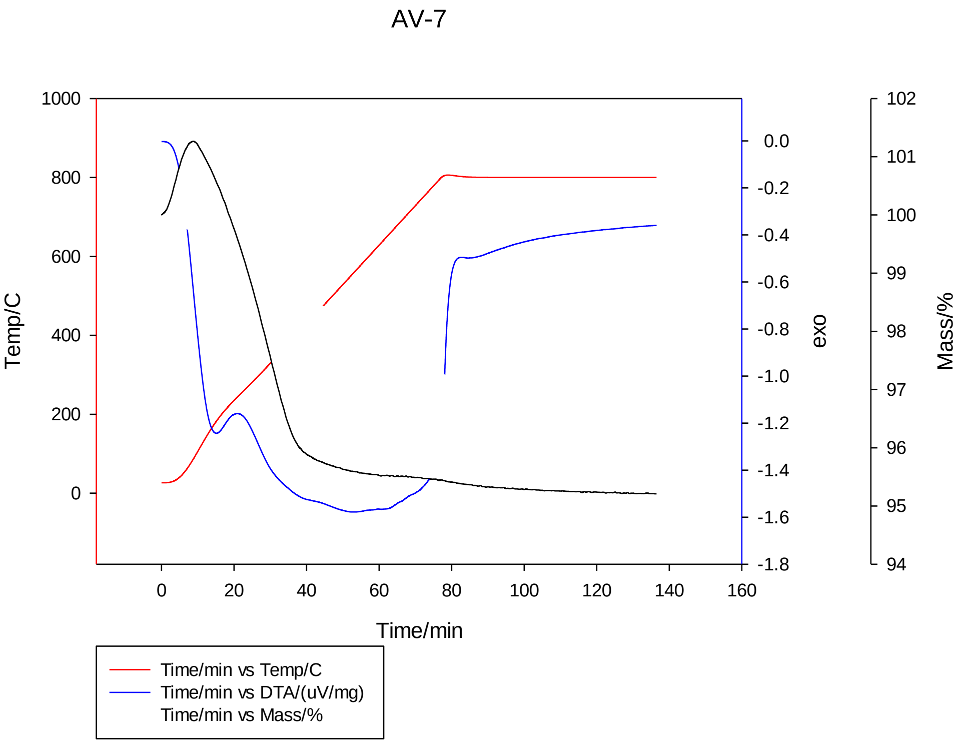

AV-7

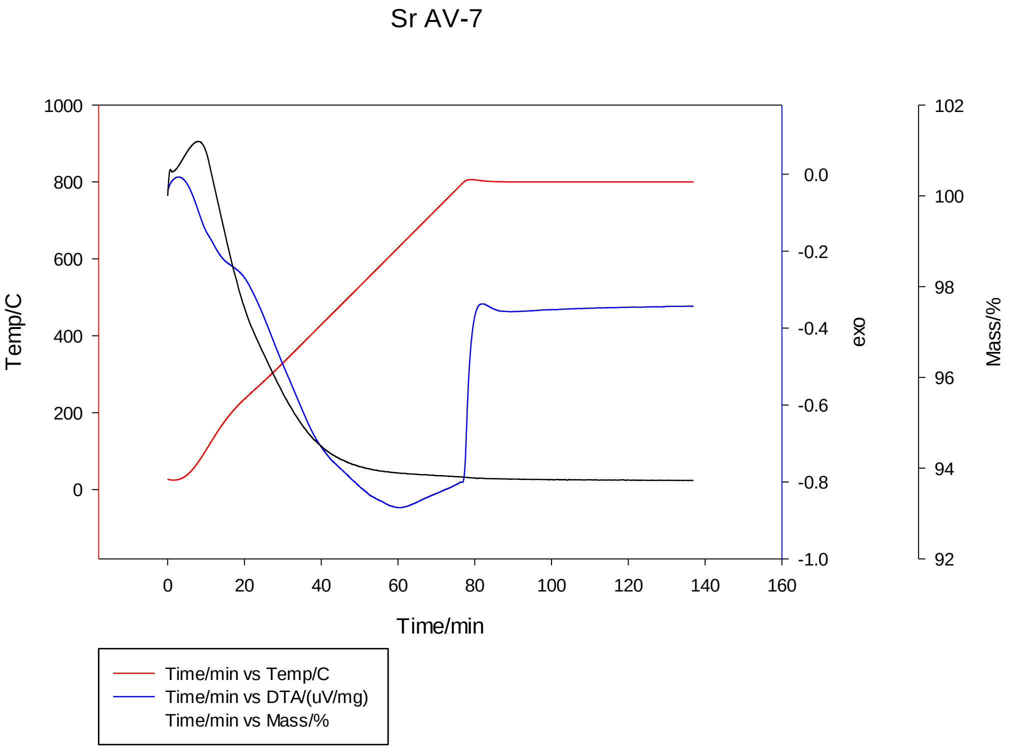

Sr AV-7

Figure 4. 12 - TGA trace of AV-7 (top) & Sr- exchanged AV-7 (bottom) heated under N2

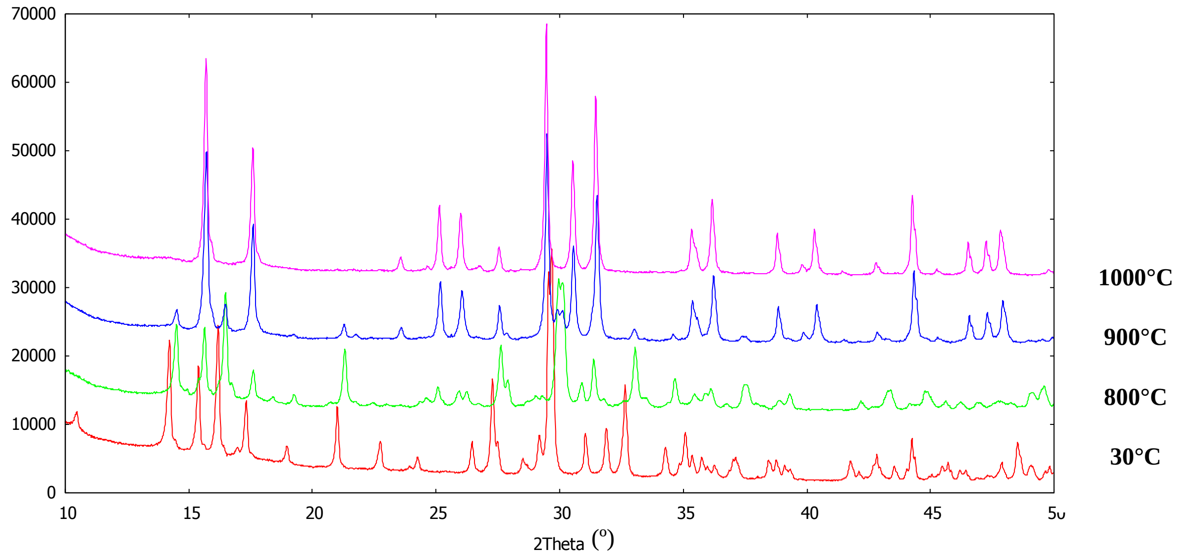

Figure 4. 13 - Variable temperature PXRD of AV-7

Upon heating in air AV-7 does appear to undergo the phase change to AV-11, Figure 4.16, *R3h* ($NaK_3SnSi_6O_{18}$ [90]) via a dehydrated intermediate, based on indexing data collected from lab X-ray diffractometers. Upon refining I11 data of the material collected ex-situ, Figure 4.13 and Table 4.10, a good fit was difficult to obtain and upon closer inspection it is evident there are some cases of peak splitting throughout the pattern as shown in Figure 4.15 where the (104) peak is split. This would indicate the structure may in fact be slightly deformed to be monoclinic rather than rhombohedral.

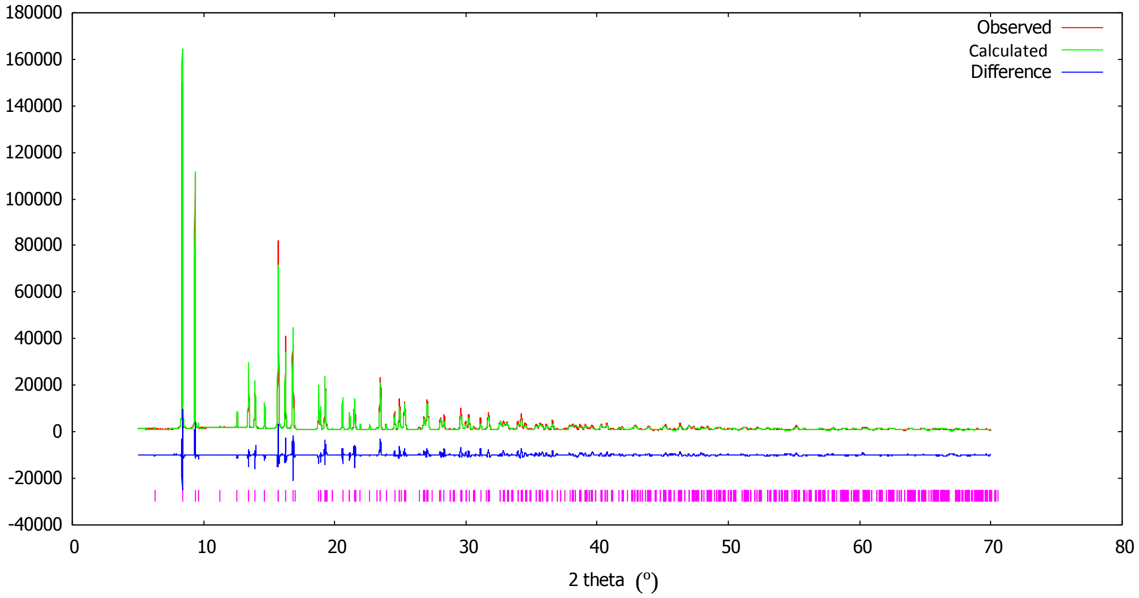

Figure 4. 14 - Synchrotron PXRD data collected on AV-7 heated to 1100°C.

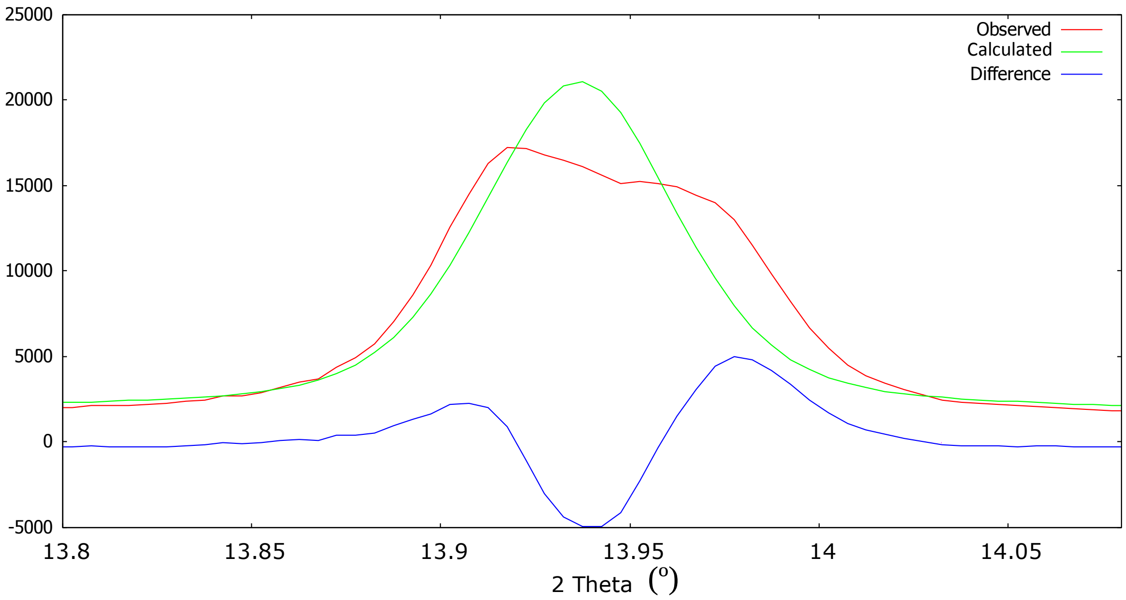

Figure 4. 15 - Observed peak splitting from I11 data collection on heated AV-7

Table 4. 10 - Refinement information for synchrotron data collection of heated AV-7

a **(Å)**	10.120(2)	***Z***	9
b **(Å)**	10.117(1)	**N°. independent parameters**	104
c **(Å)**	14.768(2)	R_{wp}	12.347
α **(°)**	90	R_{exp}	1.126
β **(°)**	90	R_p	9.146
γ **(°)**	120		
V(Å^3)	1309.45(4)		
Space group	*R*3H		

Site	*x*	*y*	*z*	*Occ*	B_{eq}
Sn1	2/3	1/3	0.089(2)	1	1.188(1)
Sn2	0	0	0.237(2)	1/3	1.72(4)
Si1	0.340(1)	0.067(1)	0.1813(9)	1	1.297(9)
Si2	0.0039(2)	0.452(1)	0.015(2)	1	1.215(1)
K1	1/3	2/3	0.180(1)	1.018(8)	1
K2	0.440(1)	0.333(1)	0.352(1)	0.602(1)	1
Na1	1/3	2/3	0.179(2)	1.031(8)	1
Na2	0.430(1)	0.267(1)	0.412(2)	0.490(3)	1
O1	0.101(3)	0.171(1)	0.321(1)	1	1.518(2)
O2	0.739(2)	0.437(1)	0.164(2)	1	1.839(2)
O3	0.267(3)	0.467(2)	0.342(2)	1	1.485(4)
O4	-0.008(3)	0.344(2)	0.387(1)	1	1.152(4)
O5	0.296(2)	-0.098(2)	0.237(2)	1	1.212(3)
O6	0.204(1)	0.075(2)	0.163(1)	1	1.116(5)

Table 4. 11 - Refined bond distances of heated AV-7 phase

Bond	**Distance(Å)**	**Bond**	Distance(Å)
Sn1 - O2	2.0456(3)	**K1 - O4**	2.750(3)
Sn1 - O3	2.0788(2)	**K1 - O1**	2.868(4)
Sn2 - O6	2.0311(1)	**K2 - O1**	2.771(2)
Sn2 - O1	2.0354(2)	**K2 - O3**	2.773(4)
		K2 - O6	2.798(5)
Si1 - O5	1.598(3)	**K2 - O5**	2.825(2)
Si1 - O6	1.603(3)	**K2 - O5**	3.049(2)
Si1 - O2	1.6145(4)		
Si1 - O4	1.6212(2)		
Si2 - O3	1.596(2)		
Si2 - O1	1.610(3)		
Si2 - O5	1.631(2)		
Si2 - O4	1.639(4)		

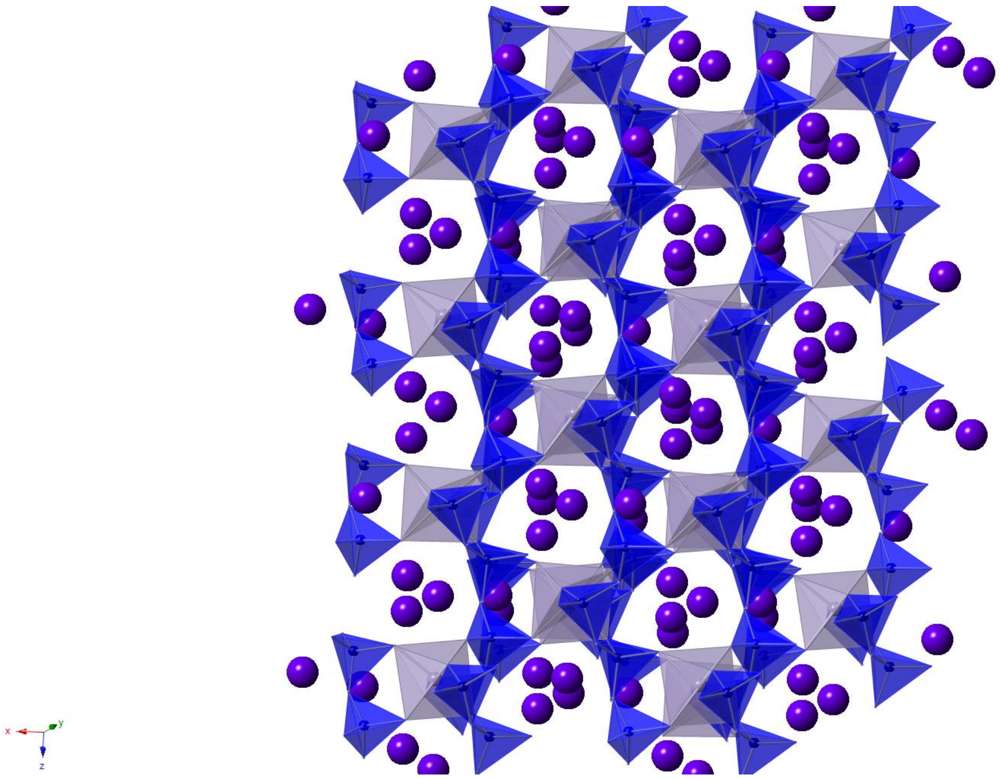

Figure 4. 16- Refined Structure of heated AV-7 phase with grey SnO_6 octahedra, blue SiO_4 tetrahedra and purple K^+ spheres

This more dense form could potentially be used as a waste form as the smaller pores which contain no water molecules may be able to lock in exchanged cations and prevent back exchange. In order to examine the suitability for this material as a waste form AV-7 was Sr-exchanged with 1.0 mol dm^{-3} $Sr(NO_3)_2$ for 24 hours then loaded into a can for hot isostatic pressing. The can was then cut into slices and the steel dissolved resulting in slices of a dense ceramic monolith. A standard method, MCC-ASTM, was then used to measure the leaching rates of the new material which will be discussed in Chapter 5.

4.4 Conclusions

Brief investigations into preparing new stannosilicate materials have been performed with one new material prepared and the structure solution underway. The synthesis of tin silicates can be challenging due to the harsh conditions necessary to prevent formation of the stable SnO_2 phase. Tin kostylvite has been prepared as per in literature and the structural changes upon strontium ion exchange and heating investigated, using laboratory X-ray powder diffraction and neutron powder diffraction. Neutron powder diffraction shows water molecules in the large pore of the structure coordinating with both the framework and cations within the pore, possibly allowing for extra stabilisation of the cations.

Chapter 5: Ion exchange

5.1 Introduction

This chapter describes in detail more extensive ion exchange studies of the materials discussed previously; the initial studies in Chapters 3 and 4 were performed using higher concentrations to screen for potential ion exchange and to examine the maximum uptake of materials and were based on X-ray fluorescence analysis. Following successful higher concentration ion exchange, low level (1-100 ppm) exchanges were performed and monitored using ion chromatography, which also allows for monitoring the increase in solution of the cations exchanged out of the framework in addition to the uptake of the target cations. Finally the lowest level exchanges, which are at more realistic concentrations for nuclear waste streams, were monitored using exchange solutions containing ^{85}Sr measured using scintillation counting of the emitted gamma rays. Calcium and caesium were chosen as competing cations amongst others, as calcium is known to compete for exchange sites with strontium due to their similarity in size and charge and caesium is commonly found in the same effluent streams along with strontium.

AV-3 and AV-7 were compared with a range of materials over high concentration: a small pore zeolite ETS-4 ($Na_9Si_{12}Ti_5O_{38}(OH)\cdot xH_2O$), a natural mineral clinoptilolite used in SIXEP, and $NaZrSi_2O_7$, a material studied for its ion exchange properties during a related 4th year MSci project. Also included is a sample of AV-7 heated to 1050°C until transformed to a more condensed rhombohedral structure, AV-11.

5.2 Experimental

5.2-1 AV-7 Competitive strontium ion exchange

1.0g of AV-7 solid was added to 20cm^3 of:

a) 0.5 mol dm^{-3} $Sr(NO_3)_2$ solution;

b) 0.5 mol dm^{-3} $Sr(NO_3)_2$ with 0.5 mol dm^{-3} $Ca(NO_3)_2$ solution; or

c) 0.5 mol dm^{-3} $Sr(NO_3)_2$ with 0.5 mol dm^{-3} $CsNO_3$ solution.

Solutions were shaken overnight for 24 hours before using centrifugation to separate the solid. The solid was then washed twice with portions of deionised water then centrifuged again. The washed solid was then formed into fused beads using the method described in Chapter 2 for XRF analysis.

5.2-2 Ion Chromatography

In order to calibrate the ion chromatography column certified standard solutions were purchased from Fisher of 1000ppm for each element to be analysed. From these standard solutions were made 8 solutions of varying concentrations which were run in triplicate after flushing the system with water filtered through a millipore water filtration system. Plotting the integrated peak intensities vs the concentration gave a linear fit and allowed for calibration using the equation of the line from a linear regression, Figure 5.1 and Table 5.1.

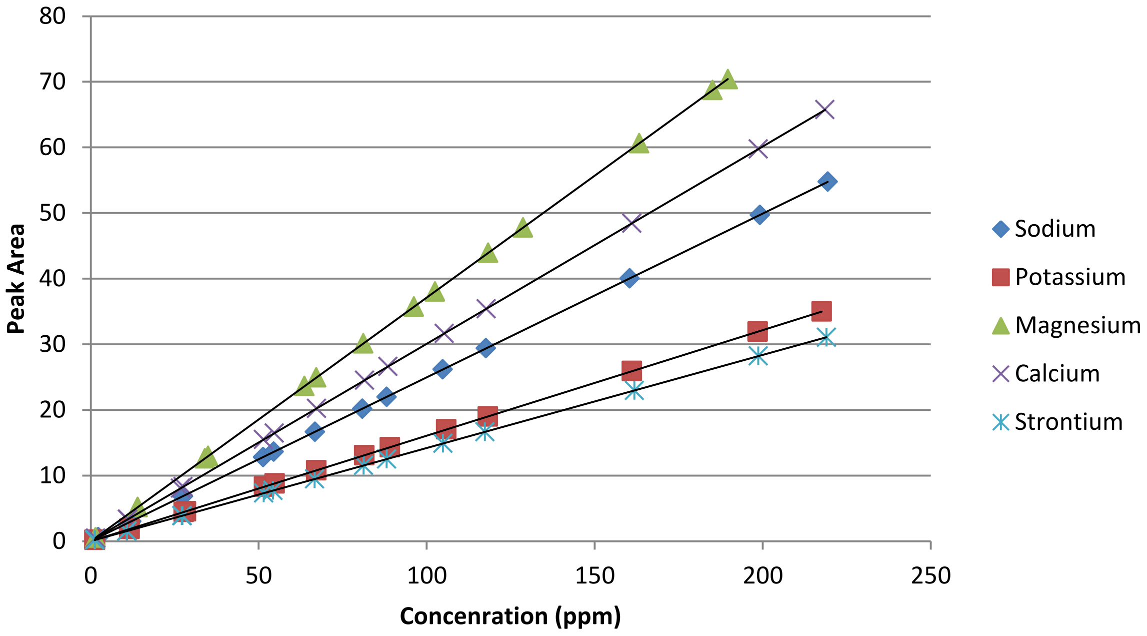

Figure 5. 1 - Calibration curves for ion chromatography column (error bars too small to be seen)

Table 5. 1 – Linear fits for ion chromatography calibrations

Calibration standard	Linear Fit
Sodium	y=0.2496x+7e-15
Potassium	y=0.1608x-7e-15
Magnesium	y=0.3711x
Calcium	y=0.1419x+3e-15
Strontium	y=0.3007x

0.2 g of each ion exchange material was added to 100 ppm solutions of $Sr(NO_3)_2$ to examine low level ion exchange properties, chromatograms of the ion exchange solution before and after ion exchange allowed for monitoring of both uptake and release of cations.

5.2-3 Initial ^{85}Sr exchanges

1.00 g of each ion exchange material was batch exchanged with 10 cm^3 of a 0.5 mol dm^{-3} solution of $Sr(NO_3)_2$ doped with ^{85}Sr over 24 hours. The $Sr(NO_3)_2$ solution was prepared by dissolving 10.582 g $Sr(NO_3)_2$ in 100 cm^3 of deionized water followed by the addition of ~15

MBq of ^{85}Sr in the form of $SrCl_2$ in water. The solid was separated from the supernatant, washed with water and dried for analysis using a Ge crystal scintillation counter.

5.2-4 Trace ^{85}Sr ion exchanges pH 7 & 4

Following initial ion exchanges a second and third batch of experiments were performed to look at exchange over a range of materials over four sets of conditions.

0.05 g of each ion exchanger was added to 10 cm^3 of solution as listed in table 5.2. The suspensions were shaken overnight for 24 hours before centrifuging to separate the solid and supernatant fluid. The supernatant was collected and the solid washed with deionised water before centrifuging again. Both the solid and supernatant fluid were counted using a Ge-based liquid nitrogen cooled scintillation counter to measure the activity. The integrated intensities of the peaks generated by the MAESTRO software were used for the activity of ^{85}Sr in each solution as there should be a linear relationship between the two and only relative numbers rather than absolute are necessary.

Table 5. 2 - Composition of ion exchange liquors - ^{85}Sr concentration given in MBq due to a very low chemical concentration

	$^{85}SrCl_2$	$Sr(NO_3)_2$	KNO_3	$NaNO_3$	$Mg(NO_3)_2$	$Ca(NO_3)_2$	$CsNO_3$	HCl	pH
Sr pH 4	0.22 MBq (<1 ppb)	10 ppm						~5µl	4.1
Competitive pH 7	0.22 MBq (<1 ppb)	10 ppm	10 ppm	100 ppm	20 ppm	20 ppm	10 ppm		6.9
Sr pH 7	0.22 MBq (<1 ppb)	10 ppm							6.8
Competitive pH 4	0.22 MBq (<1 ppb)	10 ppm	10 ppm	100 ppm	20 ppm	20 ppm	10 ppm	~5µl	3.9

5.2-5 Trace ^{85}Sr ion exchanges pH 10-11

0.01g of ion exchange material was added to a centrifuge tube followed by the addition of 10 cm^3 of ion exchange solution A, B, C or D which had the compositions shown in Table 5.3. When adding strontium to each of the solutions, non-radioactive strontium was added first to each of the solutions so the addition of equal portions of ^{85}Sr to each solution brings the total strontium concentration up to the value tabulated. Samples were prepared in triplicate for a total of 12 ion exchanger-solution samples for each examined ion exchange material. These ion exchanges were left to shake overnight for 24 hours before using centrifugation to separate the solids from the liquids.

Table 5. 3 - Composition of ion exchange solutions A-D in ppm

Solution	**A**	**B**	**C**	**D**
pH	11.2	11	10	10
Cs (ppm)	9.06×10^{-4}	0.362	0.302	1.51
^{85}Sr + Sr (ppm)	1.51×10^{-5}	1.53×10^{-3}	5.67×10^{-3}	3.21×10^{-2}
Na (ppm)	70	130	60	210
K (ppm)	0.2	10	20	250
Ca (ppm)	0.2	3	1.2	60
Mg (ppm)	0.1	3	140	30

In order to counter previously encountered problems during the pH 7 & 4 ^{85}Sr exchanges, where activity from all samples in the room resulted in a high background count, the method for this batch of exchanges was modified. A new detector was purchased to allow us to modify the instrument set-up more freely. The new detector uses a NaI scintillation crystal rather than pure-Ge, which whilst less efficient does not require liquid nitrogen cooling. In addition large amounts of lead flashing were used as shielding around both the detector and other samples in the area to reduce the background counts by a factor of 10. In order to utilize the activity of both the solid and liquid elements of the samples, solutions of known activity were used to calibrate the detector. In the case of calibrating for the liquid samples aliquots of known ^{85}Sr activity were added to 10cm^3 and for calibrating the solid samples, aliquots between 20 and 200 µl of higher activity ^{85}Sr were pipetted into the bottom of the centrifuge tubes used for measuring, to better simulate the activity from a point source.

5.3 Results and discussion

5.3-1 AV-7 Competitive strontium ion exchange

Initially the main focus of the project was the investigation of the ion exchange properties of AV-7 ($NaKSnSi_3O_9 \cdot H_2O$), a synthetic tin form of the natural zirconosilicate kostelyvite, reported by Lin *et al.* [60]. Preliminary ion-exchange results are described in Chapter 3, which were followed by a brief investigation into the competitive strontium exchange.

Table 5. 4 - Mole ratio compositions of solid AV-7 after ion exchange, XRF data normalized on Sn content

	Sn	Si	Na	K	Cs	Sr
Unexchanged $NaKSnSi_3O_9$	1.00(4)	2.8(2)	1.6(3)	2.91(4)	0.00	0.00
0.5M Sr^{2+} with 0.5M Ca^{2+}	1.00(4)	3.2(2)	1.2(3)	2.18(4)	0.00	0.38(3)
0.5M Sr^{2+} with 0.5M Cs^+	1.00(4)	3.3(2)	1.1(3)	2.13(4)	0.07(5)	0.94(3)
0.5M Sr^{2+} with 0.5M Ca^{2+} & 0.5M Cs^+	1.00(4)	3.3(2)	1.7(3)	2.16(4)	0.08(5)	0.31(3)
0.5M Sr^{2+} only	1.00(4)	2.7(2)	1.1(3)	1.58(4)	0.00	0.80(3)

The measurements were taken by forming a fused bead using the method described earlier in Chapter 2, whereby the solids remaining after ion exchange reactions are filtered, washed and dried before being heated to 1050°C in a lithium borate glass to form a homogenous glass bead. The XRF measurement method used a calibrated method with a number of fused beads of standard composition to analyse only Sn, Si, Na, K, Cs and Sr and thus any Ca which would have been exchanged into the material is not visible. A limitation to this method is the time-consuming nature of the sample preparation and time taken to calibrate the instrument as any element not included in the initial calibration will not be measured. In addition to a missing element, in this case calcium, not being measured, due to the matrix effect equation as discussed in Chapter 2, if calcium forms a significant missing mass fraction then the attempt of the spectrometer software to assign a mass fraction based upon the observed fluorescence will be incorrect, however, this effect is usually minimal unless the missing element forms a substantial fraction of the sample. Some strontium exchange is noticeable despite the presence of Ca^{2+} and Cs^{+}, with Ca^{2+} affecting uptake more than Cs^{+}. Whilst sensitivity to Ca^{2+} is not desired, it is not surprising as strontium and calcium are challenging to separate. However, the apparent preference of strontium over caesium is a useful feature as many of the ion exchangers in use such as Nb-CST and clinoptilolite are selective for caesium over strontium.

5.3-2 Ion Chromatography

Ion chromatography was used initially to measure the Sr^{2+} concentrations of the ion exchange solution before and after ion exchange. As shown in Figure 5.2, this allows for a comparison of AV-3 and AV-7 with clinoptilolite, a zeolite known to have good ion exchange behaviour and titanite, a previously prepared material which may have potential ion exchange behaviour. These measurements were performed for some initial results to test the viability of the ion chromatography because of the rapid throughput available as opposed to using another technique such as inductively coupled plasma optical emission spectrophotometry (ICP-OES) or atomic absorption spectrometry which would have required a long waiting time for a high number of samples.

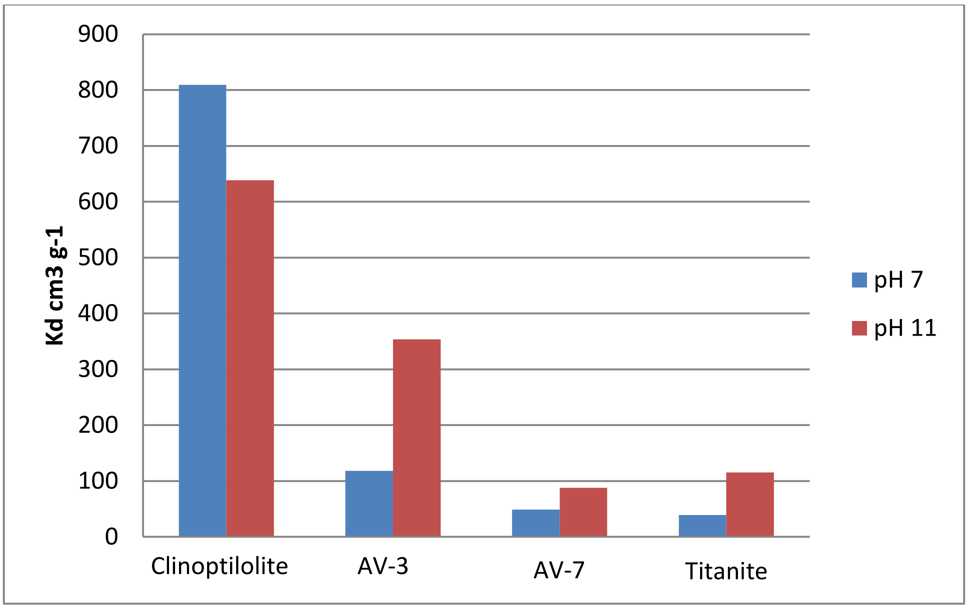

Figure 5. 2 - Material comparison for 100 ppm Sr ion exchange as measured by ion chromatography

Figure 5.2 indicates the relative performance of these materials, with clinoptilolite clearly showing the highest uptake, however, it is interesting to note that clinoptilolite shows reduced uptake with increased pH whereas the opposite is seen with AV-3, AV-7 and titanite. AV-3 appears to have the best performance of the new materials, possibly due to the higher surface area in comparison to the other materials due to the crystals being formed of clusters of thin sheets as shown previously through SEM images in Chapter 3. Whilst a higher surface area would not affect the bulk ion exchange properties if the system has reached equilibrium, it is possible that 24 hours is not sufficient time for equilibrium to be reached which would result in the ion exchange kinetics having a stronger influence over the observed strontium uptake.

Analysis of the chromatograms for the exchange of AV-7 in Figure 5.3 and also shown in Chapter 4 in Figure 4.8 and Table 4.5, show the strontium peak clearly decreases and a sharp increase in sodium and potassium indicates the ion exchange process, where strontium enters the pore and sodium and potassium are removed from the pores, according to the integrated intensity of the peaks the strontium concentration is reduced from 105 ppm to 24 ppm and an increase in sodium and potassium from trace amounts to 45 ppm and 11 ppm, respectively. This corresponds to 5.4×10^{-6} moles of strontium into the framework and 1.3×10^{-5} moles of sodium and potassium combined out of the framework which is concurrent with the ion exchange expected, approximately twice the amount of monovalent cations released compared to divalent Sr^{2+}removed from solution.

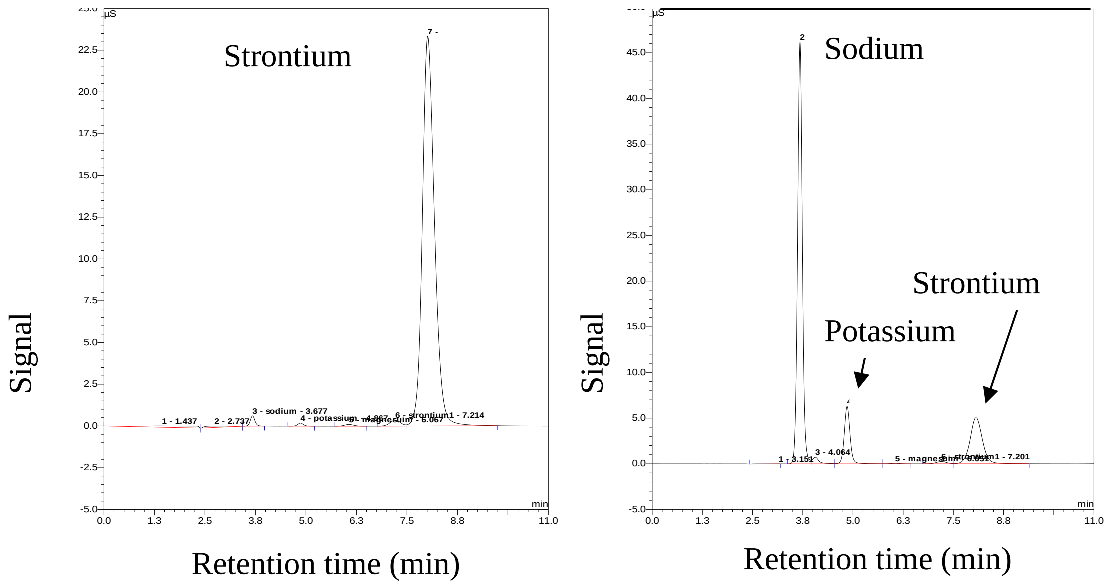

Figure 5. 3 - Example chromatogram for AV-7 before (left) and after (right) ion exchange

The chromatograms of AV-3, Figure 5.4 and Table 5.5 indicate the strontium concentration drops from 133 ppm to 89 ppm and sodium increases from trace amounts to 62 ppm corresponding to a strontium uptake of 3.01×10^{-6} moles and the release of 6.02×10^{-5} moles of sodium, approximately two and half times the expected amount of sodium released.

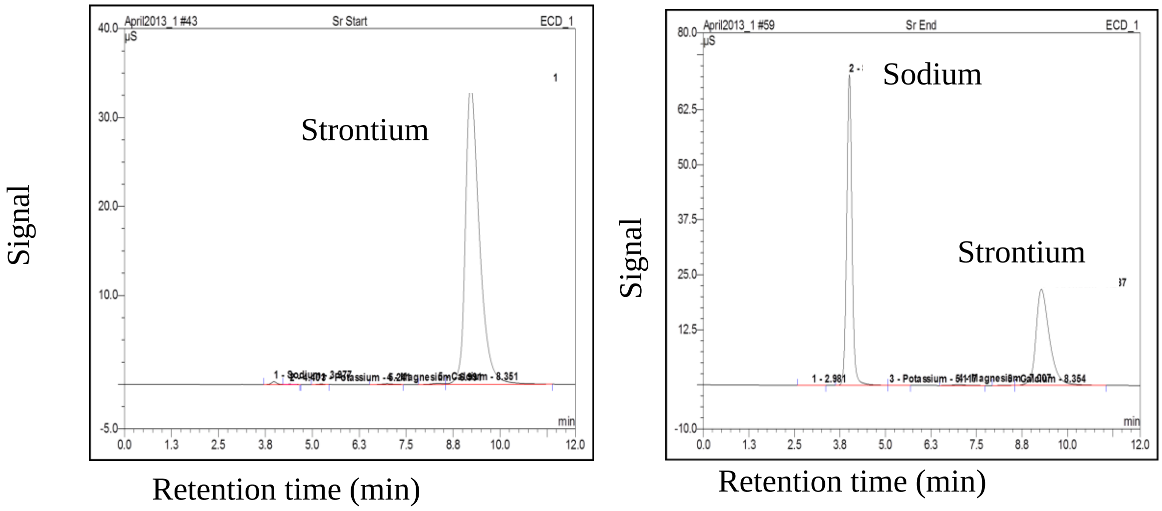

Figure 5.4 - Example chromatogram for AV-3 before (left) and after (right) ion exchange

Table 5. 5 - Integrated intensities and concentrationof AV-3 Ion exchange liquor as measured by ion chromatography

Peak Name	Before exchange		After Exchange	
	Integrated intensity (µS*min)	Concentration (ppm)	Integrated intensity (µS*min)	Concentration (ppm)
Sodium	0.04	0.31	12.00	62.82
Strontium	14.45	133.78	9.43	87.34

5.3-2a Initial exchanges

These exchanges were repeated, using the same 100 ppm $Sr(NO_3)_2$ concentrations but modified to contain 100 ppm of a competing cation. Examining the uptake shown in Figure 5.5, only calcium appears to have a significant detrimental effect on the uptake. The ionic radii of Ca^{2+} and Sr^{2+} are reasonably similar ranging from ~100-134 pm and 118-144 pm respectively, depending on coordination number. The similar size and charge and both being group II elements result in very similar chemical behaviour meaning it would not be surprising for calcium to strongly compete for the same cation site during ion exchange.

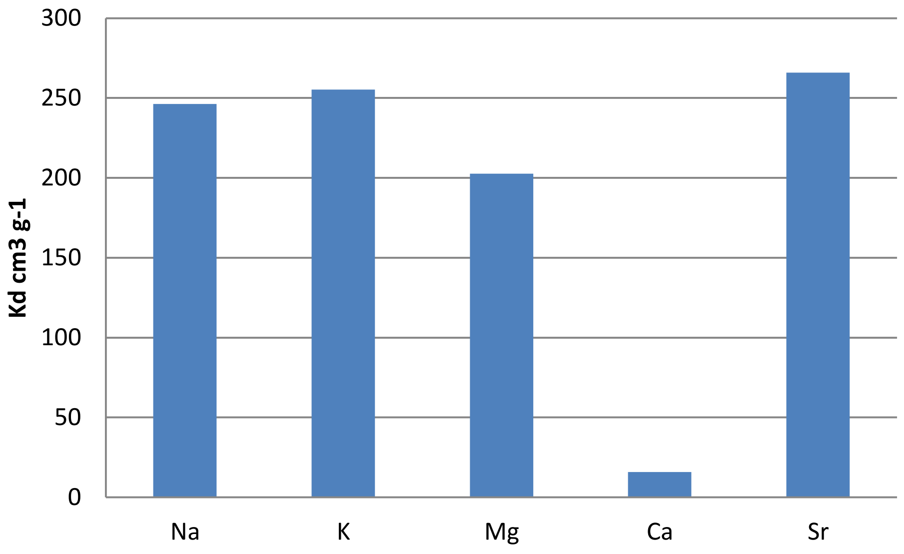

Figure 5. 5 - Batch distribution coefficients for competitive 100 ppm Sr ion exchange of AV-3 as measured by ion chromatography

5.3-3 ^{85}Sr ion exchanges

5.3-3a Initial exchanges

Initial radioisotope ion exchange experiments were performed on AV-7, AV-3 and titanite along with two well-known materials for comparison, clinoptilolite and niobium-doped crystalline silicotitanite. These exchanges were performed under slightly acidic conditions, ~ pH 6 due to the acidity of the water supply and strontium nitrate in solution.

As seen in fig 5.6 AV-7 exhibited a relatively high Sr uptake in comparison to both AV-3 and titanite, however, both clinoptilolite and Nb-CST show higher uptake.

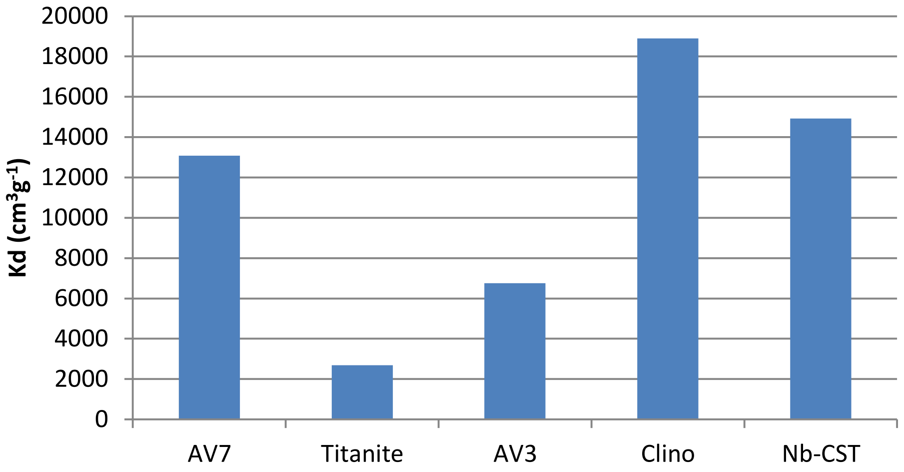

Figure 5. 6 - Batch distribution coefficients for initial 100 ppm ^{85}Sr ion exchange experiments

It is evident the strontium uptake of titanite is poor despite the porous structure and similarity to other materials. There are a number of potential reasons for the lack of ion exchange:

- Lack of water in the pores; unlike the other materials titanite is not a hydrated phase as there are no water molecules within the pores indicated by XRD. It is possible that water molecules within the channels of a material aid in the exchange mechanism in some way, such as solvating the outgoing cation to stabilize it. This trend is also noticeable in fresnoite, another porous anhydrous material which shows poor ion exchange properties;

- The pore size of titanite is too low; at the narrowest point, from the corner of one octahedron to the opposite tetrahedron, the pores are only 3.1 A wide, as shown in Figure 5.7, which may be too small to allow the necessary ion mobility throughout the pore to enable exchange;

- The calcium cations are bound too tightly electrostatically for an ion exchange to be favourable; in order to examine this possibility some modelling using static energy calculations was intended, however, due to difficulty finding correct potentials this work was not completed due to time constraints.

In these initial experiments AV-7 is observed to perform better than AV-3, both of which are exchanging at a reasonable level comparable to clinoptilolite obtained from NNL and Nb-doped CST. However, it should be noted these results were obtained before the fine tuning of the measurement method, in particular the count time of the samples for these measurements was 1 minute of live time, in which the detector was occasionally saturated leading to high proportion of dead time (up to 45%). Later measurements set thr gamma detector live time to 20 minutes per sample which gave much less dead time (max 2%) a significantly better counting statistics.

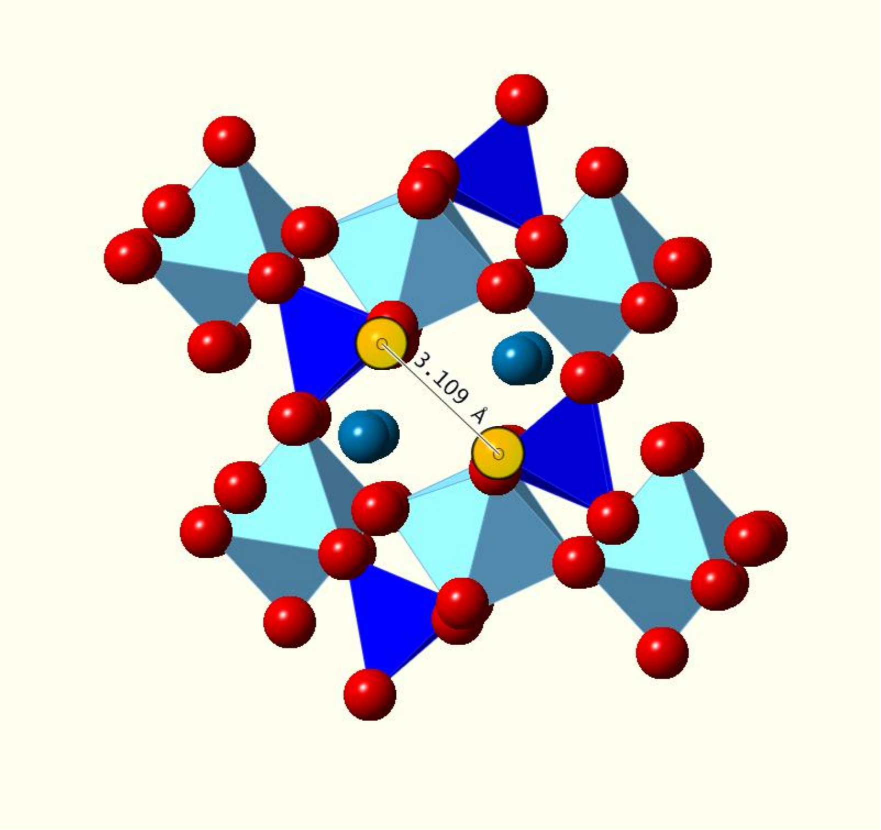

Figure 5. 7 - Structure of titanite illustrating pore diameter

5.3-3b Trace ^{85}Sr ion exchanges pH 7 & 4

These spiked exchanges were performed over two batches, using 100 ppm $Sr(NO_3)_2$ doped with ^{85}Sr, first examining strontium uptake in an acidic environment with no competition and strontium uptake in a pH neutral environment with competing cations, followed by pH neutral with no competition, and acidic with competition. Ideally these exchanges would have been completed in triplicate, however, due to only having small amounts of ^{85}Sr which had already decayed somewhat, it was not possible to complete such a large number of samples and still have sufficient counts necessary for reasonable counting statistics.

Many problems were encountered when measuring these samples. The geometry of a sample has a large impact on the counting, whilst all liquid and all solid samples should have similar geometries in relation to the detector the solid samples act more as a point source compared to the liquid samples where the ^{85}Sr is distributed throughout a larger volume. This effect results in significantly higher counts for the solid samples than for the liquid samples, in fact many of the solid samples read higher than the original stock solution making it impossible to use all the data acquired. In hindsight, shaking the solid samples in water to disperse the particles may have helped to alleviate this problem, but due to long counting times much of the solid would have settled again during the measurement resulting in an incorrect reading. Another solution to this problem and an improvement to the method in general would have been to calibrate the detector using stock ^{85}Sr solution of a known activity, both in a dispersed solution and in a more concentrated space as in the solid samples. Not only would this have enabled the use of the activities measured from solid samples to be used for more than just relative checks between samples but also to ensure that the assumed linear relationship between the integrated area of the signal peak and the activity of the sample is indeed true. Furthermore due to the high energy of the ^{85}Sr emission (514 keV) and the high sensitivity of the detector, even with lead shielding around the detector background, counts from other samples in the area provided a significant background which had to be mathematically subtracted.

The exchange liquors used for comparison were based upon work performed by Dyer *et al*[65] and the advice of Dr Zoe Maher of the NNL. In addition to AV-7 and AV-3, poorly crystalline zeolite with the gismondine (GIS) framework with an unknown Si/Al ratio prepared from coal-fly ash by R. Sommerville[66] and nenadkevichite, $(Na,Ca)(Nb,Ti)Si_2O_7{\cdot}2H_2O$, prepared by a MSc project student James Moore were investigated with pH neutral Sr exchange and acid competitive exchange. It should be noted that a significant variable in this test is the surface area of the particles. All materials were hand ground in an agate pestle and mortar and it was not possible to ensure all materials have the same particle size and thus surface area.

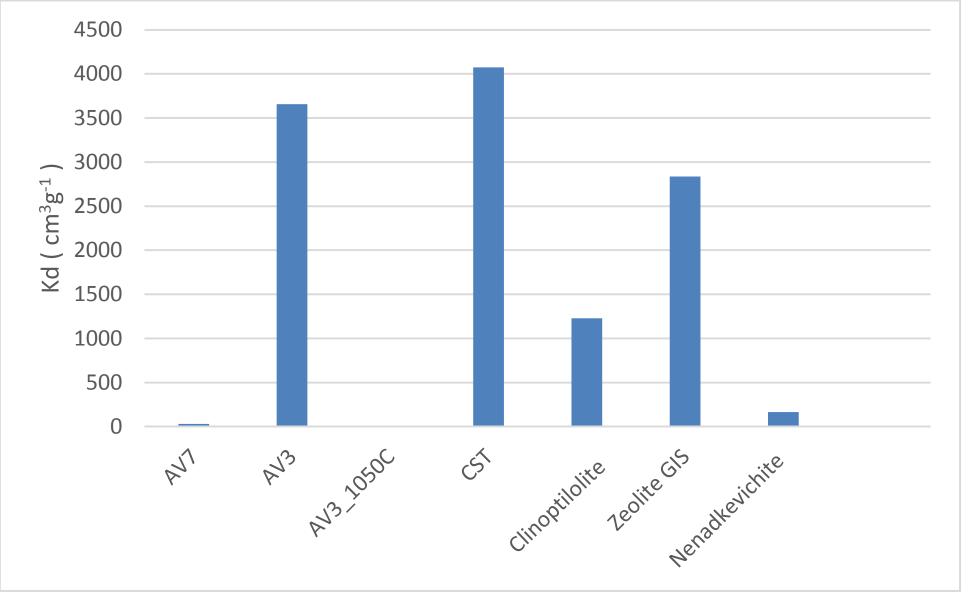

Figure 5. 8 - Batch distributions for multiple materials ion exchanged with 100 ppm Sr only at pH 7

Neutral pH strontium exchange, Figure 5.8, was used as a baseline to compare the other exchange conditions, AV-7 does exhibit uptake but significantly lower than other materials which are shown to perform comparably to industrially used CST and clinoptilolite. Unlike in the initial ^{85}Sr exchange, Figure 5.6, at a higher concentration of 0.5 mol dm^{-3} $Sr(NO_3)_2$, AV-3 is shown have higher uptake than AV-7. This could be due to a high degree of batch variation of the materials as the oven temperature can fluctuation greatly and small variations in the pressure of autoclaves due to varying degrees of leaking of the Teflon liners could have an effect on the synthesis.

.

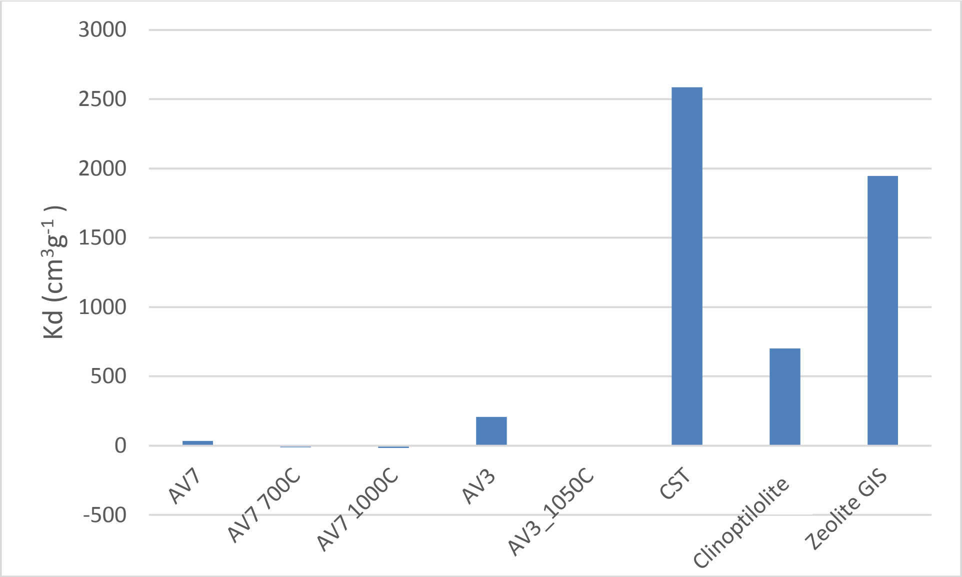

Figure 5. 9 - Batch distributions for multiple materials ion exchanged with Sr only at pH 4

Comparing Figures 5.8 and 5.9, With a decrease in the pH and no competitive cations AV-7 and AV-3 are shown (Figure 5.9) to ion exchange to a lesser degree than both Nb- CST and clinoptilolite interestingly the decrease in AV-3 is more significant than the decrease in clinoptilolite which might be expected to show a reduction in ion exchange due to dealumination from the low pH, however, the high Si/Al ratio would likely stabilize the framework and prevent dealumination under the moderately acidic conditions used here. Zeolite (GIS) retains a good uptake of strontium with the low pH actually improving the uptake of the latter.

Examining Figure 5.10 and comparing with Figure 5.8 indicates that whilst the strontium uptake of CST, AV3 and zeolite (GIS) and are all reduced upon the addition of competing cations, the uptake of AV-7 and clinoptilolite are mostly unaffected. The decreased uptake of AV-3 is less significant in the case of addition of competing cations than the decrease upon acidifying the solution.

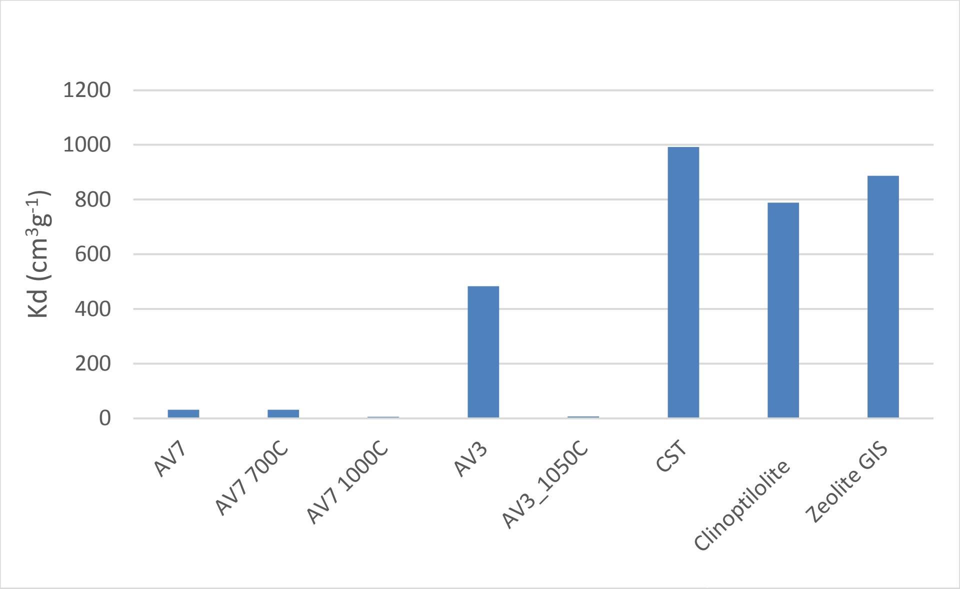

Figure 5. 10 - Batch distributions for multiple materials ion exchanged with Sr and competing cations at pH 7

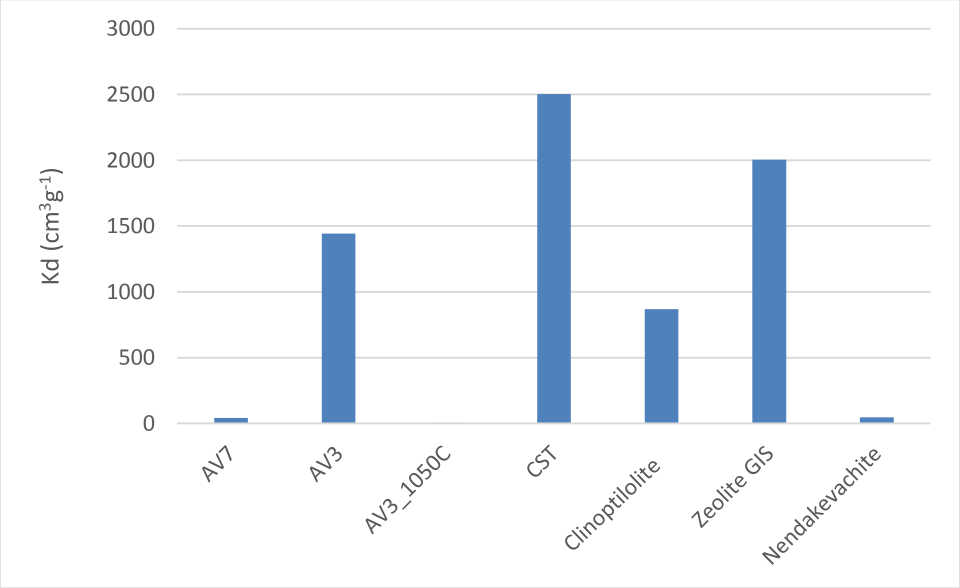

Figure 5. 11 - Batch distributions for multiple materials ion exchanged with Sr and competing cations at pH 4

With both an acidic solution and the introduction of competing cations, Figure 5.11, all materials bar AV-7 show reduced uptake. Whilst AV-3 does not exhibit the highest uptake in any situation it does show consistently good uptake. Whilst low, the uptake of AV-7 appears to be mostly unaffected regardless of conditions. Surprisingly the uptake of CST and in fact many other materials, is higher under acidic conditions than under neutral conditions when competitive cations are present; this runs contrary to most literature, and so perhaps a direct comparison should not be made but rather comparing within the series. This anomaly would indicate that this series of measurements should be repeated with a number of replicate samples.

In comparison to the initial exchanges shown at the start of section 5.3-3, the K_d values obtained for AV-7 are substantially different. This may be due to differences in the batch of AV-7 used or alternatively a dependence upon solid to solution ratio. Although theoretically the solid/solution ratio should be normalized by the definition of the K_d model, there may be some ion exchange sensitivity to concentration. A large solid/solution ratio would also result in solid particles coagulating together into larger particles which have a lower surface area and thus lessened adsorption on the surface. Further it may also be possible that the short period of 24 hours may not be sufficient to allow equilibrium to be reached, where exchange from the surface adsorption sites into the bulk exchange sites occurs, reducing the ion exchange uptake. These factors could potentially result in a reduced K_d measurement in systems with a high solid/solution ratio.

5.3-3c Trace ^{85}Sr ion exchanges pH 10-11

Having encountered problems with the previous method of ^{85}Sr ion exchanges, another set of exchanges were performed using a new scintillation counter to measure the activity of samples and ion exchange solutions suggested by the NNL as described in the experimental section of this chapter and shown here in Table 5.6.

Table 5. 6 - Ion exchange solutions compositions in ppm

Solution	A	B	C	D
pH	11.2	11	10	10
Cs (ppm)	9.06×10^{-4}	0.362	0.302	1.51
^{85}Sr + Sr (ppm)	1.51×10^{-5}	1.53×10^{-3}	5.67×10^{-3}	3.21×10^{-2}
Na (ppm)	70	130	60	210
K (ppm)	0.2	10	20	250
Ca (ppm)	0.2	3	1.2	60
Mg (ppm)	0.1	3	140	30

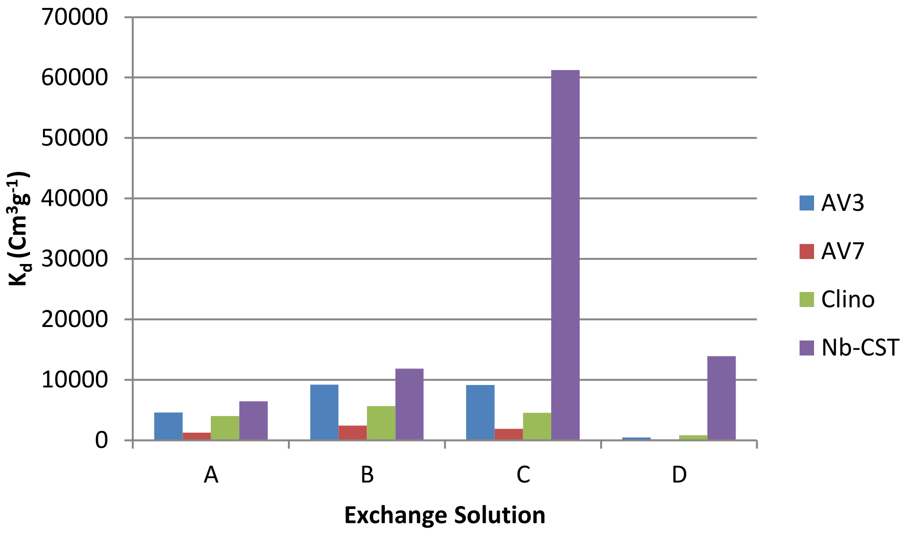

Figure 5. 12 - Comparison of batch distribution coefficients for strontium of multiple materials exchanged in a range of different solutions

As seen in Figure 5.12, the results for Nb-CST in solutions C where concentrations of magnesium are high & D with high concentrations of both sodium and potassium appear anomalous due to the K_d values being significantly higher than expected in comparison to solution A which should act as a baseline for comparison having no significant concentration of any competing cations. The very high uptake is observed is likely due to all the strontium being removed from solution which results in a very high number. AV-3 demonstrates reasonable uptake, performing well in comparison to Nb-doped CST and better than clinoptilolite in solutions A and B where strontium is in higher concentrations relative to other elements in the ion exchange solution.. The reasoning behind the poor selectivity of AV-3 is unclear as all of competing cations in the solutions have similar ionic radii between 100-150 pm which would mean a size-match effect is unlikely. The increased uptake of AV-3 over AV-7 and clinoptilolite may be due to the increased surface area of AV-3 as previously mentioned in this chapter, due to the morphology as seen in Chapter 3, where SEM images show the crystals are composed of clusters of parallel aligned plates which result in a higher surface area, however, this would only be in the case of equilibrium not being reached. Overall high pH appears to reduce the influence of calcium and magnesium competition, possibly due to the formation of insoluble $Ca(OH)_2$ and $Mg(OH)_2$ compounds in suspension which are not readily ion exchanged.

5.3-4 Hipping and leach testing

The stability of a wasteform is important considering spent ion exchange material will likely be stored for decades; but the long chemical stability needs to be extrapolated from short term leach tests performed according to standard methods. Two standard methods are commonly used, MCC (C 1220) based on a dense monolith with a known surface area and PCT (C 1285) where a powder is used and the surface area is either measured using a technique such as nitrogen adsorption and a BET isotherm or geometrically estimated using the particle size.

In order to produce a dense monolith for the MCC test, a process known as HIPing (Hot Isostatic Pressing) as previously described in Chapter 2 was used. 10 g each of AV-7 and

AV-3 were exchanged in 0.05 mol^{-1} dm^3 $Sr(NO_3)_2$ to 1.02 wt% and 1.91 wt% strontium respectively before HIPing at 1100 °C.

The HIPing process for AV-7 produced a uniform black material, Figure 5.13, however X-ray diffraction, Figure 5.14, revealed the sample to contain FeO and some tin metal as the only observable crystalline phases, although some peaks may be obscured due to the iron content causing significant fluorescence in addition to the amorphous content. The reducing conditions of the HIP can has not only caused the tin in the sample to be reduced but also caused the iron from the steel can to be drawn into the material and contaminate the material making this sample brittle and mechanically fragile.

Figure 5. 13 - Image of AV-7 post HIPing having cut the HIP can to reveal a dense black solid

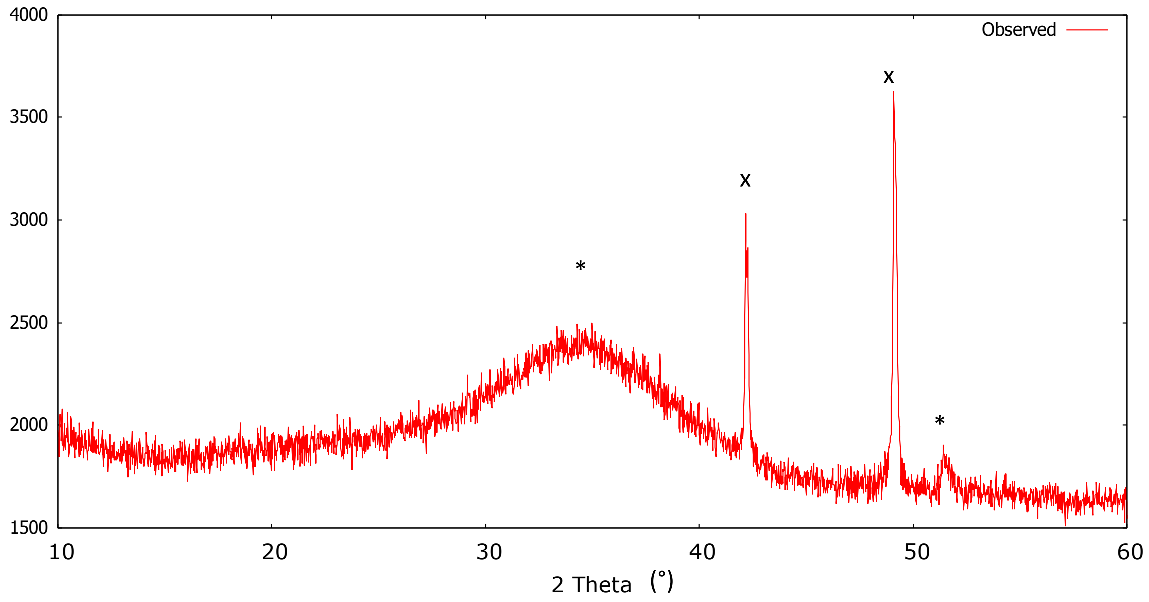

Figure 5. 14 - XRD pattern of HIPed AV-7 with peaks
x - FeO
*** - indicating Sn^0**

In the case of AV-3 the HIPing caused the formation of several different phases, which can be seen in the cross section of HIP can. The outer green edge indicates where the material reacted with the iron in the steel again and the core can be seen to be inhomogeneous as shown in Figure 5.15.

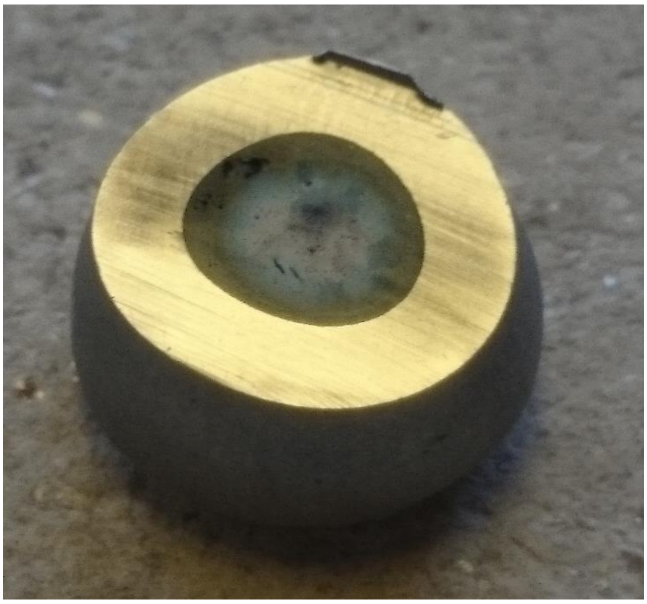

Figure 5. 15 Image of AV-3 post HIPing having cut the HIP can to reveal a dense green-white inhomogeneous solid

Powder X-ray diffraction, Figure 5.16, shows a number of different phases present, the main phase being parakeldyshite ($H_xNa_{2-x}ZrSi_2O_7$) as described in Chapter 3.

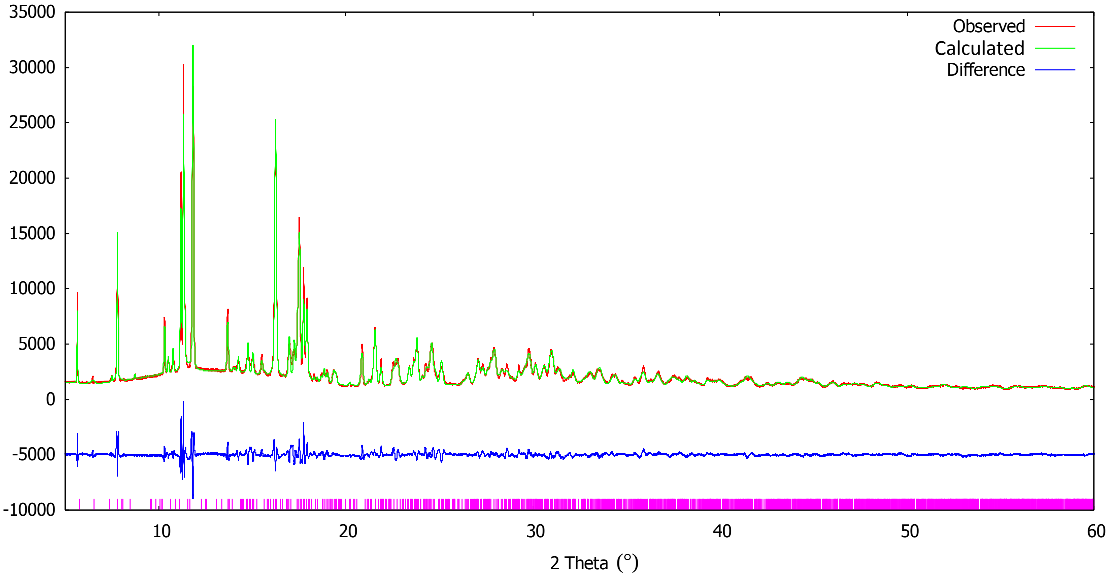

Figure 5. 16 - Refinement of HIPed AV-3 to identify parakeldyshite phase, see Chapter 3 for details

Table 5. 7 - Leach testing water concentrations as measured by ICP-OES & ICP-MS
*** indicating anomalous result**

Sample	K (mg/L)	Sr (mg/L)	Zr (mg/L)	Sn (mg/L)	Cl (mg/L)	Na (mg/L)	Si (mg/L)
	ICP-OES	ICP-MS	ICP-MS	ICP-MS	ICP-MS	ICP-OES	ICP-OES
Blank	0.05	8.1x10^{-4}	< 2x10^{-4}	1.16x10^{-3}	0.324	0.39	0.242
AV-7 A- 15 days	7.8	2.93x10^{-2}	-	1.73*	-	2.8	68.9
AV-7 B- 30 days (1)	7.7	1.06x10^{-1}	-	9x10^{-5}	-	1.63	102
AV-7 C- 30 days (2)	5.6	4.04x10^{-2}	-	2.26x10^{-2}	-	1.85	61.4
AV-7 D- 30 days (3)	5.5	5.5x10^{-3}	-	4.11x10^{-2}	-	1.86	105
AV-3 A- 15 days	-	1.24x10^{-2}	0.506	-	48.5	80.9	47.1
AV-3 B- 30 days (1)	-	2.36x10^{-2}	0.385	-	233	260	96
AV-3 C- 30 days(2)	-	1.62x10^{-2}	0.296	-	207	250	113
AV-3 D- 30 days(3)	-	2.49x10^{-2}	0.517	-	130	172	90.6

Table 5.7 gives the concentrations of various elements obtained by ICP-MS and ICP OES (performed by Robert Clough of Plymouth University) of the leachate solutions after following leach testing procedure MCC (C 1220). Regrettably sample AV-7 A appears to have been contaminated from another source of tin, possibly from a contaminate of the steel HIP can which may not have been completely removed from the monolith prior to testing. Also Sample AV-7B appears to have an unusually low concentration of tin, in this case lower than the supplied blank so AV-7 A and AV-7 B have been ignored for the case of tin leaching.

Table 5. 8 - Normalized elemental mass loss (g m^{-2})

Sample	K	Sr	Zr	Sn	Cl	Na	Si
AV-7 A- 15 days	4.71	0.15	-	1.27	-	5.1	39.05
AV-7 B- 30 days (1)	4.66	0.55	-	0	-	2.62	57.88
AV-7 C- 30 days (2)	3.37	0.21	-	0.02	-	3.09	34.79
AV-7 D- 30 days (3)	3.3	0.02	-	0.03	-	3.11	59.59
AV-3 A- 15 days	-	0.12	0.14	-	61.21	42.78	18.42
AV-3 B- 30 days (1)	-	0.24	0.1	-	295.65	137.94	37.64
AV-3 C- 30 days (2)	-	0.16	0.08	-	262.61	136.63	44.32
AV-3 D- 30 days (3)	-	0.26	0.14	-	164.77	91.18	35.52

Table 5.8 shows the normalized elemental mass loss $(NL)_i$ in g m^{-2} which is given by:

$$(NL)_i = \frac{(C_{ij} - B_i)V_j}{f_i SA} \qquad (5.1)$$

where,

C_{ij} is the concentration of element i observed in the leachate from sample j

B_i is the concentration of element i observed in the blank solutions averaged over replicate blank solutions

V_j is the volume leachate added to sample j

f_i is the mass fraction of element i in the unleached sample

SA is the surface area in m^2

In this case the concentration in the samples is obtained by XRF of the sample after grinding and fusing into a bead shown in Table 5.9. The surface area was calculated using image processing software ImageJ to measure the pixels within the area of the samples from pictures taken of the samples next to a ruler for scale using a digital camera.

Table 5. 9 – Composition of HIPed AV-7 and AV-3 as measured by XRF

Sample	K (wt%)	Sr (wt%)	Zr (wt%)	Sn (wt%)	Cl (wt%)	Na (wt%)	Si (wt%)	Fe (wt%)
HIPed AV-7	16.5(2)	1.90(3)	-	13.60(2)	-	4.7(3)	17.6(4)	44.21(2)
HIPed AV-3	-	0.94(3)	37.15(2)	-	2.9(5)	18.8(3)	23.4(4)	3.56(2)

The overall leaching observed for both AV-3 and AV-7 HIPed phases indicates a reasonably high leaching of silicon and sodium and potassium, which could indicate the formation of glassy sodium/potassium silicate phases which are more easily leached into solution. Chloride still present in the AV-3 appears to leach very readily, considering the higher sodium leaching of AV-3 there may also be chloride in a sodium silicate glassy phase as there is no NaCl evident in the PXRD patterns of this material. Overall the cation leach rate of both AV-3 and AV-7 appears to be significant, with the exception of strontium, however, this may simply be due to only small amount of strontium being present, and so a greater portion of the strontium present is in the bulk rather than the surface. Due to the high leaching rates and in the case of AV-7 poor mechanical properties, it would appear that the HIPing process under these conditions is not suitable for either AV-7 or AV-3.

5.4 Conclusions

This chapter contains work performed to study the ion exchange properties of AV-7, AV-3 and titanite in reference to other known ion exchange materials clinoptilolite and Nb-CST.

Ion exchange experiments were performed over a range of conditions, with variation of strontium concentration, competing cation concentration and pH in particular. The ion exchange was characterized by XRF on solid samples and ion chromatography on liquid samples at higher concentrations and using radioactive ^{85}Sr with scintillation counters to achieve the greater sensitivity needed for low concentration experiments. HIPing and subsequent leach testing of AV-7 and AV-3 was performed in attempts to produce dense ceramic phases suitable for wasteforms, however, neither AV-7 nor AV-3 appeared to form phases suitable for wasteforms due to high leach rates and poor mechanical properties.

Chapter 6: Summary

6.1 Conclusions

During this work the main focus has been to identify and characterize potential new materials for strontium ion exchange from nuclear waste streams or ponds. A number of brief surveys into possible routes for producing new materials were investigated with one new, as yet unidentified, material produced. Sn-kostyelvite (AV-7), petarasite (AV-3) and Ca-titanite were hydrothermally synthesised and the ion exchange properties explored with reference to a number of other known ion exchange materials. Strontium ion exchanged AV-7, AV-3 and Ca-titanite thermal decomposition products were investigated as were the phases formed during hot isostatic pressing of AV-7 and AV-3. Whilst AV-3 and AV-7 both demonstrate overall good ion exchange properties, with AV-3 exhibiting superior uptake to AV-7 over the low concentration range, neither currently perform substantially better than the currently established technology under the conditions examined.

6.1.1 Titanosilicates and zirconosilicates

Three porous materials, fresnoite, titanite and petarasite, have been synthesised hydrothermally. Whereas petarasite has been shown to undergo ion exchange, titanite and fresonite do not appear to do so. Upon ion exchange bond valence sums indicate the most favourable location to be on the Na1 site as at this site the valence sum, 2.03, is approximately equal to 2 for the Sr^{2+} cation. Upon heating, petarasite decomposes into a parakeldashite phase and another unidentified phase. Which phase the strontium is located in could not be established and further work would be necessary before the suitability of this phase as a waste form can be determined.

Titanite and fresnoite, however, do not appear to ion exchange and upon heating the structures appear to be stable up to 1000 °C. Whilst all of these materials have porous structures of 5 or 6 rings, only petarasite contains water molecules within the pores which may play an important role in the ion exchange process.

6.1.2 Stannosilicates

A brief investigation into the synthesis of a new stannosilicate phase for ion exchange was performed. Initial work suggests that due to the stability of SnO_2 aggressive conditions from high concentrations of hydroxide or fluoride ions are necessary for the crystallization of these types of materials.

A new sodium stannosilicate has been prepared using Sn^{II} oxalate, with a cubic structure which undergoes a phase transition to a monoclinic phase upon cooling to 100 K. Structure solution is still on-going but, having obtained high-quality synchrotron PXRD data along with solid state Si and Sn NMR, ICP/MS for elemental composition and TGA data, solution should be possible given time.

AV-7, a synthetic Sn form of kostylvite has also been prepared with good quality TOF NPD obtained to investigate the structure changes which occur upon strontium ion exchange with comparison to the reported structure in literature. The thermal decomposition product of Sr-loaded AV-7 has also been prepared and the structural changes investigated and compared to structural data published in literature.

6.1.3 Ion exchange

A variety of methods were used to characterize the ion exchange properties of AV-7, AV-3 and titanite with comparisons to Nb-CST and clinoptilolite. XRF spectrophotometry was used to characterize solid samples, however, much of the acquired data proved to be inconsistent and required normalizing to obtain sensible information. Frequently problems also arose with sample preparation causing fused beads to split and crack. XRF is also unsuitable for measuring aqueous samples due to X-rays penetrating through the sample which causes errors with the measurement as the backing plate of the sample holder is detected.

Liquid samples were measured with ion chromatography, which had a high throughput and reasonable sensitivity and measures multiple components in the solution so sodium or potassium exchanged from the solids into the solution can be quantified in addition to strontium. This technique was used to look at some ion exchange experiments in the 100-200 ppm region of concentrations, comparing AV-7, AV-3 and titanite with clinoptilolite and examining the competitive ion exchange of AV-3 under acidic conditions. However, the technique lacked the precision and sensitivity necessary for extremely low level exchanges which necessitated the use of ^{85}Sr and a scintillation counter.

^{85}Sr ion exchanges were performed in three batches, the first batch of experiments examined the ion exchange of a variety of ion exchange materials, AV-3, AV-7, Nb-CST and clinoptilolite under slightly acidic conditions ~pH 6. These initial exchanges indicated very low uptake for titanite which when examined with data obtained from ion chromatography, is likely due to surface adsorption rather than ion exchange. The second batch of ^{85}Sr ion exchanges were performed at much lower concentrations, < 1 ppb, where the whole concentration of strontium comes only from the added ^{85}Sr. These exchanges were performed over neutral (~pH 7) and acidic (~pH 4) conditions with and without competing cations. These experiments indicated very poor performance of AV-7 vs clinoptilolite and Nb-CST under these conditions, but AV-3 appeared to perform well. However the differences in measured activity are minimal and the solid samples which would have a much lower error could not be measured due to differences in the geometry of the instrument. Also at this concentration, it is possible that the process is dominated by surface adsorption rather than ion exchange so the material with the highest surface area would appear to have the greatest strontium uptake.

The final batch of ^{85}Sr ion exchanges improved upon the methods used previously, a new detector was purchased to enable a change in instrument setup allowing for more lead shielding to be used to reduce background radiation and improve the accuracy of the measurements. The exchange solutions used in this case were pH 10-11 in contrast to the acidic solutions used previously, also these exchange experiments had a number of competing cations at varying concentrations across the four solutions, the concentrations based upon the advice of contacts from the NNL. Under these conditions AV-7 again performed poorly in comparison to the other materials investigated, whereas AV-3 showed higher uptake than clinoptilolite but inferior to Nb-CST in most cases. Ion exchanges performed using solutions with higher concentrations of sodium, caesium or magnesium do not appear to affect significantly the strontium uptake of AV-3. Nb-CST shows some anomalous results in solutions C and D, which have high concentrations of magnesium for solution C and sodium and potassium for solution D, as a significantly greater uptake for these solutions is shown in comparison to solution A which does not contain high concentrations of any competing cations, although it does have a lower concentration of strontium. A general trend for the other materials is visible in that whilst magnesium and calcium do not appear to have a great effect at high pH, high concentrations of sodium and potassium are clearly detrimental to strontium uptake of these materials. Overall for the low concentration ion exchange experiments AV-7 shows poor strontium uptake and selectivity in comparison to other tested materials, whereas AV-3 appears to perform well in comparison to clinoptilolite but inferior to Nb-CST. Higher concentration ion exchange experiments indicate both AV-7 and AV-3 show poorer strontium uptake than clinoptilolite with AV-3 performing better than AV-7. Maximum strontium uptake on these materials may be dependent on differing factors depending on the concentrations of strontium and the concentrations of competing cations. If low concentration strontium uptake is dependent upon surface adsorption then the higher uptake of AV-3 at low concentrations could be explained by what appears to be a high surface area due to the morphology of the particles, although surface area measurements would be necessary to corroborate this.

Hot isostatic pressing was performed on strontium exchanged AV-7 and AV-3 to form dense phases suitable for leach testing, however, PXRD of the produced materials indicate that AV-7 appears to have amorphized and only one phase from the HIPed AV-3 has been identified. Due to problems with the HIP can, only 4 samples of each suitable for leach testing were able to be prepared. Following the procedure for MCC(C 1220) 3 repeats are necessary for 30 day leaching samples leaving one sample left for 14 days. After acquiring ICP-MS/OES elemental analysis normalized elemental mass loss values were calculated which revealed high leach rates for both AV-7 and AV-3, which render these materials along with these particular hipping conditions used unsuitable for producing good wasteform materials.

6.2 Further work

There are a number of areas which could be expanded upon in this work. In terms of synthesis work the synthesis of noonkanabahite or related phases batisite and scheherbakovite was not achieved. Whilst these are not common minerals, they do occur in nature and it should be possible to prepare them using hydrothermal methods, although long crystallization times may be necessary. The use of a cold-seal vessel, also known as a Tuttle bomb could potentially be of use in this area to reach higher temperatures and pressures, up to 1000°C and 1500 bar, not possible with a standard Parr acid digestion vessel. In general much of the synthesis work has been too broad in scope and could have benefited from more focus and a more specific series of experiments designed to more fully probe the synthesis conditions necessary to form stannosilicate materials. The structure of what appears to be a new stannosilicate material as discussed in Chapter 4 needs more work to solve the structure; with the data already acquired it should be possible to contruct a plausible model of the material given time.

With regards to ion exchange work, explaining why fresnoite and titanite appear to be poor ion exchange materials could be aided using computer modelling to calculate the relative stability of the different cation-exchanged forms and examining how unfavorable the creation of cation vacancy defects are as, in order for an ion exchange reaction to occur, cations must be able to be removed from the cation site. Having found adequate methods of measuring the ion exchange properties of these materials using XRF and ^{85}Sr studies, more detailed work could be performed to produce ion exchange isotherms detailing the change in behaviour more thoroughly. The ion exchange over a range of pH conditions should be investigated over a wider range with more data points to allow for a more definitive trend to be observed; similarly the effect of introducing competing cations should be investigated using a range of concentrations of each of these cations also over a range of pH conditions to reveal how the change in pH and thus the hydration sphere of all of the species in solution affect the ion exchange in terms of kinetics and overall uptake.

Also whilst some surface area and particle size measurements were attempted on AV-7 and AV-3 to help explain ion exchange trends at low concentraions, the obtained data was not of sufficient quality, as it produced nonsensical figures. This may be due to nitrogen not being the correct gas adsobant to use for these systems. Using porosimetry instruments to acquire surface areas and good isotherms of gas adsorption and comparing these to isotherms produced from ion exchange kinetics studies may aid in resolving the mechanisms of ion exchange or surface adsorption occuring at various concentrations.

The HIPing and leach testing experiments did not provide a great deal of useful information due to the degredation of the samples and limited number of samples which necessitated a smaller time scale. Exploring the different conditions possible when HIPing, and different sample preparation, would allow for better leach testing of the densified forms of strontium exchanged AV-7 and AV-3

References

1 DECC and NDA, *Radioactive Wastes in the UK : A Summary of the 2013 Inventory*, 2013.

2 D. Delacroix, J. P. Guerre, P. Leblanc and C. Hickman, *Radionuclide and Radiation Protection Data Handbook 2002*, Nuclear Technology Publishing, 2nd edn., 2002.

3 H. S. Thompson, *J. R. Agric. Soc.*, 1850, **11**, 313–379.

4 1954.

5 A. Clearfield, *Inorganic Ion exchange materials*, CRC Press, 1982.

6 A. Clearfield and J. A. Stynes, *J. Inorg. Nucl. Chem.*, 1964, **26**, 117–129.

7 L. Jukka, *Encyclopedia of Separation Science III, The Nuclear Industry: Ion Exchange*, Academic Press, 2000.

8 R. Harjula, A. Paajanen, J. Lehto, E. Tusa and P. Standring, in *Proc. Waste Management*, Tuscon, Arizona, 2003.

9 K. R. Rao, *Main*, 2001, **81**, 1534–1546.

10 E. Tusa, in *Proc. Waste Management*, Tuscon, Arizona, 2001.

11 D. R. Lewis, *Clays Clay Miner.*, 1952, **1**, 54–69.

12 C. Ma and R. A. Eggleton, *Clays Clay Miner.*, 1999, **47**, 174–180.

13 Y. Cho and S. Komarneni, *Appl. Clay Sci.*, 2009, **44**, 15–20.

14 S. W. Bailey, *Reviews in Mineralogy vol 13: Micas*, Bookcrafters Inc, Chelsea, Michigan, 1981.

15 R. Fricke, H. Kosslick, G. Lischke and M. Richter, *Chem. Rev.*, 2000, **100**, 2303–2405.

16 J. D. Sherman, *Proc. Natl. Acad. Sci.*, 1999, **96**, 3471–3478.

17 M. Howden and j Pilot, *Ion Exchange Technology*, Elis Horwood, London, 1984.

18 D. M. . Horsley and M. Howden, *Inst. Chem. Eng.*, 2005, **68b**, 141.

19 G. Alberti, U. Costantino and M. Pelliccioni, *J. Inorg. Nucl. Chem.*, 1973, **35**, 1327–1338.

20 V. Veselý, *Talanta*, 1972, **19**, 219–262.

21 G. Alberti, *Acc. Chem. Res.*, 1978, **11**, 163–170.

22 A. Clearfield, *Solvent Extr. Ion Exch.*, 2000, **18**, 655–678.

23 L. H. Baetslé, D. Van Deyck and D. Huys, *J. Inorg. Nucl. Chem.*, 1965, **27**, 683–695.

24 A. Dyer, J. Newton and M. Pillinger, *Microporous Mesoporous Mater.*, 2009, **126**, 201–212.

25 A. Dyer, R. Harjula, J. Newton and M. Pillinger, *Microporous Mesoporous Mater.*, 2010, **130**, 63–66.

26 A. Dyer, R. Harjula, J. Newton and M. Pillinger, *Microporous Mesoporous Mater.*, 2010, **135**, 21–29.

27 A. Dyer, J. Newton and M. Pillinger, *Microporous Mesoporous Mater.*, 2010, **130**, 56–62.

28 A. Dyer, J. Newton and M. Pillinger, *Microporous Mesoporous Mater.*, 2009, **126**, 192–200.

29 L. Jukka, L. Brodkin and R. Harjula, *Radioact. Waste Manag. Enviromental Remediat. - ASME 1997*, 1997, 245–248.

30 D. T. Hobbs, M. J. Barnes, R. L. Pulmano, K. M. Marshall, T. B. Edwards, M. G. Bronikowski and S. D. Fink, *Sep. Sci. Technol.*, 2005, **40**, 3093–3111.

31 T. B. Peters, M. J. Barnes, D. T. Hobbs, D. D. Walker, F. F. Fondeur, M. A. Norato, S. D. Fink and R. L. Pulmano, *Sep. Sci. Technol.*, 2006, **41**, 2409–2427.

32 A. Clearfield, A. I. Bortun, L. N. Bortun, D. M. Poojary and S. A. Khainakov, *J. Mol. Struct.*, 1998, **470**, 207–213.

33 S. Solbrå, N. Allison, S. Waite, S. V Mikhalovsky, A. I. Bortun, L. N. Bortun and A. Clearfield, *Environ. Sci. Technol.*, 2001, **35**, 626–629.

34 A. M. Puziy and J. R. García, *J. Radioanal. Nucl. Chem.*, 1999, **240**, 851–857.

35 N. Talaie, H. R. Aghabozorg and S. Alamdar Milani, *J. Radioanal. Nucl. Chem.*, 2012, **292**, 473–479.

36 D. M. Poojary, R. a. Cahill and A. Clearfield, *Chem. Mater.*, 1994, **6**, 2364–2368.

37 A. Bortun, L. Bortun and A. Clearfield, *Abstr. Pap. Am. Chem. Soc.*, 1997, **213**, 133–IEC.

38 US4853202 A, 1987.

39 J. Rocha, P. Brandão, M. W. Anderson, T. Ohsuna and O. Terasaki, *Chem. Commun.*, 1998, 667–668.

40 L. Liu, R. Singh, G. Li, P. Xiao, P. Webley and Y. Zhai, *J. Hazard. Mater.*, 2011, **195**, 340–5.

41 C. C. Pavel, K. Popa, N. Bilba, a. Cecal, D. Cozma and a. Pui, *J. Radioanal. Nucl. Chem.*, 2003, **258**, 243–248.

42 L. Lv, G. Tsoi and X. S. Zhao, *Ind. Eng. Chem. Res.*, 2004, **43**, 7900–7906.

43 A. Nalaparaju, Z. Q. Hu, X. S. Zhao and J. W. Jiang, *J. Memb. Sci.*, 2009, **335**, 89–95.

44 C. C. Pavel, M. Walter, P. Pöml, D. Bouëxière and K. Popa, *J. Mater. Chem.*, 2011, **21**, 3831.

45 N. J. Coleman, S. P. Lewis, A. P. Mendham and V. Trivedi, *J. Porous Mater.*, 2010, **17**, 747–753.

46 V. Sebastian, I. Diaz, C. Tellez, J. Coronas and J. Santamaria, *Adv. Funct. Mater.*, 2008, **18**, 1314–1320.

47 C. S. Fewox and A. Clearfield, *J. Phys. Chem. A*, 2008, **112**, 2589–2597.

48 C. S. Fewox, S. R. Kirumakki and A. Clearfield, *Chem. Mater.*, 2007, **19**, 384–392.

49 C. S. Fewox, A. Clear and A. J. Celestian, 2011, 3596–3604.

50 R. G. Anthony, R. G. Dosch, D. Gu and C. V Philip, *Ind. Eng. Chem. Res.*, 1994, **33**, 2702–2705.

51 L. Al-Attar, A. Dyer and R. Harjula, *J. Mater. Chem.*, 2003, **13**, 2963.

52 H. Xu, A. Navrotsky, M. Nyman and T. M. Nenoff, *J. Am. Ceram. Soc.*, 2005, **88**, 1819–1825.

53 S. Chitra, S. Viswanathan, S. V. S. Rao and P. K. Sinha, *J. Radioanal. Nucl. Chem.*, 2010, **287**, 955–960.

54 S. Chitra, R. Sudha, S. Kalavathi, a. G. S. Mani, S. V. S. Rao and P. K. Sinha, *J. Radioanal. Nucl. Chem.*, 2012.

55 D. V Marinin and G. N. Brown, *Waste Manag.*, 2000, **20**, 545–553.

56 Y. a. Uvarova, E. Sokolova, F. C. Hawthorne, R. P. Liferovich and R. H. Mitchell, *Can. Mineral.*, 2003, **41**, 1193–1201.

57 K. O. H. Zro, G. D. Ilyushin and L. N. Dem, *Inorg. Mater.*, 2002, **38**, 612–616.

58 S. Jale, A. Ojo and F. Fitch, *Chem. Commun.*, 1999, 411–412.

59 L. N. Demianets, *Prog. Cryst. Growth Charact. Mater.*, 1991, **21**, 299–355.

60 Z. Lin, J. Rocha, J. D. Pedrosa de Jesus and A. Ferreira, *J. Mater. Chem.*, 2000, **10**, 1353–1356.

61 R. P. Nikolova, K. Fujiwara, N. Nakayama and V. Kostov-Kytin, *Solid State Sci.*, 2009, **11**, 382–388.

62 R. P. Nikolova, B. L. Shivachev and S. Ferdov, *Microporous Mesoporous Mater.*, 2013, **165**, 121–126.

63 N. R. Petrova, N. Noriaki, B. Snejana, B. Petr and K.-K. Vladislav, *Solid State Sci.*, 2011, **13**, 1187–1190.

64 A. Ferreira, Z. Lin, M. R. Soares and J. Rocha, *J. Solid State Chem.*, 2010, **183**, 3067–3072.

65 Z. Lin, J. Rocha, P. Ferreira, A. Thursfield, J. R. Agger and M. W. Anderson, *J. Phys. Chem. B*, 1999, **103**, 957–963.

66 J. Rocha, P. Ferreira, Z. Lin, J. R. Agger and M. W. Anderson, *Chem. Commun.*, 1998, 1269–1270.

67 Z. Lin and J. Rocha, *Microporous Mesoporous Mater.*, 2006, **94**, 173–178.

68 Z. Lin and J. Rocha, *Stud. Surf. Sci. Catal.*, 2002, 319–325.

69 Z. Lin and J. Rocha, *Microporous Mesoporous Mater.*, 2004, **76**, 99–104.

70 Y. Xie, F. Chang, C. Li, J. Chen, J. Luo, L. Li and X. Hu, *CLEAN - Soil, Air, Water*, 2014, **42**, 521–527.

71 S. S. Mali, C. A. Betty, P. N. Bhosale, R. S. Devan, Y.-R. Ma, S. S. Kolekar and P. S. Patil, *CrystEngComm*, 2012, **14**, 1920.

72 R. Jenkins and R. L. Snyder, *Introduction to X-Ray Powder Diffractometry*, Wiley-Interscience, 1996.

73 W. H. Bragg and W. L. Bragg, *Proc. R. Soc. A Math. Phys. Eng. Sci.*, 1913, **88**, 428–438.

74 C. Hammond, *The Basics of Crystallography and Diffraction*, International Union of Crystallography Oxford Science Publications, Third Edit., 2009.

75 P. P. Ewald, *Acta Crystallogr. Sect. A Cryst. Physics, Diffraction, Theor. Gen. Crystallogr.*, 1969, **25**, 103–108.

76 A. Guinier, *X-ray diffraction in crystals, imperfect crystals and amorphous bodies*, W.H. Freeman, 1963.

77 C. Baerlocher, A. K. Cheetham, W. I. F. David, T. H. de Keijser, R. Delhez, R. J. Hill, F. Izumi, J. D. Jorgensen, J. I. Langford, D. Louer, E. J. Mittemeijer, E. Prince, J. W. Richardson Jr, H. M. Rietveld, T. M. Sabine, E. J. Sonneveld, R. L. Snyder, P. Suortti, H. Toraya, R. B. Von Dreele and R. A. Young, *The Rietveld Method*, 1995.

78 B. Beckhoff, B. Kanngieber, N. Langhoff and R. Wedell, *Practical X-Ray Fluroescence Analysis*, Springer.

79 H. Bennet and G. Oliver, *XRF Analysis of Ceramics Minerals and Allied Materials*, John Wiley & Sons, 1992.

80 Y. A. Uvarova, E. Sokolova, F. C. Hawthorne, R. P. Liferovich, R. H. Mitchell, I. V. Pekov and A. E. Zadov, *Mineral. Mag.*, 2010, **74**, 441–450.

81 D. M. Poojary, a I. Bortun, L. N. Bortun and A. Clearfield, *J. Solid State Chem.*, 1997, **132**, 213–223.

82 J. Rocha, P. Ferreira, Z. Lin, J. R. Agger, M. W. Anderson, R. A. J. and W. A. M., *Chem.Commun.*, 1998, 1269–1270.

83 D. G. Medvedev, A. Tripathi, A. Clearfield and J. Hanson, 2004, 3659–3666.

84 R. Hall and J. Readman, in *Acta Cryst.*, 2014, p. C1526.

85 V. I. Starichenko, *Russ. J. Ecol.*, 2011, **42**, 64–70.

86 G. . Gibbs and J. A. Speer, *Am. Mineral.*, 1976, **61**, 238–247.

87 M. Taylor and G. E. Brown, *Am. Mineral.*, 1976, **61**, 435–447.

88 P. B. Moore and J. Louisnathan, *Science (80-.).*, 1967, **156**, 1361–1362.

89 5110568, 1992.

90 Z. Lin, A. Ferreira and J. Rocha, *J. Solid State Chem.*, 2003, **175**, 258–263.

91 D. Wu, C. Han, S. Wang, N. Wu and I. A. Rusakova, *Mater. Lett.*, 2002, **53**, 155–159.

92 W. Clegg, *X-Ray Crystallography*, Oxford University Press, 2nd edn., 2015.

93 J. Evans and Bill David, .